THESIS

QUASI-GLOBAL AND REGIONAL WATER VAPOR AND RAINFALL RATE CLIMATOLOGIES FOR A 35 MONTH PERIOD

Submitted by

Kelly Michelle Howell

Department of Atmospheric Science

In partial fulfillment of the requirements

For the Degree of Master of Science

Colorado State University

Fort Collins, Colorado

Fall 2010

Master's Committee:

Department Head: Richard H. Johnson

Advisor: Thomas H. Vonder Haar

Co-Advisor: Stanley Q. Kidder

Christian D. Kummerow

Jorge A. Ramírez

ABSTRACT

QUASI-GLOBAL AND REGIONAL WATER VAPOR AND RAINFALL RATE CLIMATOLOGIES FOR A 35 MONTH PERIOD

Atmospheric water vapor and rainfall are crucial elements in the global water cycle. The spatial and temporal variations of total precipitable water (TPW) and rainfall rate (RR) between 60° N and 60° S are investigated. In addition, nine oceanic locations in different climate regions are further studied in order to clarify regional differences in a more detailed manner. The Blended Total Precipitable Water (bTPW) product from the Cooperative Institute for Research in the Atmosphere (CIRA) provides the water vapor observations and the Climate Prediction Center morphing method (CMORPH) product is used for the rainfall rate. These six-hourly datasets were analyzed at $0.25^{\circ}\times0.25^{\circ}$ resolution during the period between February 2006 and December 2008.

The variations present in these quasi-global TPW and RR climatologies are found to be similar to the variations presented in previous studies. For instance, oceanic TPW maximizes around 7° N at 45 mm, the most land-falling rain occurs around 2° S, and the most oceanic rainfall occurs around 7° N. However, both datasets over the 35 month period indicate an occurrence of the double Intertropical Convergence Zone during the boreal spring that is not evident in the previous TPW studies presented. Over the study period, the

quasi-global CMORPH mean daily RR is 2.63 mm day^{-1} and the quasi-global bTPW mean oceanic TPW is 24.94 mm.

Regionally, the rainfall rate distributions were found to approximate exponential decay, with typically drier regions corresponding with faster decay rates. This pattern is also evident on a global scale. While one might expect an increased TPW to correspond with an increased RR, it was found that rainfall is possible at nearly any TPW value. On a global scale, higher TPW values are associated with higher probabilities of rainfall, although global patterns of moisture convergence and vertical motion are key factors in the production of this rainfall. The RR algorithms used to form the CMORPH product are less sensitive to stratiform light rain, which means that rainfall is likely underestimated in areas receiving mostly this type of rain, such as the subtropical eastern Pacific Ocean. The results demonstrate that the bTPW and CMORPH products produce observations consistent with past climatologies and that TPW on its own is not an accurate indicator of rainfall; other dynamical and thermodynamical effects must be considered.

ACKNOWLEDGEMENTS

First, I'd like to thank my family for their confidence in my ability to succeed and for their unrelenting support. I am also grateful to my friends for their readiness to listen and keep in touch from across the country. Thanks to Jessica Ram, Eric Guillot, Heather Cronk, and Darren Van Cleave, my officemates in room 301; your fun personalities got me through hours of studying, coding, homework, and writing. I am also grateful my advisor and co-advisor, Dr. Tom Vonder Haar and Dr. Stan Kidder, for their discussions and enthusiastic advice on the direction of this project. Finally, I thank my committee members, Dr. Chris Kummerow and Dr. Jorge Ramírez, for their time in reviewing and helping to improve this thesis. This study was supported by the Department of Defense Center for Geosciences/Atmospheric Research at Colorado State University under Cooperative Agreement W911NF-06-2-0015 with the Army Research Laboratory.

TABLE OF CONTENTS

1. INTRODUCTION

Atmospheric moisture and rainfall play an important role in the global water cycle. Precipitation is “an essential component of the hydrological cycle” and is likely the “longest observed and most widely recorded hydrological phenomenon” (Legates and Willmott 1990). Total precipitable water (TPW) is a necessary condition for rainfall. One might expect that increased atmospheric moisture is directly related to increased precipitation. For instance, moisture plumes, also known as atmospheric rivers or areas of relatively high TPW, are “often associated with heavy rainfall events” (Junker et al. 2008). However, the relationship between the two parameters is not so simple. Several other factors contribute to the occurrence of rain, including convection, horizontal flow dynamics, and the presence of cloud condensation nuclei, but none of these factors is the sole catalyst for the occurrence of rainfall.

One reason for investigating both TPW and rainfall rate (RR) is that, as the climate changes, there is a need for improved understanding of ‘the changing character of precipitation.’ Schlosser and Houser (2007) state that “such global metrics will be valuable to the general public, much like global averaged temperature, in conveying the ‘status’ of global changes in water transport.” Trenberth (1998) describes that an increase in greenhouse gas concentrations may result in changes in distributions of precipitation. Increased greenhouse gas concentrations lead to an increase in downwelling infrared radiation, which increases the surface temperature. This temperature increase, in turn, leads to an increase in atmospheric water vapor, as described by the Clausius-Clapeyron equation. A bigger absolute increase in water vapor would occur in the tropics by this argument since the Clausius-Clapeyron equation is nonlinear (Trenberth 2003). This means that the intensity of global changes in water vapor may be latitudinally-stratified. However, an increase in atmospheric temperature and water vapor does not necessarily imply an increase in global mean evaporation. Evaporation depends not only on the air temperature, but also on the wind speed and the relative humidity (Hartmann 1994). If evaporation does in fact increase, then globally, "there must be an increase in precipitation to balance the enhanced evaporation but the processes by which precipitation is altered locally are not well understood" (Trenberth 1998). Understanding the relationship between TPW and RR both globally and regionally therefore becomes increasingly important as the character of Earth's atmosphere changes. In addition to its effects as the climate changes, the relationship between TPW and RR is an "integral part of theories" explaining the Madden-Julian Oscillation, convectively-coupled waves, and hurricanes (Muller et al. 2009).

A related reason to study these parameters together is to produce a relationship that may be useful for improving forecasting methods, particularly in areas lacking adequate forecasting capability, such as the Middle East. Improved forecasts in these sorts of areas would contribute to operational decision-making, since heavy rainfall events may impede operations in terms of trafficability. Even meteorologically data-rich areas would benefit from improved forecasting of flood-inducing heavy rainfall, both in terms of early warnings for citizens and in mitigation procedures for the predicted floodwaters. "Accurate forecasts of extreme rainfall events and their associated runoff would allow for the advanced release of water from dams, thereby reducing the damage from floods" (Junker et al. 2008). Several recent studies discussed in Sec. 2.5 and new operational forecasting aids (NESDIS

Operational Blended TPW Products Website) have used TPW thresholds and anomalies (CIRA Experimental Merged Total Precipitable Water Products Website) to assist in characterizing rainfall events.

This thesis expands upon previous studies by analyzing high spatial and temporal resolution quasi-global datasets of TPW and RR products from nine satellite-based instruments. These datasets allow for independent reproducibility of quasi-global variations in TPW and RR; this study is the first known to use these particular datasets to produce such climatologies. Chapter 2 presents previous TPW and RR climatologies as well as regional studies focusing on the influence of various factors on local rainfall. Chapter 3 introduces the instruments and products used to measure TPW and RR. Chapter 4 discusses the choice of domain and the determination of statistical values used to analyze the data. Chapter 5 examines the 35 month quasi-global climatologies of these parameters as well as investigates more localized relationships between TPW and RR. Chapter 6 discusses possible explanations for these results and presents ways to expand upon this study's findings.

2. PREVIOUS STUDIES ON TOTAL PRECIPITABLE WATER AND RAINFALL RATE

2.1 A Brief Overview of Passive Microwave Remote Sensing

The first usable satellite radiometric data became available in 1959, measuring the Earth's reflected solar and emitted infrared radiation (Kidder and Vonder Haar 1995). The first microwave data became available in 1968 from Soviet satellites (Kidder and Vonder Haar 1995). Visible and infrared rainfall and water vapor estimation techniques began to be studied in the early 1970s. Passive microwave (PMW) rainfall and water vapor estimation techniques have been in effect since the Electrically Scanning Microwave Radiometer (ESMR-5) was launched in December 1972 and the Scanning Microwave Spectrometer (SCAMS) was launched in 1975 (Kidder and Vonder Haar 1995).

Wilheit et al. (1977) saw the necessity of sensing meteorological parameters over the ocean: "…the rainfall occurring over the oceans, which cover three-fourths of the earth's surface, is very poorly known." The lack of numerous microwave channels necessitated Wilheit et al. (1977) to depend on theoretical arguments in their determination of over-ocean rainfall, making assumptions about parameters such as drop size distribution, humidity, and freezing level. Their results show that brightness temperatures at 19.35 GHz can be related to rain rate "within a factor of 2." This study showed that "it is possible to measure the oceanic component of the atmospheric water budget" using satellite sensing techniques.

Spencer (1986) expanded upon the Wilheit et al. (1977) study through the use of data from 19 and 37 GHz channels, which "primarily reflects the availability of existing satellite data." These wavelengths relate the rain rate to the scattering portion of the attenuation. At 37 GHz, "only those hydrometeors of precipitation size will cause significant scattering, which acts to reduce the Tb below that which is due to emission alone. Therefore, even though rain is an efficient absorber (emitter) of 37 GHz radiation, it will simultaneously act to depress the Tb through scattering....Precipitation-size ice, as previously discussed, will enhance the scattering effect. It is this scattering signature alone that we will relate to rain rate" (Spencer 1986). Spencer's RR retrievals in the 1980s depended on similar principles as the retrieval methods used in this study, although the algorithms used for this study depend on the stronger ice scattering signals from higher frequency channels (i.e., 85, 89, 150, and 183 GHz). The sensors used by Spencer needed signal and calibration refinement, since the "scattering signal at 37 GHz is not as strong as the emission signal of light precipitation at 19 GHz."

Spencer (1986) also saw ahead to the possible direction rainfall sensing might take, noting the upcoming arrival of SSM/I data, which includes a channel at 85.5 GHz. "Ultimately, a combination of a scattering (high frequency) method with an emission (low frequency) method will probably be the most accurate means of obtaining global rainfall statistics" (Spencer 1986). This study also made it evident that over-ocean rainfall estimation is less prone to confounding factors than is over-land rainfall estimation, due to highly variable land surface emissivities. Spencer's (1986) algorithm performs better over the ocean (0.90 correlation) than it does over land (0.58 correlation) when compared with results from a 1983 study by Spencer et al.

Satellite methods have become much more sophisticated since the first PMW studies. In contrast to Spencer's (1986) two channel over-ocean algorithm, the Tropical Rainfall Measuring Mission (TRMM) Goddard Profiling Algorithm (GPROF) uses several channels to determine the nature and quantity of rainfall with much greater accuracy over both land and ocean, in both ice and iceless cases. Even though the GPROF is much more complex than earlier rainfall estimation algorithms, it is still computationally less expensive than previous profiling algorithms (Kummerow et al. 1996). Since data analysis techniques as well as the sensors themselves have improved since earlier studies, datasets such as those used in the current study are relatively accurate and finely resolved, both spatially and temporally.

The top-of-atmosphere microwave radiances are due to radiation from both the surface and the atmosphere. The surface contributions depend mainly on surface type and temperature. Atmospheric contributions depend on the emission and scattering properties of the constituents, such as precipitation, water vapor, and other trace gases (Kummerow et al. 1996). The microwave radiation emitted from raindrops is not heavily attenuated by clouds because cloud droplets are very small relative to the millimeter-scale microwave radiation. Thus in this region of the spectrum, absorption and scattering due to cloud drops is "negligibly small" (Kidder and Vonder Haar 1995). Microwave radiometers do, however, detect rainfall because rain droplets are of comparable size to microwave wavelengths (Kidder and Vonder Haar 1995).

"Microwave methods are also complementary to visible and IR methods because the microwave radiation is sensitive to larger ice crystals and to thicker cirrus layers whereas visible/IR radiation is more sensitive to smaller particles and cirrus clouds" (Weng et al. 2003). Microwave frequencies of 31, 89, and 150 GHz most strongly sense cloud liquid and ice water, detecting emission from cloud liquid and scattering from ice particles (Weng et al. 2003). Using observations at both 89 and 150 GHz to determine the differential ice scattering signature allows for a "better retrieval of precipitating ice microphysical properties" (Bennartz and Bauer 2003). In general, high microwave frequencies are more sensitive to ice scattering while lower microwave frequencies are more sensitive to rain or water vapor emission (Kidder and Vonder Haar 1995). The frequencies used in this study range from 21.3 to 183.3 GHz, which correspond to wavelengths between 14.08 and 1.64 mm, respectively. The particular methods used to relate different channels' signals to a RR or TPW estimate will be explained in more detail in Chapter 3.

2.2 Total Precipitable Water Climatology

Total precipitable water (TPW) is defined as "the total atmospheric water vapor contained in a vertical column" from the earth's surface to the top of the atmosphere (AMS Glossary Website). It is also commonly referred to as integrated precipitable water, precipitable water vapor, and total column water vapor. Atmospheric moisture has a residence time of about 8 days, with residence times averaging 12 days in tropical convergence zones and much shorter in subtropical high regions (Trenberth 1998). TPW tends to exceed 50 mm in the ITCZ, while it is less than 10 mm "in areas having extensive subsidence," such as the subtropical highs (Grody et al. 2001). Since areas such as the subtropical highs have high evaporation rates but little precipitation, horizontal advection of moisture and moisture convergence is a critical factor for precipitation. "On average less than 20% of the precipitation that falls comes from evaporation within a distance of about 1000 km" (Trenberth 1998). Local evaporation will not affect the intensity of the precipitation as much as the moisture that is transported into a region, since "moderate or heavy precipitation feeds mostly on the moisture already in the atmosphere" (Trenberth 1998).

Trenberth (1998) used National Aeronautics and Space Administration (NASA) Water Vapor Product (NVAP) estimates between 1988 and 1992 to produce the annual mean TPW plot shown in Fig. 2.1. Sudradjat et al. (2005) also studied the NVAP TPW dataset and found the global mean TPW to be 24.52 mm. They also studied the National Center for Environmental Prediction (NCEP)-National Center for Atmospheric Research (NCAR) reanalysis-1 and reanalysis-2 products, which resulted in global mean TPW values of 23.87 and 24.65 mm, respectively (Sudradjat et al. 2005). Figure 2.1 shows that

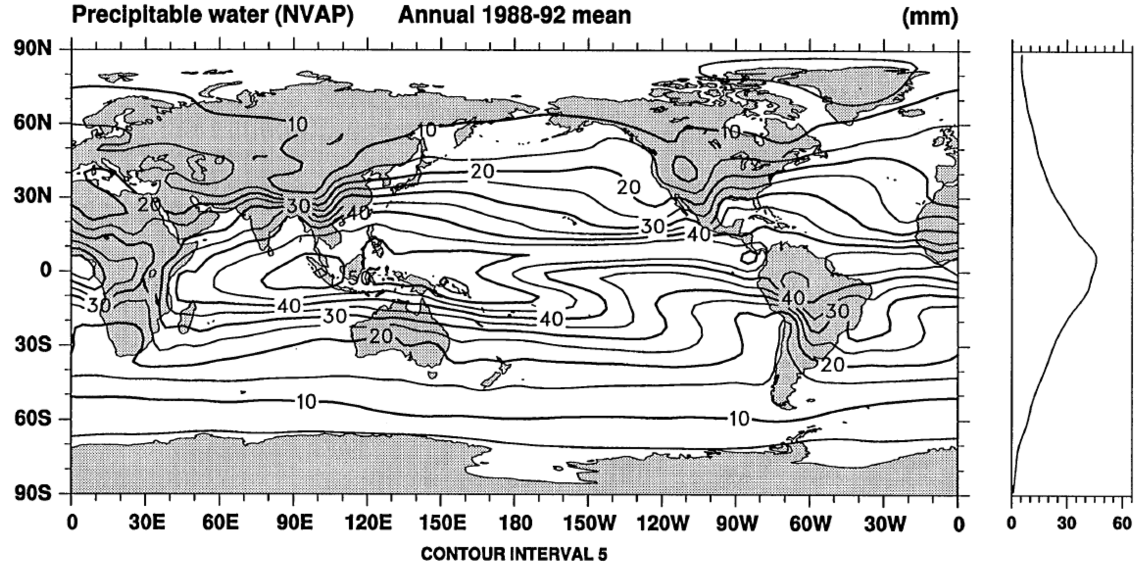

FIG. 2.1. Annual mean precipitable water for 1988-1992 from NVAP data. At right is the zonal mean profile of TPW in mm. Source: Trenberth (1998).

atmospheric moisture has its highest values around the equator, with values exceeding 50 mm located around the west Pacific warm pool. The plot at the right of Fig. 2.1 demonstrates that the zonally and annually averaged maximum TPW occurs just north of the equator. The maximum TPW values concentrated just north of the equator are called the Intertropical Convergence Zone (ITCZ) and the southeast-reaching arm of the west Pacific warm pool high TPW values is called the South Pacific Convergence Zone (SPCZ). The lowest values tend to be found off the subtropical west coasts of continents and in the high latitudes.

In contrast to the zonally and annually averaged TPW presented by Trenberth (1998) at the right of Fig. 2.1, Ferraro et al.'s (2005) July 2004 mean TPW, shown in Fig. 2.2, maximizes around 8° S. This discrepancy is indicative of how much the seasonal variations in TPW distribution oscillate around the annual mean distribution.

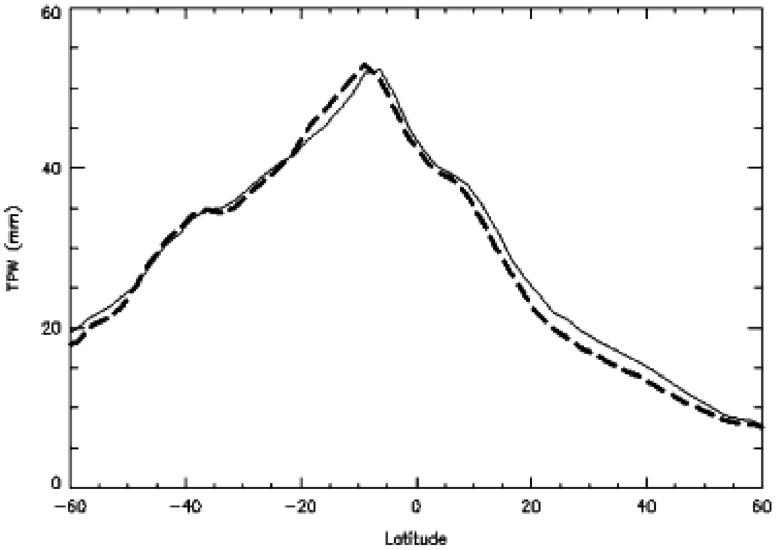

FIG. 2.2. Zonal monthly mean total precipitable water in mm for July 2004 from NOAA-16 AMSU (dashed) and Aqua AMSR-E (solid). Source: Ferraro et al. (2005).

Amenu and Kumar (2005) find that the interseasonal variability in TPW is greater than the interannual variability. Ferraro et al. (1996) used SSM/I measurements between 1987 and 1994 to produce the seasonal mean TPW plots shown in Fig. 2.3. These plots show similar patterns to those in Fig. 2.1, with the highest TPW values along the ITCZ and the west Pacific warm pool and the lowest values at the high latitudes and in subtropical high regions. These dry regions off the subtropical west coasts of North America, South America, and northern and southern Africa can be described as 'oceanic deserts' due to their relatively

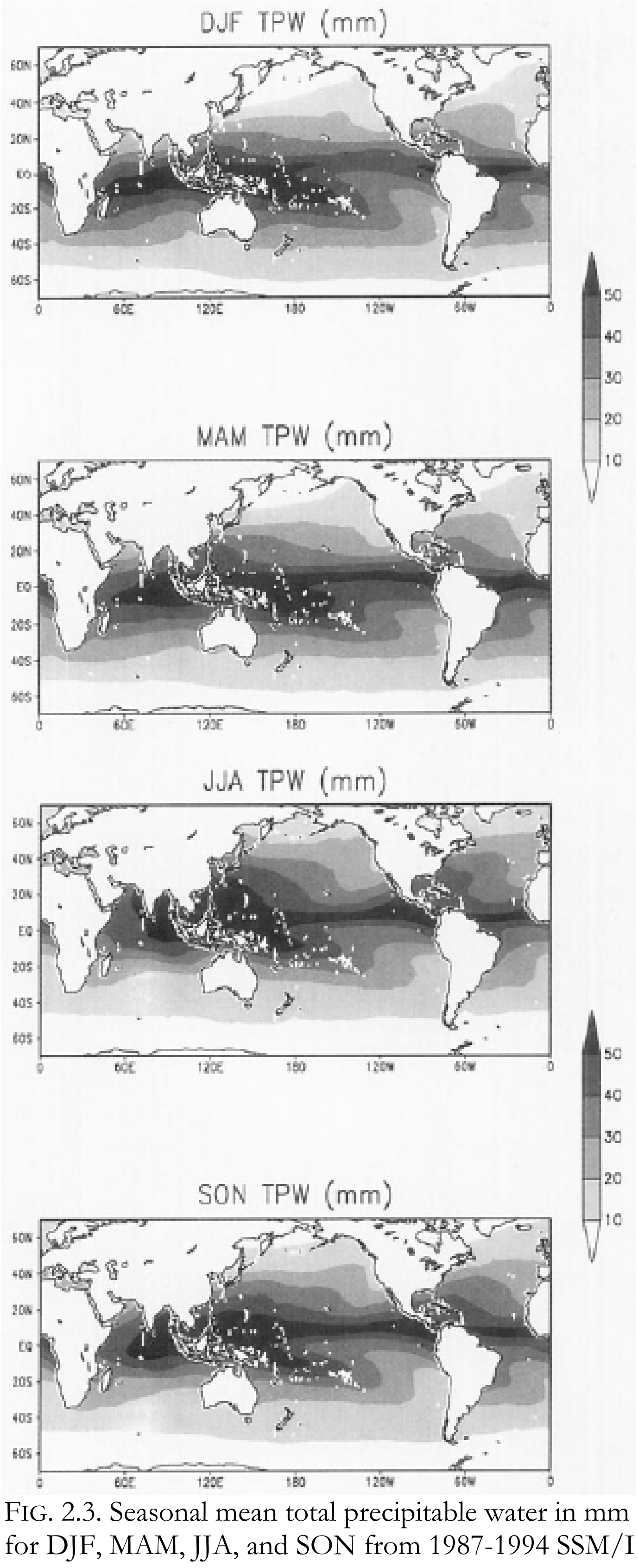

FIG. 2.3. Seasonal mean total precipitable water in mm for DJF, MAM, JJA, and SON from 1987-1994 SSM/I measurements. Source: Ferraro et al. (1996).

low TPW values and rainfall frequencies. They occur because of atmospheric subsidence and lower oceanic sea surface temperatures (Ferraro et al. 1996). Although a southern band of the ITCZ is not apparent during MAM, the eastern tropical Pacific does experience a wider band of high TPW values during MAM as compared with the other seasons. The Northern Hemisphere (NH) summer, occurring during June, July, and August (JJA), is characterized by the south Asian and southwestern United States monsoons, as evidenced in the increased TPW around these regions during JJA. Another feature of Fig. 2.3 that is lost in the annual average is the poleward migration of higher TPW values into the summer hemisphere. The SPCZ TPW values also vary with season, reaching the farthest southeastward in December, January, and February (DJF), or the SH summer. Amenu and Kumar (2005) find TPW anomalies to be "closely related to global surface temperature anomalies, with the temperature driving the precipitable water," as described in Chapter 1.

On a daily timescale, Dai et al. (2002) find that the peak TPW in North America typically occurs around solar noon during the winter and from mid-afternoon to midnight during the summer. The diurnal cycle has a variance between 1.0 and 1.8 mm and varies the least during the NH spring. Diurnal variations are induced by surface evapotranspiration, atmospheric large-scale vertical motion, and low-level moisture convergence and precipitation (Dai et al. 2002). Changes in the large-scale vertical motion should produce wet anomalies at night and dry anomalies during the day. "The results of this study suggest that atmospheric water vapor has significant diurnal variations, although the diurnal amplitude is generally small (≤5% of the mean)" (Dai et al. 2002). In this way, the variations in TPW over timescales longer than a day are larger than the sub-daily variations. These results also support Trenberth's (1998) assertion that local evaporation (i.e., over 1000 km scales) does not significantly contribute to that region's precipitation.

2.3 Rainfall Rate Climatology

Rainfall rate (RR) is defined as the amount of rain that falls during a given amount of time. According to a study by Legates and Willmott (1990) based on rain gauge measurements, “annual average global precipitation is approximately 1123 mm”, which is a value consistent with similar gauge-based studies. Legates and Willmott (1990) used gauge-based precipitation estimates because radar and satellite estimates were relatively new technologies and long-term means from remote sensing sources were unavailable at that time. Newer studies show the global mean RR to be about 2.8 mm day^{-1} (Trenberth et al. 2003; Xie and Arkin 1997).

2.3.1 Spatial Distribution of Rainfall

The global distribution of rainfall is fairly analogous to the global distribution of TPW. Figure 2.4 shows the annual mean daily RR from the Legates and Willmott (1990) study, which indicates the heaviest rainfall along the ITCZ and a general decrease in precipitation toward the poles. This plot also indicates a dearth of rainfall in the oceanic desert and continental desert regions. Along the ITCZ, “intense surface heating and the confluence of the tropical easterlies result in annual precipitation rates that often exceed 8 mm day^{-1}” (Legates and Willmott 1990). They also find that precipitation is typically heavier over the oceans than it is over land. Table 2.1 describes global mean RR values over ocean areas, land areas, and both (global) for three different studies. In addition, precipitation amounts appear to be more variable in the NH than in the SH. “Moderating influences that the oceans exert on precipitation are evident particularly in the Southern Hemisphere. Precipitation variability is especially damped over the extensive southern ocean” (Legates and Willmott 1990).

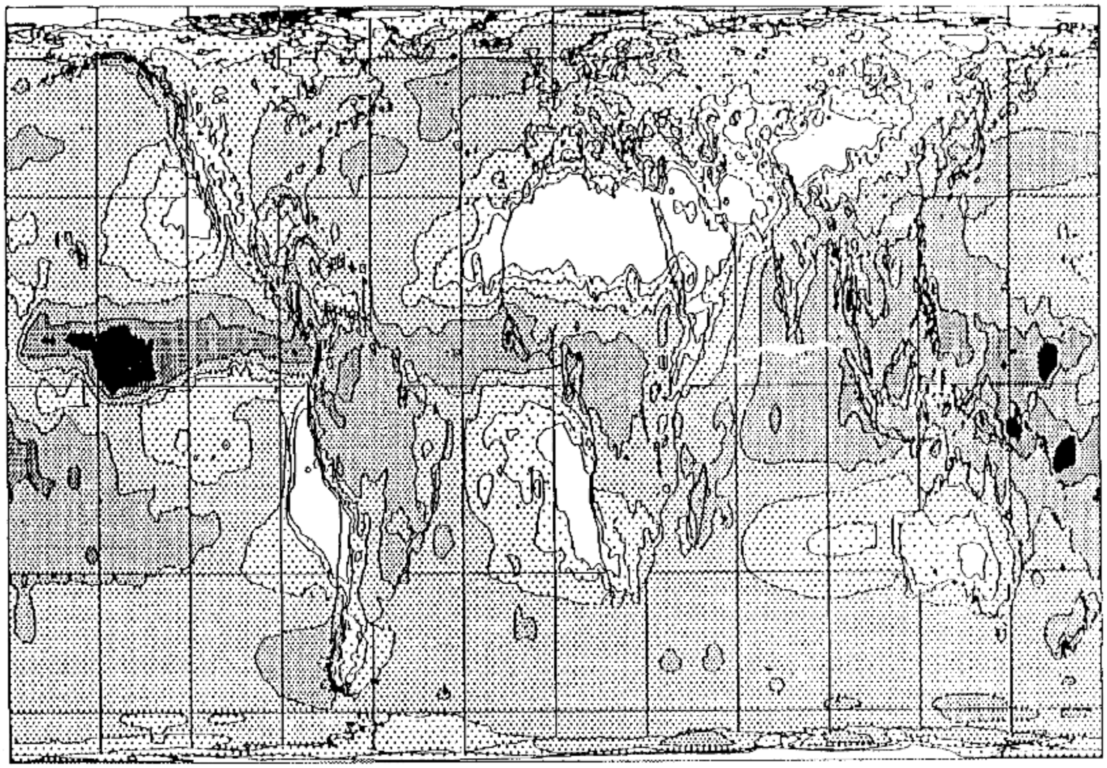

FIG. 2.4. Annual mean daily rainfall from gauge measurements taken between 1920 and 1980. Unshaded areas receive less than 0.5 mm day^{-1}, black areas receive greater than 12 mm day^{-1}, with intermediate contours at 1.0, 2.0, 4.0, and 8.0 mm day^{-1}. Source: Legates and Willmott (1990).

TABLE 2.1. Annual mean daily RR from different sources and for different surface types. Source: Xie and Arkin (1997).

Source	Surface Type	RR [mm day^{-1}]
CMAP	Ocean	3.02
	Land	1.86
	Globe	2.69
Jaeger (1976)	Ocean	2.91
	Land	2.01
	Globe	2.66
Legates and Willmott (1990)	Ocean	3.15
	Land	1.97
	Globe	2.82

In a plot by Trenberth (1998) similar to Fig. 2.4, shown in Fig. 2.5, the heaviest precipitation occurs along the ITCZ while the least occurs in the oceanic desert regions. This map also makes the heavier rainfall along the SPCZ more apparent since it is centered on the

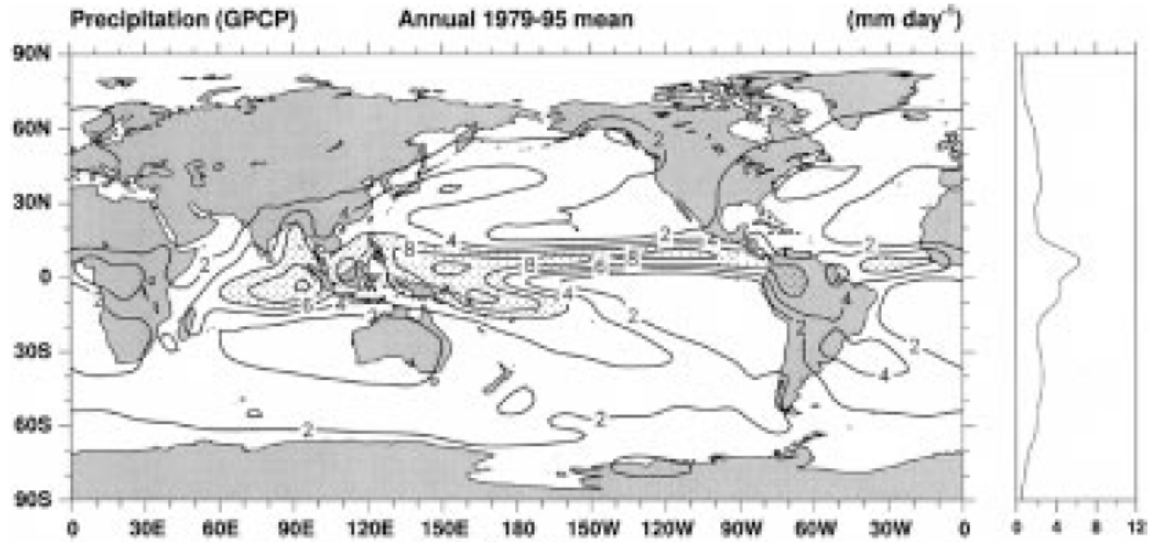

FIG. 2.5. Annual mean daily rainfall for 1979-1995. Stippled areas receive more than 6 mm day^{-1}. At right is the zonal mean profile of annual mean daily rainfall in mm day^{-1}. Source: Trenberth (1998).

Pacific Ocean. "Average precipitation rates range from almost zero to over 10 mm/day, but as rain typically occurs only about 0 to 20% of the time, actual rates conditional on rain falling can average 10 mm/h or more" (Trenberth 1998). The zonal mean daily RR is shown on the right side of this plot, which indicates the highest annual rainfall just north and south of the equator, with the highest peak occurring around 7° N, a secondary peak around 7° S, minima in the subtropics, and secondary maxima in the midlatitudes.

Figure 2.6b, which presents zonally averaged annual oceanic rainfall, displays a similar shape to Trenberth's (1998) zonal profile at the right of Fig. 2.5, with its highest peak just north of the equator, its second highest peak just south of the equator, minima in the subtropics, and secondary maxima in the midlatitude regions. "The double peak in the Tropics occurs from the preferred location of the intertropical convergence zone (ITCZ) during the course of one year at these two locations" (Kummerow et al. 2001). Interestingly, over land (Fig. 2.6a), the double peak around the equator is not present; the single peak in rainfall occurs around 2° S. In addition, over land, the secondary midlatitude maxima are also

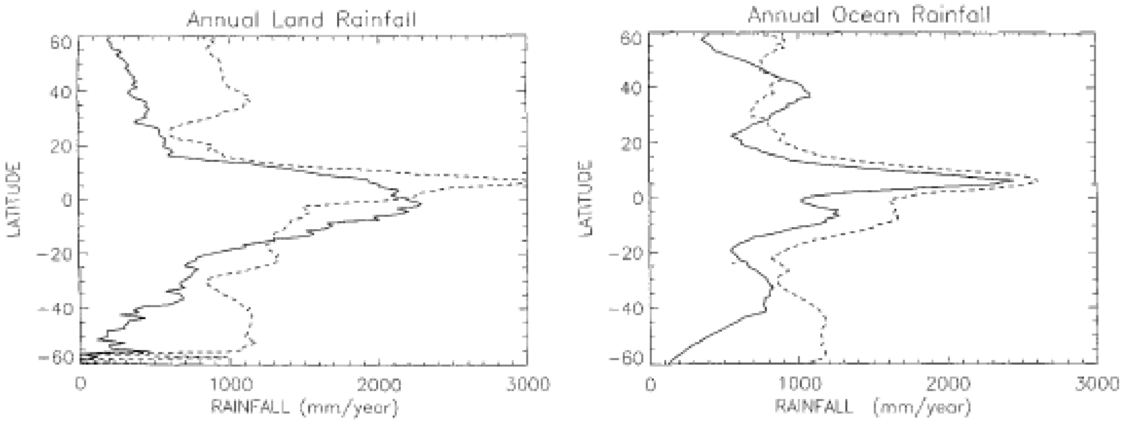

FIG. 2.6. Zonal mean annual rainfall in mm for (a) land and (b) ocean from 1987-1994 SSM/I measurements (solid) and Legates and Willmott (1990) (dashed). Source: Ferraro et al. (1996).

absent. One reason that the results from Legates and Willmott (1990) in Fig. 2.6 are greater in the midlatitudes than the Ferraro et al. (1996) findings is that Ferraro et al. (1996) use snow cover screens when performing RR retrievals. For this reason, Ferraro et al.'s (1996) rainfall estimates do not include any estimates of the water equivalent of frozen precipitation (e.g., snow) that occurs during the mid- and high-latitude winter seasons. Since Legates and Willmott (1990) included snow water equivalent estimates, their estimates of total rainfall are higher than Ferraro et al.'s (1996) in the midlatitudes.

2.3.2 Temporal Variations in Rainfall

While TPW is a continuous field, RR is discontinuous. So while atmospheric water vapor is always present, rain either is or is not occurring. It only rains over about 5-10% of the globe at any given time (Trenberth et al. 2003), with the frequency of occurrence defined in Eq. (4.1). In the midlatitudes, rain typically falls about 10% of the time (Trenberth 1998). It makes sense that rain falls most frequently over the areas that receive the most rainfall, that is, the ITCZ, SPCZ, and midlatitude storm tracks, as seen in Fig. 2.7. Just as in Fig. 2.3, Fig. 2.7 shows that the SPCZ reaches its farthest eastward during DJF and is at its weakest

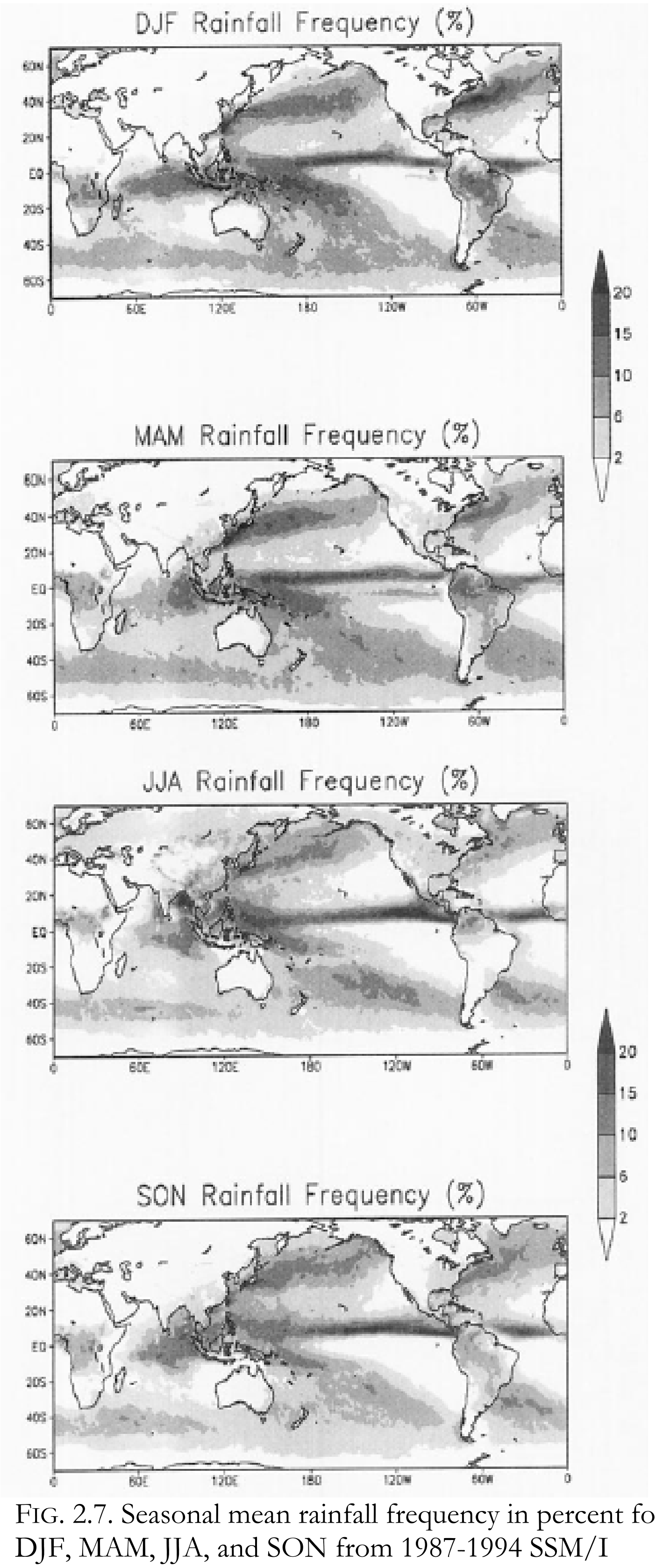

FIG. 2.7. Seasonal mean rainfall frequency in percent for DJF, MAM, JJA, and SON from 1987-1994 SSM/I measurements. Source: Ferraro et al. (1996).

during JJA, a result that is confirmed by Xie and Arkin (1997). The plots in Fig. 2.7 also indicate how much rainfall frequency varies given the 10% global average. In the southeastern Pacific oceanic desert region, for instance, the average frequency hovers around 0 to 2%. Rain is much less frequent over land than it is over the oceans, which mirror the results stated in Sec. 2.3.1 (i.e., the oceans typically receive more total rainfall than land areas). One exception is in the Amazon Basin, which receives rain nearly as frequently as the ITCZ. The ITCZ moves with the solar irradiation maximum, and this migration has a "marked effect" on the timing of precipitation in equatorial regions (Legates and Willmott 1990). The winter hemisphere land areas experience rainfall much less frequently than their summer hemisphere counterparts.

The zonal mean rainfall frequency plots shown in Fig. 2.8 display a similar shape to the zonal mean rainfall plots shown in Fig. 2.6. Over equatorial land areas, rain falls around 15% of the time and becomes less frequent with higher latitudes, with somewhat more frequent rainfall poleward of 20°. Over the ocean, rain is its most frequent around the equator as well and displays strong secondary maxima in the midlatitudes. Over any surface,

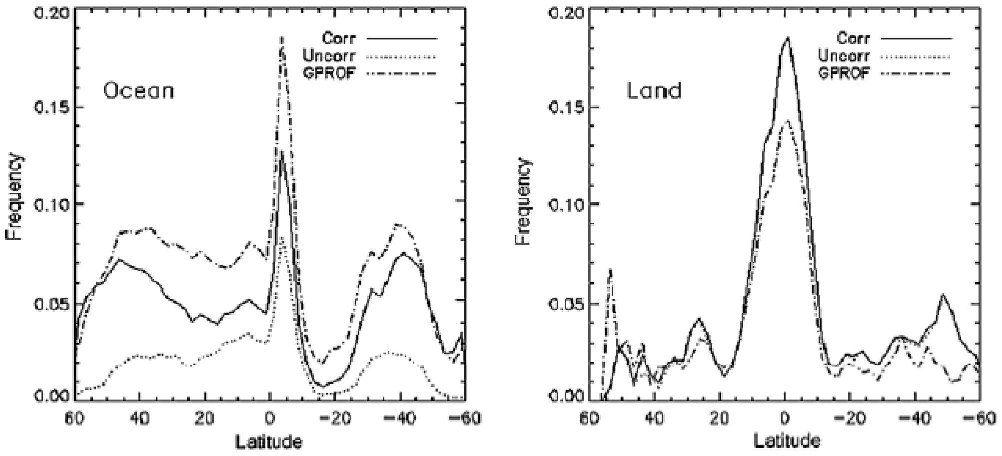

FIG. 2.8. Zonal mean frequency ratio ($RR>0 \div RR\geq0$) over (a) ocean and (b) land for AMSU-B (solid) and SSM/I (dotted and dashed) for April 2005. Source: Vila et al. (2007).

rain falls the least frequently around 20° latitude. In these plots, “over land, the AMSU-B retrieval algorithm shows a larger frequency than SSM/I GPROF V6.0…because the higher frequency channels used in AMSU-B retrievals are more sensitive to lighter rain rates” (Vila et al. 2007).

Figure 2.9 displays the zonal mean rainfall rate for April 2005. Over land, the shape of this plot is very similar to Figs. 2.6 and 2.8. Over the ocean, however, only the southern RR peak is present, and the southern subtropical minimum and midlatitude maximum are evident while their northern counterparts are not. These departures from the annual average indicate the importance of seasonal variations. Investigating the seasonal variations in precipitation is validated by Janowiak et al. (2005), who find that the highest amplitudes in the power spectrum occur at the diurnal and half-year timescales.

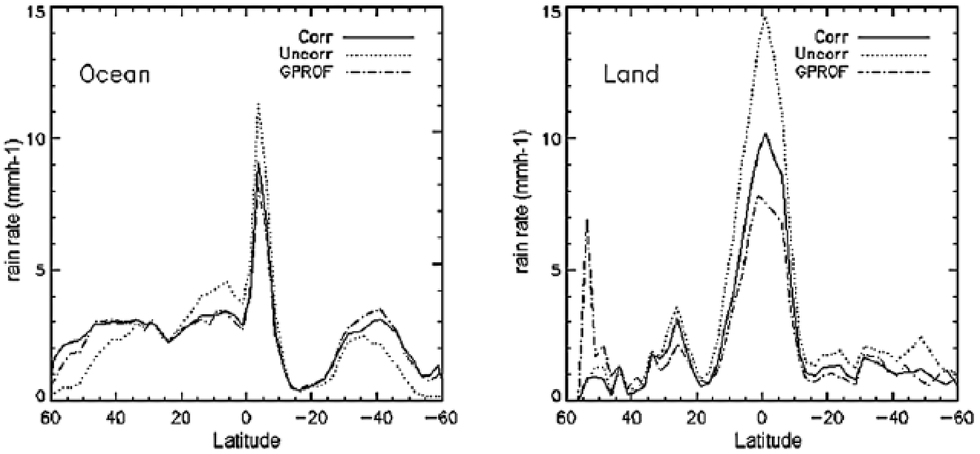

FIG. 2.9. Zonal mean rainfall rate over (a) ocean and (b) land for AMSU-B (solid) and SSM/I (dotted and dashed) during April 2005. Source: Vila et al. (2007).

Ferraro et al. (1996) calculated seasonally averaged monthly mean rainfall totals, as shown in Fig. 2.10. These plots display similar patterns to the annual mean plots, with maximum rainfall occurring in the ITCZ, SPCZ, and east coast midlatitude storm tracks. Also notable is the presence of a southern band of the ITCZ during MAM. As Legates and

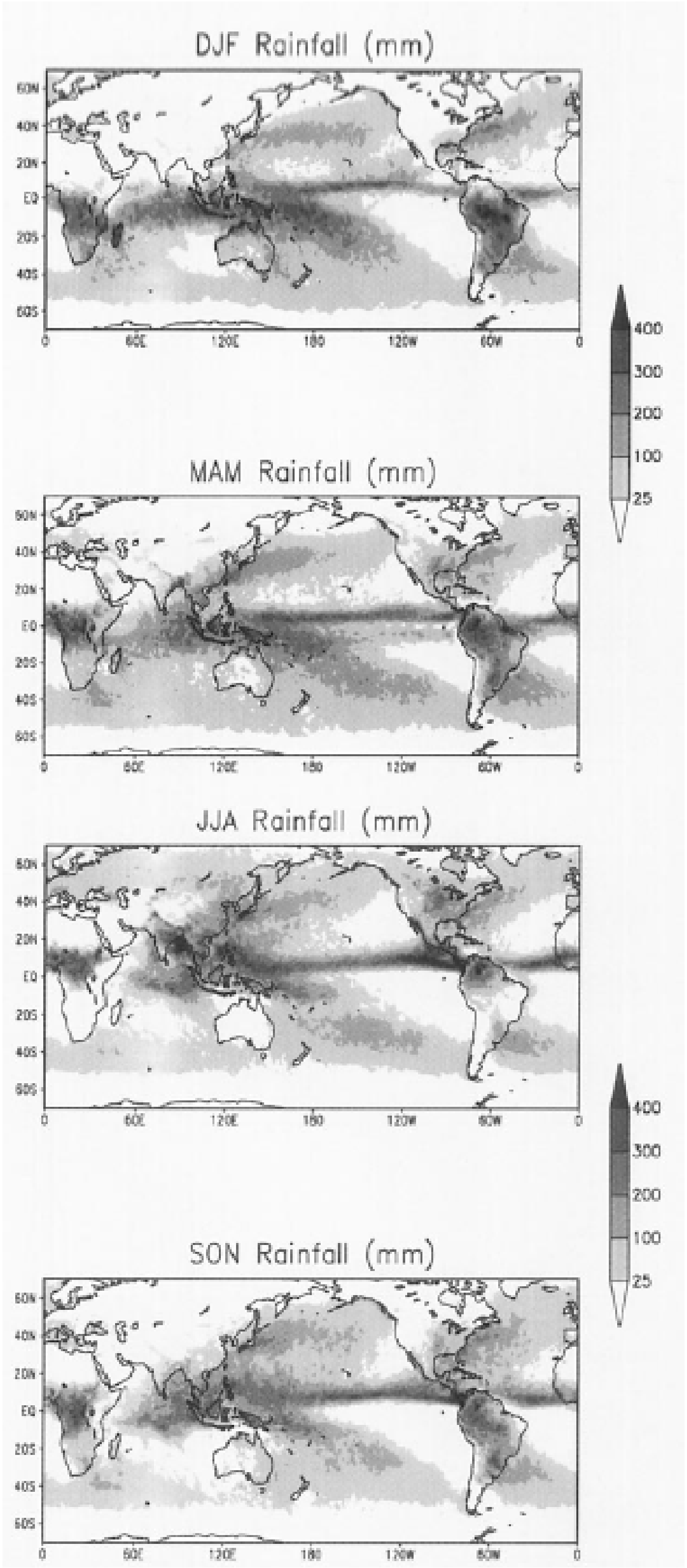

DJF Rainfall (mm)

MAM Rainfall (mm)

JJA Rainfall (mm)

SON Rainfall (mm)

FIG. 2.10. Seasonal monthly mean rainfall in mm for DJF, MAM, JJA, and SON from 1987-1994 SSM/I measurements. Source: Ferraro et al. (1996).

Willmott (1990), and now Ferraro et al. (1996), found, rainfall is much less frequent over land than it is over the ocean. Ferraro et al. (1996) explain that this is due to “the inclusion of the emission technique over the oceans,” which is not used in over-land rainfall estimation, as will be discussed further in the following chapter. When considering only the over-land rainfall, it occurs almost entirely in the SH during its summer (DJF) and in the NH during its summer (JJA). The monsoonal increase in rainfall around India and the southwestern United States during JJA is evident, as was the similar seasonal increase in TPW around those areas shown in Fig. 2.3. While the greatest United States summer rainfall totals typically occur in the southeastern United States, this study finds a midwestern United States maximum, due to “record-breaking rainfall during the summer of 1993” (Ferraro et al. 1996). Legates and Willmott (1990) find that the maximum precipitation over the subtropics occurs during the mid- to late-high-sun season.

Surface air temperature is an important factor in the occurrence of precipitation. “Precipitation between 5° N and 5° S, particularly in the Atlantic Ocean, has a March or April maximum, which coincides with the maximum surface air temperature for this region” (Legates and Willmott 1990). In addition, Legates and Willmott (1990) find that “low-latitude oceanic precipitation, especially in the subtropics of the Northern Hemisphere, is delayed for one or two months relative to terrestrial precipitation and this is coincident with the occurrence of the maximum surface air temperature” (Legates and Willmott 1990). Trenberth (1998) conducted a more focused investigation of rainfall frequency over the continental United States, displaying the seasonal changes in rainfall, as shown in Fig. 2.11. In the northwest in January, rain falls over 30% of the time. In the summer, maximum values are around 15 to 20% in the southeastern US, with the least frequent rainfall occurring in the western US. Trenberth et al. (2003), citing a study of precipitation increases

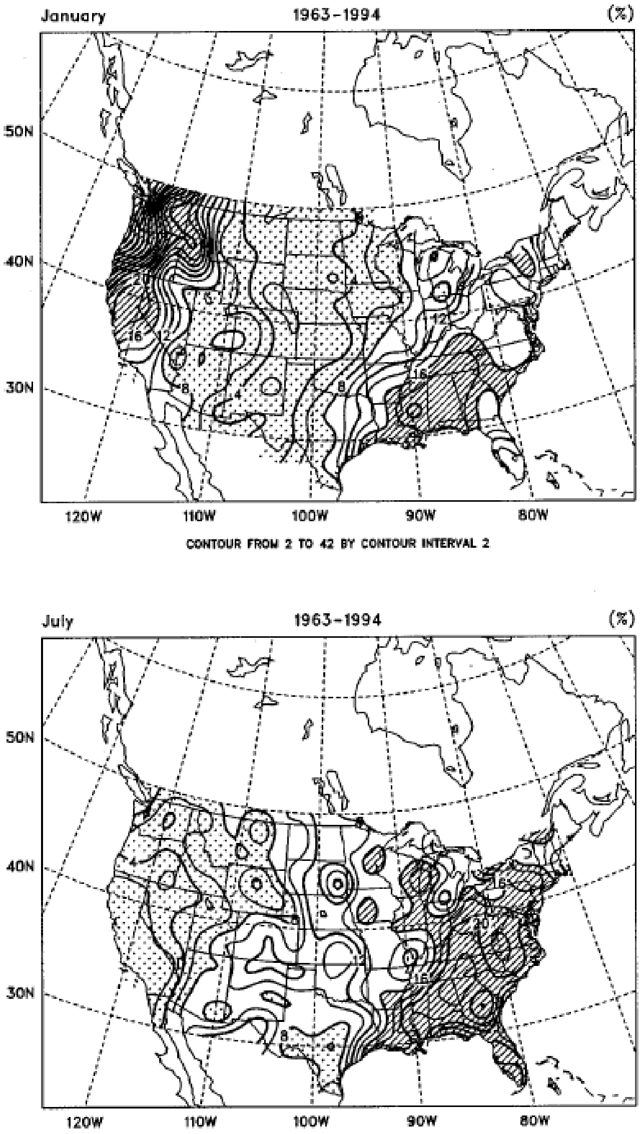

FIG. 2.11. Percentage of hours with RR ≥ 0.1 mm hr^{-1} for (a) January and (b) July from 1963-1994. Stippled areas represent values less than 8%; hatched areas represent values greater than 16%. Source: Trenberth (1998).

in the United States, state that an increase in extreme and heavy rainfall events occurs "at the expense of more moderate events," which indicates that the distributions of rainfall are variable.

2.4 A Brief Description of Global Wind Patterns

The global distribution of TPW and RR depends heavily on atmospheric dynamics. The general pattern of easterly wind flow in the tropics and westerly wind flow in the higher latitudes results from the conservation of angular momentum. The lower latitudes experience the highest amounts of solar heating. The Hadley cell is formed in part by the vertical transport of this heat and moisture in the tropics and then poleward flow of this excess heat. This poleward transport means that the air is being moved closer to the axis of the earth's rotation. According to the law of conservation of angular momentum, this air therefore must travel faster than the rotation speed of the earth. This effect is apparent in westerly flow in the higher latitudes and, contrastingly, in easterly flow in the lower latitudes. The subsidence in the subtropical latitudes, another result of the Hadley cell, contributes to impeding rainfall in the subtropics.

Surface winds "exhibit an equatorward component on the eastern sides of the oceans and a poleward component on the western sides" (Wallace and Hobbs 2006). This circulation pattern causes cool, dry air from higher latitudes to be advected toward the equator in the eastern oceans, or the 'oceanic desert' regions. Similarly, warm, moist air is advected toward the poles in the western oceans, which corresponds with the location of the storm tracks and the SPCZ in the western oceans. The ITCZ, which results from the convergence of the northeasterly and southeasterly trade winds, has a preferred location around 7° N as a result of "land-sea geometry" (Wallace and Hobbs 2006).

Because mass must always be conserved, the abundance of air at the surface that occurs when surface winds converge must result in ascending air masses, which is illustrated in Fig. 2.12a. This figure demonstrates that in the areas of converging winds (e.g., the ITCZ and SPCZ) water vapor is generally ascending. In the areas of typically diverging winds (e.g., the oceanic desert regions), water vapor generally travels downward. For comparison, Fig. 2.12b shows the annual mean rainfall from this study (Fig. 5.4). The oceanic desert regions

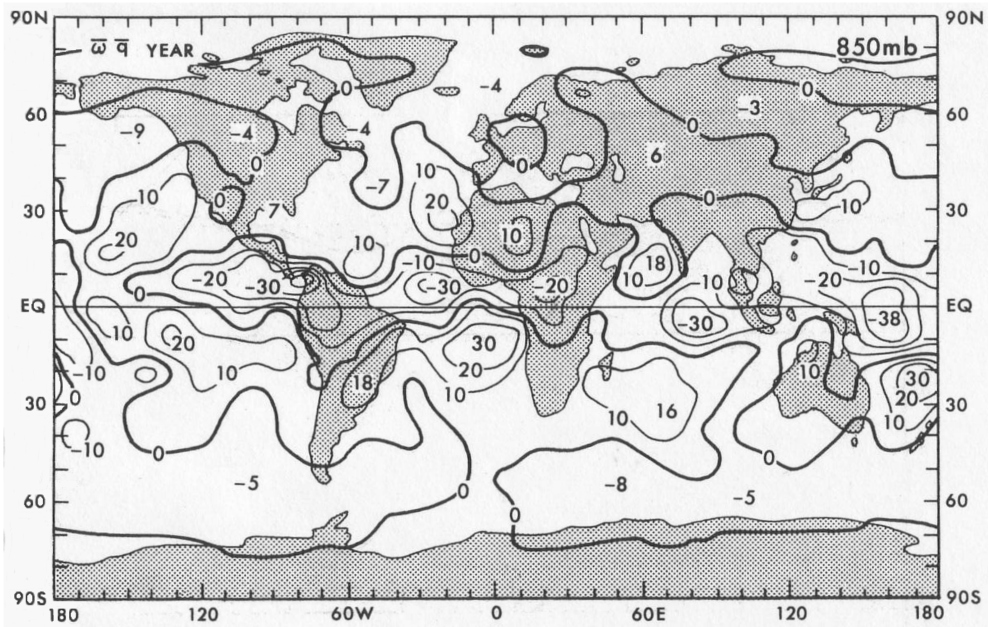

FIG. 2.12a. Global distribution of the vertical transport of water vapor at the 850-mb level, $\overline{\omega}\,\overline{q}$ in flux units of 10^{-6} kg m^{-2} s^{-1}, for annual mean conditions. Negative values indicate upward transports. Source: Peixoto and Oort (1992).

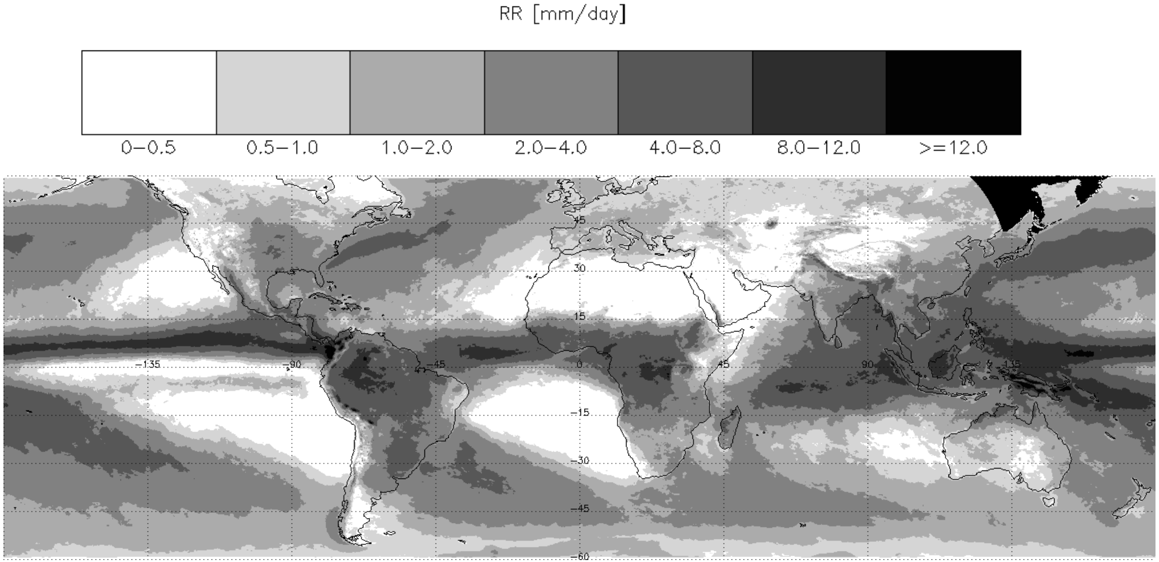

FIG. 2.12b. Annual mean daily RR in mm day^{-1} using estimates from CMORPH. The figure is the same as Fig. 5.4 but here it is centered on 0^{o} longitude for comparison with Fig. 2.12a.

of low rainfall in Fig. 2.12b correspond with atmospheric subsidence in those regions in Fig. 2.12a. Similarly, the eastern Pacific ITCZ and west Pacific warm pool areas in Fig. 2.12b, areas of higher rainfall, correspond with rising water vapor in Fig. 2.12a. Some inconsistencies do, however, exist. For instance, the northern hemisphere storm tracks in the western oceans in Fig. 2.12b are associated with sinking motion in Fig. 2.12a. These inconsistencies could be due to poor data sampling in these regions.

The occurrence of the boreal summer monsoon in southeast Asia results from a seasonal shift in wind patterns. During the summer months, southwesterly surface winds advect warm, moist air into the region. In contrast, northeasterly surface winds advect cool, dry air away from southeast Asia during the winter months (Wallace and Hobbs 2006).

In the global average, the rate of precipitation P must equal the rate of evaporation E. “Any appreciable imbalance between these terms would result in a rapid accumulation or depletion of atmospheric water vapor, which is not observed” (Wallace and Hobbs 2006). In the oceanic desert regions, E>>P; this excess atmospheric water vapor is transported toward typically moist regions (or where P>>E) by the diverging surface winds. This dependence of moisture patterns on atmospheric dynamics helps to illuminate Trenberth's (1998) statement that most of an area's rainfall results from non-local evaporation.

2.5 Regional Studies

Heavy rainfall occurs in the presence of several factors, the most important of which are sufficient atmospheric moisture, convection, and appropriate local dynamics. Since atmospheric dynamics and average TPW values vary across the globe, regional studies are necessary in order to better understand the characteristics of a particular location. Dinku and Anagnostou (2006) found there to be regional differences in the TRMM RR calibration, which is indicative of the global variety of rainfall characteristics. Thus, climatological studies are important on a global scale, but regional studies must be conducted in order to better predict particular rain events.

2.5.1 Nigeria

Ojo (1970) studied the seasonal changes in precipitable water and precipitation over Nigeria. He found that high values of TPW are found further inland during the spring and summer because of the influence of the maritime tropical (mT) air mass. Beginning in October, TPW values decrease across the country because the ITCZ "has begun to move south with the southward movement of the sun." This result reflects the findings described in Sec. 2.2 above. There is a decrease in TPW "from the coast inland in a zonal pattern" due to the different air masses influencing the country: The mT and its westerlies from the ITCZ are the greatest influence in southwestern Nigeria, while the continental tropical (cT) air mass affects the rest of the country during the dry season.

Ojo (1970) found that the decrease in precipitation during the dry season "is not caused by a lack of atmospheric moisture over the country, but by the absence of mechanisms for the release of the moisture." Thus, the presence of abundant TPW does not necessarily make rain inevitable. Ojo (1970) describes that the atmospheric dynamics and the country's topography allow the moisture to be rained out. "Drought conditions are mainly due to the absence of the mechanism for the release of the moisture, particularly because of large saturation deficits and the stable conditions of the atmosphere which characterize cT air mass." Although the higher latitudes typically have lower TPW values, cyclonic storms provide the mechanism for more rainfall in these areas. In conclusion, "the amount of precipitation is a function of the moisture content of the air as well as the degree of convergence and uplift" (Ojo 1970).

2.5.2 Sumatra Island

Wu et al. (2003) studied the diurnal variations in TPW over a mountainous area of Sumatra Island during JJA 2001. They found a large variation in TPW during that time period, ranging from 25 to 52 mm, although this range was not found on daily timescales. Over Sumatra Island, the maximum TPW occurs in the late afternoon. This phenomenon "is related to the intensity of incident solar radiation at the surface" (Wu et al. 2003). On low solar radiation days the TPW maximum is around noon, while on high solar radiation days the TPW maximum is around the late afternoon, as seen in Fig. 2.13. The maximum TPW

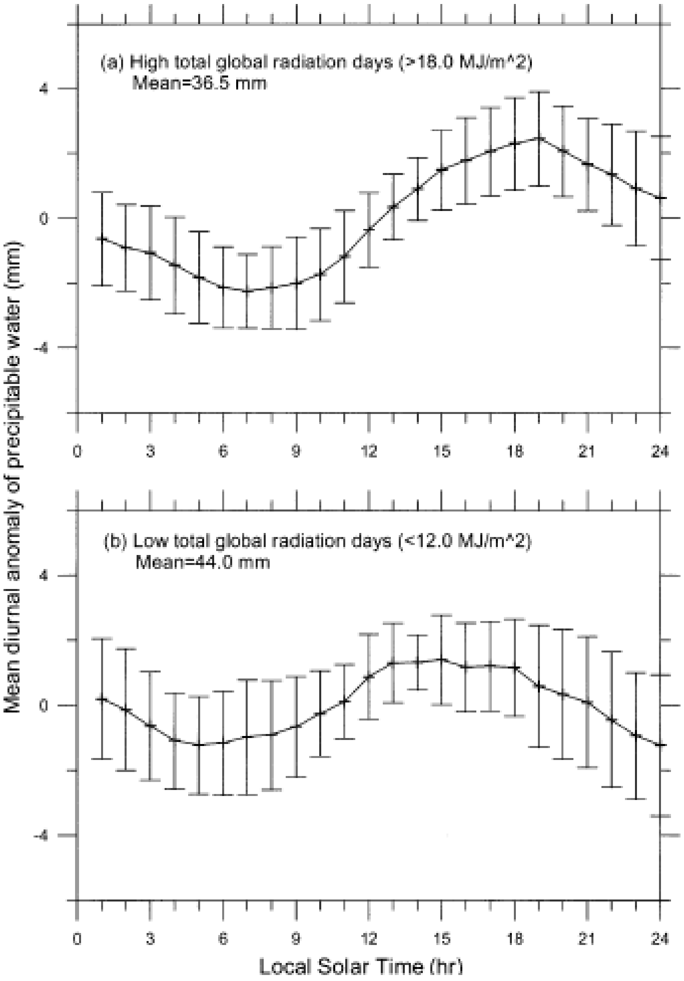

FIG. 2.13. Mean diurnal TPW anomaly on (a) high solar radiation and (b) low solar radiation days. Source: Wu et al. (2003).

on days with heavy rainfall occurs 1 to 2 hours later than on rainless days, which indicates that an increase in solar radiation in this region influences the dynamics leading to the production of rain. According to Wu et al. (2003), high solar radiation days allow for more intense local circulation, which sustains low-level convergence until later in the day.

A time series of RR and TPW shown in Fig. 2.14 indicates that there may be a TPW threshold that must be reached in order for rain to fall over the study area. During a low-TPW time period starting around July 1, there is no rainfall. Similar low TPW values around June 10 and August 13 and 18 coincide with periods lacking precipitation. Solar radiation heats the surface, inducing buoyant masses of warm, moist air to rise (i.e., convection). This ascending moist air is cooled and its water vapor may then condense into droplets. Thus solar heating and convection are important dynamical factors for the incidence of rainfall. A comparison of TPW and RR time series in this study indicates that a satisfactory TPW may need to be surpassed in order for rain to fall.

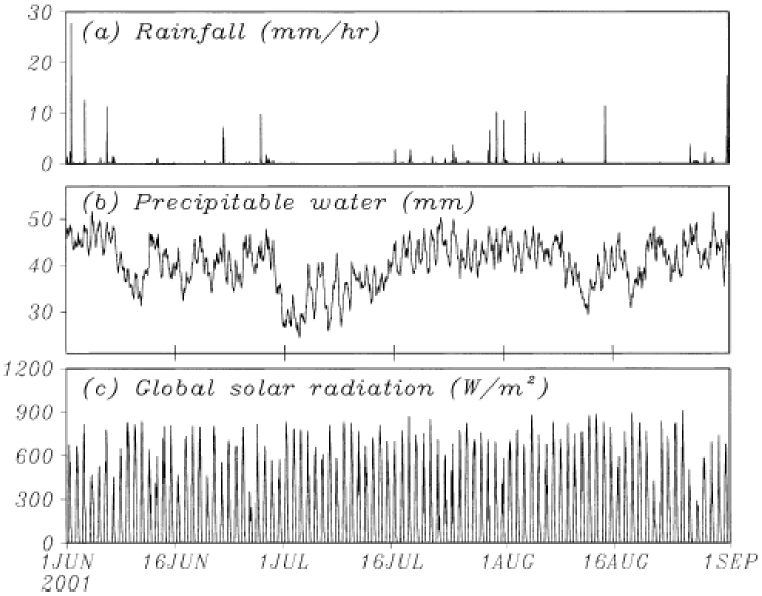

FIG. 2.14. Time series of (a) RR in mm hr^{-1}, (b) TPW in mm, and (c) global solar radiation at the Koto Tabang GPS station during JJA 2001. Source: Wu et al. (2003).

2.5.3 Heavy Rainfall Events

Smith et al. (1996) studied a catastrophic rainfall event in the Blue Ridge Mountains of Virginia on June 27, 1995 that caused flash flooding as a result of "rainfall accumulations exceeding 600 mm in a 6-hour period." Predicting the intensity of such an event would be beneficial in terms of early warning for people who may be in the area. Better understanding the causes of these heavy rain events is also important because they initially may not appear threatening: "a striking feature of the Rapidan storm was its small size and long duration." The Appalachian Mountain terrain was very important in this case—the interaction of the terrain with the dynamics of this storm led to this heavy rainfall event. The convection that triggered the instability anchored the cloud to the mountains, since the upslope winds continually fed moisture into the storm. Thus, even this small storm was long-lived. Although the presence of elevated TPW was necessary for rainfall, the "orographic features played an important role in regulation of atmospheric moisture inflow to the storm."

Junker et al. (2008) studied heavy rainfall in the Northern California mountains. The heaviest precipitation during this study occurred during the winter months (NDJFM), with no events during the summer months (JJAS), which is attributed to the higher moisture flux into the area during those cold months. Although TPW values during the winter months are lower than typical summer TPW values, the heavier rain events occur during the winter months as a result of seasonal synoptic-scale flow patterns. During the winter months, stronger than normal southerly flows transport heat and moisture northward to the areas that experience the very heavy rainfall. These results support the findings by Trenberth (1998), who noted that the most frequent rainfall over the northwestern United States occurs during the NH winter. In addition to the presence of "highly anomalous" TPW, or 'atmospheric rivers,' each case of extreme rainfall during this study was associated with an “unusually intense” negative geopotential height anomaly. The Junker et al. (2008) findings agree with a previous study that described how this negative height anomaly was associated with the 20 heaviest rainfall cases in the same region between 1948 and 1988. They find that these atmospheric rivers are always associated with heavy precipitation, but not with light precipitation. The parameters most highly correlated with heavy precipitation were the 700 hPa moisture flux anomalies and the 850 hPa moisture flux anomalies, both at least 5σ greater than normal during this study. In addition, TPW anomalies were also significantly correlated with heavy precipitation, as were atmospheric instability, latent heat release, and synoptic and mesoscale forcing. In sum, anomalously negative geopotential heights are important for the occurrence of heavy precipitation in Northern California during the NH winter, in addition to the occurrence of anomalously high TPW values.

Keighton et al. (2001) observed flash flood-producing rain events in the Appalachian Mountains between July 2000 and March 2001 using TPW data from local GPS sites and RR measurements from local rain gauges. They note that several factors contribute to the production of such heavy rain, such as TPW, atmospheric instability, and storm evolution. Non-atmospheric contributors to flash flooding events include soil moisture conditions, the steepness of the terrain, the presence of vegetation, and the area type (i.e., urban vs. rural).

Mainville (2004) studied heavy rainfall over Québec, finding that heavy convective rainfall accounts for around half of summer severe convective weather events in that region. Trenberth (1998) came to a similar conclusion in monsoon regions, finding that 70 to 85% of the rainfall results from periods of heavy RR, or RR $\geq$10 mm hr^{-1}. As Wu et al.'s (2003) results indicate a possible TPW threshold for the occurrence of rain, Mainville (2004) determined that a TPW value of $\geq$35 mm is necessary for heavy convective rainfall over Québec. Mainville's (2004) results also mirror those of Wu et al. (2003) in that they find diabatic heating to be a strong influence on daytime and early evening convection. In contrast, night-time convection is more strongly influenced by dynamic effects. In this region, Mainville (2004) finds the interaction between high TPW values and local dynamics to be the deciding factor in the production of heavy rainfall. "Several processes must take place in order to favour a high rainfall rate. A weak vertical environmental shear slows the weather system as well as the components responsible for convection, allowing the rain to fall over the same area. In addition, this weak shear coupled with parallel low-level and upper-level jets reduces dry air entrainment, and consequently restricts in-cloud evaporation of the rain drops. High drop density develops with a long narrow CAPE profile as it indicates slow updraft acceleration. Collision and coalescence processes thus take place over a longer period of time. These processes easily prevail when the environment contains high humidity, as pointed out by high magnitudes of precipitable water content, and when humidity is advected by the low-level jet towards the convergence axis. In addition, a lifting condensation level close to the surface limits evaporation under the cloud base" (Mainville 2004).

2.5.4 Eastern Pacific Ocean

Neelin et al. (2009) studied tropical convective storms over the eastern Pacific Ocean. This study assigned critical TPW values to each system, above which precipitation becomes very likely. They found that sea surface temperature (SST), rather than directly influencing individual occurrences of precipitation, influences the climatological frequency of occurrence, "consistent with large-scale forcing typically being larger over warmer SST." In individual tropical convective events, however, the critical TPW and occurrence of precipitation depends "only on the tropospheric water vapor and temperature." As Wu et al. (2003) and Mainville (2004) found over Sumatra Island and Québec, respectively, there appears to be a threshold TPW value such that, once surpassed, the occurrence of rainfall becomes more likely. Neelin et al. (2009) found that, although precipitation became more likely with TPW values above criticality, the occurrences of those very high TPW values are infrequent. Thus, "significant contributions to precipitation are confined to a relatively narrow range just below and above criticality." Following this study, Muller et al (2009) made the assumption that, "when deep convection is occurring, more free tropospheric humidity leads to more rainfall," since "surface evaporation provides a slow, continuous forcing bringing the atmosphere towards this threshold, while convection events rapidly dissipate instability after it is generated". The contribution of local evaporation to the occurrence of rainfall goes against the assertion by Trenberth (1998) that local evaporation is relatively unimportant in a region's precipitation patterns.

In the eastern Pacific, the most common vertically averaged tropospheric temperature was $\hat{T}$ =270 K. Average RR values are compared with TPW for different tropospheric temperature values in Fig. 2.15. For this tropospheric temperature value, 95%

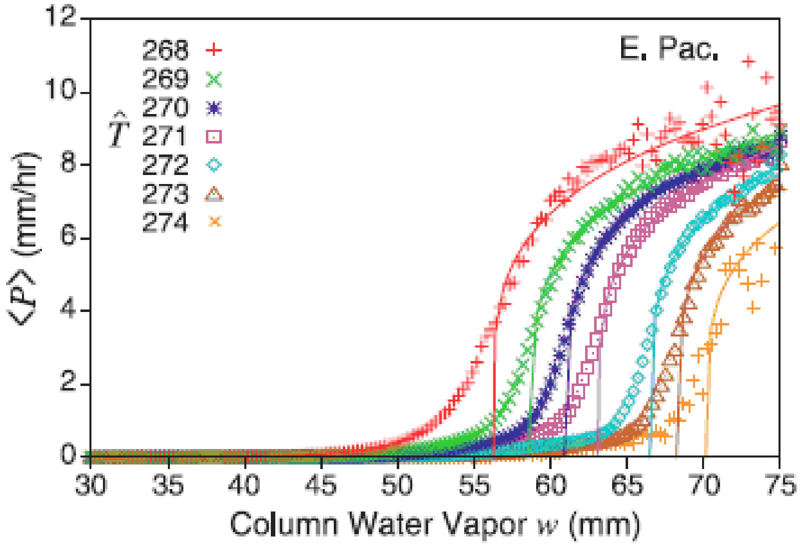

FIG. 2.15. Average rainfall rate versus column water vapor for the eastern Pacific for various tropospheric temperatures. Source: Neelin et al. (2009).

of the rainfall occurs at TPW values greater than 2 standard deviations below the critical TPW value and 25% of the rainfall occurs for TPW values greater than the critical TPW value. So while a significant amount of rain falls at TPW values surpassing the critical value, 75% of the rain still occurs at TPW values below the critical value. Figure 2.15 shows the average rainfall rate as a function of TPW for various values of vertically averaged tropospheric temperature $\hat{T}$. This plot indicates that a TPW threshold does exist for tropical convection in the eastern Pacific, where TPW values above this threshold coincide with increased rainfall amounts, although this threshold may have a tropospheric temperature dependence. As this study and the other studies described in Sec. 2.5 indicate, the occurrence of rainfall appears to have a TPW dependence, but region-specific dynamics also play an important role in the creation of rainfall.

2.5.5 Tropical Cyclones

Xiao et al. (2000) studied the influence of TPW and RR data on tropical cyclone forecasts. They assimilated TPW and RR data from SSM/I observations into the Pennsylvania State University-NCAR Mesoscale Model version 5 in order to determine how well the model forecasts of tropical cyclones improved given these improved initial conditions. They found that "the forecasts initialized with the optimal initial conditions are improved." Both the prediction of cyclone tracks and rainfall were improved. Thus, incorporating SSM/I TPW and RR observations into forecast models has "great potential for improving cyclone prediction."

3. INSTRUMENTATION AND DATA PRODUCTS

3.1 Total Precipitable Water

TPW can only be confidently measured by satellites over the oceans because TPW retrieval over land is complicated by the high (i.e., 0.9 on average) and highly variable emissivities of land surfaces. The emissivity of an ocean surface is fairly uniform globally and is closer to 0.5 (Ferraro et al. 1996, 2005). The passive microwave TPW retrievals are emission-based and rely on a radiometrically cold background, so that the presence of atmospheric emitters (e.g., water vapor) increases the observed brightness temperature above the surface brightness temperature. "The brightness temperature change due to sea surface emissivity variations is generally small compared to the transmittance variations due to water vapor and liquid water" (Grody et al. 2001). Since land surfaces have high and highly variable emissivities, detecting variations in atmospheric emission against a relatively warm background is difficult. In this way, over-land retrievals are relatively inaccurate, whereas over-ocean retrievals are much more reliable. The brightness temperatures at the top of the atmosphere contain three contributions: "the surface emission, the upwelling atmospheric radiation, and the downwelling atmospheric radiation reflected at the surface" (Grody et al. 2001).

3.1.1 SSM/I

The Special Sensor Microwave Imager (SSM/I) is a radiometer aboard the Defense Meteorological Satellite Program (DMSP) F-13, -14, and -15 satellites (Joyce et al. 2004).

According to Ferraro and Marks (1995), each SSM/I instrument contains seven channels: 19.35 horizontal and vertical polarizations (H & V), 22.235 V, 37.0 H & V, and 85.5 H & V GHz. TPW is an accurate parameter retrieved by passive microwave sensors, with errors near 10% when compared with radiosonde measurements (Ferraro et al. 1996). "Since most of the moisture is in the lower atmosphere, below 700 mb, these retrievals are strongly coupled with sea surface temperature" (Ferraro et al. 1996). The over-ocean TPW retrieval makes use of the lines at 19.35, 22.235, and 37.0 GHz (Kidder and Jones 2007). The National Environmental Satellite, Data, and Information Service (NESDIS) algorithm described by Ferraro et al. (1996) takes the form:

$$TPW = 232.89 - 0.1486(Tb_{19V}) - 0.3695(Tb_{37V}) - [1.8291 - 0.006193(Tb_{22V})]Tb_{22V} \quad (3.1)$$

$$TPW(corrected) = -3.753 + 1.507(TPW) - 0.01933(TPW^2) + 0.0002191(TPW^3)\,, \quad (3.2)$$

where "the first equation is the original algorithm, while the second equation is a cubic correction of the TPW in low- and high-TPW regimes" (Ferraro et al. 1996).

Measurements of upwelling radiance have the "best accuracy" at local zenith angles near 54 degrees (Weng et al. 2003). The SSM/I sensor takes all of its measurements at a constant viewing angle near 54 degrees from nadir.

3.1.2 AMSU-A2

The Advanced Microwave Sounding Unit-A2 (AMSU-A2) is a radiometer aboard the National Oceanic and Atmospheric Administration (NOAA) -15, -16, and -17 satellites. Weng et al.'s (2003) atmospheric absorption-based TPW algorithm works using the 23.8 and 31.4 GHz channels. This instrument scans the domain using viewing angles from 1.2 to 57.3 degrees from nadir, resulting in an angle-dependent algorithm since the viewing angle "alters the surface emissivity, increases the path length, and enlarges the footprint" (Grody et al. 2001).

TPW is calculated from the 23.8 and 31.4 GHz channels by:

$$\text{TPW} = b_0\mu[\ln(T_s - Tb_{31}) - b_1\ln(T_s - Tb_{23}) - b_2], \tag{3.3}$$

where b_0, b_1, and b_2 "are coefficients based upon the atmospheric absorption (water vapor, cloud water, and oxygen) and sea-surface emissivity, μ is the cosine of the local zenith angle, T_s is the sea-surface temperature, and Tb_{23} and Tb_{31} are the AMSU brightness temperatures at 23 and 31 GHz, respectively" (Ferraro et al. 2005). The coefficients are described by Weng et al. (2003):

$$b_0 = 0.5\kappa_{l23}/(\kappa_{v23}\kappa_{l31} - \kappa_{v31}\kappa_{l23}) \tag{3.4}$$

$$b_1 = \kappa_{l31}/\kappa_{l23} \tag{3.5}$$

$$b_2 = [-2.0(\tau_{o31} - b_1\tau_{o23})/\mu] + (1.0 - b_1)\ln(T_S) + \ln(1.0 - \varepsilon_{31}) - b_1\ln(1.0 - \varepsilon_{23}), \tag{3.6}$$

where $\varkappa_v$ and $\varkappa_l$ are the water vapor and cloud liquid water mass absorption coefficients, respectively. $\varkappa_l$ can be expressed in terms of cloud layer temperature T_l:

$$\kappa_l = a_l + b_lT_l + c_lT_l^2. \tag{3.7}$$

Oxygen optical thickness is given by:

$$\tau_o = a_o + b_oT_S. \tag{3.8}$$

The parameters for $\varkappa_v$ a_l, b_l, c_l, a_o, and b_o are described in more detail by Weng et al. (2003) and are validated against ground-based radiometer measurements.

3.1.3 CIRA Blended TPW Product

Although TPW data from the SSM/I and AMSU-A2 sensors are only available over the ocean, the Cooperative Institute for Research in the Atmosphere (CIRA) blended TPW product (bTPW) also incorporates data from the Global Positioning System Meteorology (GPS-Met) ground-based receiver network located across the continental United States (CIRA Experimental Merged Total Precipitable Water Products Website). Integrating GPS-retrieved water vapor into numerical weather prediction models has had varying degrees of success, depending on the region and the season, but ultimately is a help rather than a hindrance to precipitation prediction (Marcus et al. 2007).

The bTPW data are available hourly from 71° N to 71° S, with 16 km resolution at the equator (Kidder and Jones 2007). The initial motivation for the bTPW product was for use in forecasting, so that TPW measurements from different sources may be examined in one plot with the minimal presence of satellite scan lines. However, as is evident in this study, this dataset is useful for quasi-global and regional climatologies of TPW as well.

TPW values from the AMSU and SSM/I, because they are different instruments, have different statistical properties (Kidder and Jones 2007). Because plotting values from both instruments on the same map introduces discrepancies as a result of these statistical differences, users are distracted and are unable to determine if a sharp TPW gradient is a physical phenomenon or simply an artifact of the individual swaths. The CIRA bTPW is formed in three steps. First, a histogram of TPW values is constructed for the latest 5 days of data for each instrument. "The assumption is that in a 5-day period, each scan position of each instrument will sample the global distribution of TPW" (Kidder and Jones 2007). The second step is constructing a reference probability distribution function (PDF). The reference instrument is the NOAA-17 AMSU since it was the newest of the three AMSU instruments and no data were available to show any superiority of the SSM/I TPW values over the AMSU TPW values. The third step is to construct an adjustment for each scan position of each instrument, all using the same reference PDF. SSM/I values are fitted to the reference values by a cubic polynomial fit. By conforming all measurements to the reference PDF, the presence of artifacts is reduced and a smoother map of global TPW is created. A composite map of all available data is created hourly using all the available data accumulated in the previous 12 hours.

3.2 Rainfall Rate

RR can be measured over land as well as over ocean because the algorithms used can detect radiation scattered from precipitation, independent of the land surface background, which, as previously discussed, is highly variable. RR algorithms are both emission- and scattering-based. Emission-based algorithms work over oceans because they appear 'cold' without the presence of rain, due to a surface emissivity around 0.5. When rain is falling, it emits radiation at its own temperature with an emissivity near 1.0 (Spencer 1986), acting to increase the observed brightness temperature (Tb) (Kummerow et al. 1996). In contrast, "scattering acts to lower the Tb below what would have been observed for a land background alone" (Spencer 1986).

Rainfall rate retrievals are more error-laden than TPW retrievals. "The passive microwave methods try to relate the attenuation of the upwelling ocean emitted radiation by hydrometeors in the atmosphere to a rain rate. This is extremely difficult to do accurately because the attenuation (absorption and scattering) is a function of many different parameters. These include rain water, cloud water, and ice contents and their vertical distributions, atmospheric temperature and humidity; these factors vary within the microwave radiometer's field of view" (Spencer 1986). In addition, the wind at the ocean's surface affects its emissivity (Wilheit et al. 1977). Scattering-based algorithms rely on the presence of ice to detect rain, so shallow convective and weak stratiform rain are not as readily detected. The same is true for orographically induced rain (Ferraro and Marks 1995). Although all these error sources are present, the retrieved RRs have been independently verified for several cases. For instance, TMI RRs matched well with those from a robust model simulation (Kummerow et al. 1996) and Ferraro and Marks (1995) describe various validation studies.

3.2.1 SSM/I

The same SSM/I sensors used to retrieve TPW are used for the rainfall rate retrieval. The SSM/I sensors compute RR using the NOAA/NESDIS/Office of Research Applications SSM/I combined scattering- and emission-based algorithm over the oceans and scattering-based algorithm over land. According to Ferraro (1997), this algorithm "performs its best during the convective season and its worst during stratiform rain regimes." That is, this algorithm works the best for relatively heavy rainfall events and for rain initiated in clouds containing ice.

Over the ocean, a "combined 85 GHz scattering and 19/37 GHz emission" algorithm is used to measure RR (Ferraro 1997). SSM/I detects emitted radiation from raindrops and scattered radiation from precipitation-sized ice particles. The scattering index (SI) is calculated over water using:

$$SI_W = [-174.4 + 0.72 \times Tb_{19V} + 2.439 \times Tb_{22V} - 0.00504 \times Tb_{22V}^2] - Tb_{85V}\,, \tag{3.9}$$

where Tb indicates brightness temperature in Kelvin. Using this scattering index, RR is estimated using:

$$RR = 0.00188 \times SI_W^{1.0343}\,, \tag{3.10}$$

where RR is in mm hr^{-1}. When RR is greater than 35 mm hr^{-1}, the value is set to 35 mm hr^{-1} because RR increases "exponentially for higher SI values" (Ferraro 1997).

Over land, an 85 GHz scattering-based algorithm is used to measure RR. The SI is calculated using:

$$SI_L = [451.9 - 0.44 \times Tb_{19V} - 1.775 \times Tb_{22V} + 0.00575 \times Tb_{22V}^2] - Tb_{85V} \tag{3.11}$$

and the resulting over-land RR is estimated using:

$$RR = 0.00513 \times SI_L^{1.9468}. \tag{3.12}$$

This algorithm does not retrieve rain over snowy surfaces, which means that relatively few rain estimates are made during the cold season, "particularly in the northern hemisphere, which has expansive snow cover during December, January, and February" (Ferraro 1997).

This algorithm uses a 10 K minimum threshold for SI values, which corresponds to a minimum detectable RR of 0.45 mm hr^{-1} over land and 0.20 mm hr^{-1} over ocean. If the SI is less than 10 K over ocean, "a liquid water emission technique is applied, since an ice scattering signature may not be present in many mid- and high-latitude rain systems or in tropical warm rain" (Ferraro 1997). This technique comprises liquid water estimates (Q) using different channels:

$$Q_{19} = -2.70[\ln(290 - Tb_{19V}) - 2.84 - 0.40\ln(290 - Tb_{22V})] \tag{3.13}$$

$$Q_{37} = -1.15[\ln(290 - Tb_{37V}) - 2.99 - 0.32\ln(290 - Tb_{22V})]. \tag{3.14}$$

If Q_{19} is greater than 0.60 mm or if Q_{37} is greater than 0.20 mm, a RR is calculated using the relationship from Ferraro and Marks (1995):

$$RR = 0.001707(100Q)^{1.7359}, \tag{3.15}$$

Using this alternative emission-based over-ocean algorithm, the minimum RR is 0.30 mm hr^{-1}, while RRs greater than 35 mm hr^{-1} are set to 35 mm hr^{-1}, as in the original scattering- and emission-based algorithm (Ferraro 1997).

The SSM/I RR algorithm performs "best in the tropics and summer seasons of the midlatitudes…and worst in the high latitudes and in the transition seasons," since estimates over snow cover are not possible (Ferraro 1997). This algorithm caps its RR estimates at 35 mm hr^{-1}, but rare storms, such as the one described by Smith et al. (1996) in Sec. 2.5.3, can exceed these thresholds, leading to underestimates. For instance, "peak rainfall rates exceeded 300 mm hr^{-1} during two pulses of heavy rainfall," and "above 100 mm hr^{-1} on multiple occasions" (Smith et al. 1996). Although these instances of heavy rainfall are infrequent, they do occur. As more instances of heavy precipitation may be possible as the climate changes, it becomes more important to adequately characterize these types of events (Trenberth 1998).

3.2.2 TRMM

The Tropical Rainfall Measuring Mission (TRMM) Microwave Imager (TMI) instrument is nearly identical to the SSM/I, with the exceptions that a dual-polarized 10.7 GHz channel has been added and that the water vapor channel is moved to 21.3 GHz (from 22.235 GHz) "to avoid saturation in the tropics" (Kummerow et al. 1996). Once a channel becomes saturated, with unit absorptance, any additional emission at that frequency cannot be detected by increasing absorptance values. Rain rate is estimated using the Goddard Profiling Algorithm (GPROF), which "relates the vertical profiles of liquid and ice to surface rain rates in a radiative model context" (Joyce et al. 2004).

GPROF retrieves the vertical structure of the precipitation due to fact that the different channels' response functions peak at different levels in the raining column. Several possible vertical profiles, generated by the Goddard Cumulus Ensemble model, are used to determine the probability of a particular brightness temperature. GPROF varies this "assumed rain structure in order to minimize the differences between observed and modeled radiances" (Kummerow et al. 1996). Radiative transfer calculations then determine the brightness temperature given this vertical distribution of hydrometeors. A more detailed description of the retrieval process is described by Kummerow et al. (1996). Figure 3.1 is the flow chart they present describing the process of converting brightness temperature to RR.

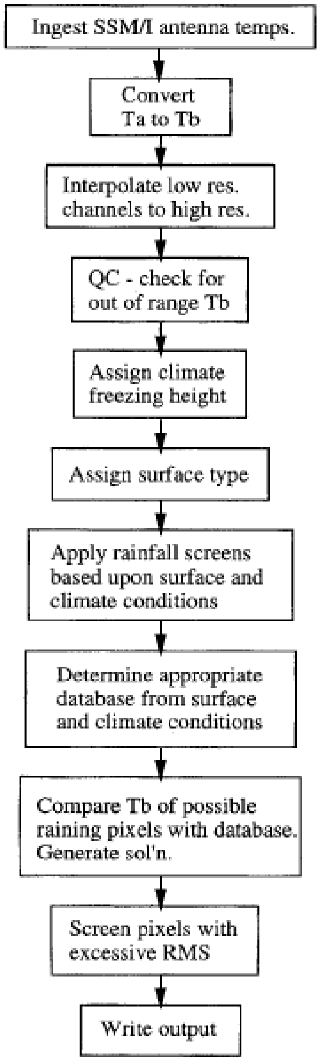

FIG. 3.1. Flow chart of GPROF RR algorithm.
Source: Kummerow et al. (1996).

As with the SSM/I RR algorithm, GPROF uses both emission- and scattering-based techniques to retrieve RR. GPROF defines RR as "the precipitation liquid present in the lowest 0.5 km of the cloud structure" (Kummerow et al. 1996). The lower frequency channels (10, 19, 21, and 37 GHz) detect the thermal emission of raindrops and the higher frequency channel (85 GHz) detects the upwelling radiation scattered from ice particles, which are commonly found in raining clouds (Joyce et al. 2004). The scattering technique works because "scattering acts to reflect upwelling radiation back to the surface, lowering the observed brightness temperatures" below what they would be if no ice particles were present (Kummerow et al. 1996). The emission technique has a physical basis, directly detecting an increased brightness temperature due to raindrops' emission against a cold background. The scattering technique, however, "must infer the precipitation based upon a measure related to the ice content of the cloud. This makes scattering algorithms more susceptible to regional and temporal biases" (Kummerow et al. 1996). Over land, since the algorithm mainly depends on the 85 GHz scattering signal, the mean hydrometeor structure is retrieved. Over the oceans "more radiometric signal is available," so more vertical structure can be discerned.

GPROF was compared to a scattering-based technique and to an emission-based technique. The correlations between each of those algorithms and GPROF were shown to be higher than when the one-technique results were compared with each other. This means that using both scattering and emission signatures results in an improved model (Kummerow et al. 1996). TMI and SSM/I measurements were also compared to the TRMM precipitation radar (PR) rainfall estimates, as described in a validation study by Dinku and Anagnostou (2006).

Improvements were made to the GPROF retrieval algorithm after it had been active for a few years, as described by Kummerow et al. (2001). For instance, the updated algorithm better distinguishes between convective and stratiform regions. Convective regions "are characterized by locally strong updrafts and downdrafts," which are associated with strong horizontal variations in precipitation, while stratiform regions are characterized by "relatively weak and horizontally uniform updrafts and downdrafts," which are associated with uniformly distributed precipitation. Using the earlier algorithm, rainfall was overestimated in stratiform rain regions. The improved algorithm results in significantly decreased precipitation amounts in "stratiform areas, especially in those areas far from convection." Another change was the improved pixel-screening method, which determines whether a pixel is raining, not raining, or unclassifiable. The improved method uses the pixels in the vicinity of an unclassifiable pixel to determine if the surrounding pixels are mostly classified as raining or not raining. If the majority of surrounding pixels agree, the unclassifiable pixel is classified to match the pixels in its vicinity (Kummerow et al. 2001).

GPROF tends to overestimate small liquid water contents corresponding to RRs less than 3 mm hr^{-1}, but produces accurate estimates corresponding to RRs between 3 and 15 mm hr^{-1}. "At low rainfall rates, light uniform rain tends to have very similar brightness temperature signatures as heavier, more variable rain. Since these signatures are indistinguishable to a microwave sensor, the weighted average of profiles carried out by the retrieval tends to overestimate the very light rainfall amounts. At the high rainfall end, saturation of the brightness temperature signal is responsible for the underestimation" (Kummerow et al. 1996). However, when information from the 10 GHz channel is added to the TMI retrievals, the overestimates at low RRs and underestimates at high RRs are minimized since the 10 GHz channel does not saturate as quickly as the 19 GHz channel.

3.2.3 AMSU-B

The Advanced Microwave Sounding Unit-B (AMSU-B) is a multi-channel radiometer aboard the National Oceanic and Atmospheric Administration (NOAA) -15, -16, and -17 polar-orbiting satellites (Joyce et al. 2004). It contains one channel at both 89 and 150 GHz and three channels centered on 183.3 GHz: 183.3 ± 1, 3, and 7 GHz (Weng et al. 2003; Ferraro et al. 2005). Since only these high frequency channels are available, "only precipitation detectable from a scattering signature can be estimated" (Vila et al. 2007). The NESDIS RR algorithm works by performing a physical retrieval of the ice water path (IWP) associated with “thick and precipitation ice clouds” (Weng et al. 2003). However, a distinction must be confirmed between atmospheric and surface scatterers since “the scattering signature resulting from sea ice and snow particles at higher microwave frequencies is similar to that of the ice particles because the dielectric constants among these scatterers are almost the same” (Weng et al. 2003).

IWP is calculated using the ice cloud scattering parameter, which can be derived using the 89 and 150 GHz measurements. The coefficients in the equations used to calculate IWP are dependent upon effective ice particle diameter and ice particle bulk volume density, assuming the ice particles follow a gamma distribution. See Ferraro et al. (2005) or Weng et al. (2003) for a more detailed description of the equations used to determine IWP.

This algorithm works because the upwelling radiation is scattered by millimeter-sized ice particles within the precipitation layer, with higher frequency radiation experiencing more scattering because it interacts more readily with smaller particles (Ferraro et al. 2005). Once IWP is determined, RR is calculated using:

$$\mathrm{RR} = r_0 + r_1 IWP + r_2 IWP^2 , \tag{3.16}$$

where the coefficients are dependent upon the rain type. The 183 GHz channels are used to classify the different rain types. Tb for 183±7 is “sensitive to the presence of ice particles at lower altitudes, whereas the measurements at 183±1 GHz primarily respond to deep convection where large ice particles are thrust substantially higher into the upper atmosphere” (Ferraro et al. 2005). From the different 183 GHz measurements, a convective index (CI) is determined:

$$\Delta_1 = TB_{183\pm1} - TB_{183\pm7} \tag{3.17}$$

$$\Delta_2 = TB_{183\pm3} - TB_{183\pm7} \tag{3.18}$$

$$\Delta_3 = TB_{183\pm1} - TB_{183\pm3} \tag{3.19}$$

where CI_1 is "an indicator of weak convection or stratiform rain," CI_2 is "an indicator of moderate convection," and CI_3 is "an indicator of strong convection" (Ferraro et al. 2005). The CI choices are determined by:

CI = 1 when $\Delta_2 > 0, \Delta_2 > \Delta_1, \Delta_2 > \Delta_3$

CI = 2 when $\Delta_1 > 0, \Delta_2 > 0, \Delta_3 > 0, \Delta_1 > \Delta_2, \Delta_1 > \Delta_3, \Delta_2 > \Delta_3$

CI = 3 when $\Delta_1 > 0, \Delta_2 > 0, \Delta_3 > 0, \Delta_1 > \Delta_2, \Delta_1 > \Delta_3, \Delta_2 < \Delta_3$.

The CI choice, in turn, establishes which coefficients should be used in the RR retrieval given by Eq. (3.16). See Table 3.1 below for these coefficient values:

TABLE 3.1: Convective index coefficients for RR determination. Source: Ferraro et al. (2005).

CI	$\mathbf{r_0}$	$\mathbf{r_1}$	$\mathbf{r_2}$
1	0.322	16.504	-3.342
2	0.322	16.504	-3.342
3	0.089	20.819	-2.912

Although AMSU-B RRs are considered to be less accurate than those from the TMI or SSM/I, as will be discussed further in the following section, the AMSU is more sensitive to light rain because of the availability of the 150 GHz channel (Weng et al. 2003). Rainfall rate retrievals are constantly evolving. For instance, Vila et al. (2007) describe a correction scheme for the AMSU-B RR retrieval that would give it the ability to sense rain that has little or no ice using cloud liquid water "as a proxy for retrieving rainfall."

3.2.4 CMORPH RR Product

The Climate Prediction Center (CPC) morphing method (CMORPH) global precipitation analyses are available every three hours beginning at 00 UTC. The spatial domain for these data is 0.25°×0.25° degree latitude/longitude resolution from 60° S to 60°

N. The 3-hourly CMORPH record is available from December 2002 to the present (CMORPH website). PMW rainfall estimates from the TMI, SSM/I, and AMSU-B instruments are mapped to the nearest grid point. If two estimates from the same sensor are mapped to the same grid point, the average rainfall is used. However, this generally only happens for TMI data since it is available at a higher resolution than the other two sources. When no rainfall estimates are mapped to a grid point, "an inverse distance squared weighting interpolation of the nearest rainfall estimates is performed to create a spatially complete field" (Joyce et al. 2004). When more than one sensor type has data matched to a grid point, TMI data are the first choice, SSM/I the second, and AMSU-B the third, if no information from the TMI or SSM/I is available. AMSU-B is the last choice because of its coarser spatial resolution and weaker rainfall estimation algorithm (i.e., it only considers scattering, not a combination of scattering and emission techniques as the other two algorithms do). Because the AMSU-B algorithm is so different from the TMI and SSM/I algorithms, a normalization procedure is used on the data, with SSM/I and TMI estimates as the standard (Joyce et al. 2004).

The CMORPH algorithm uses global infrared (IR) data from the Geostationary Operational Environmental Satellite-8 (GOES-8), GOES-10, Meteosat-5, Meteosat-7, and Geostationary Meteorological Satellite-5 (GMS-5) satellites to "detect cloud systems and determine their movement" (Joyce et al. 2004). This algorithm computes cloud system advection vectors (CSAVs) to propagate the PMW rainfall retrievals. To fill in the time-gaps for a grid box (e.g., data are available at 0330 and 0500 UTC, but not 0400 or 0430), the precipitation estimates are propagated both forward and backward in time using the IR CSAVs. Propagation of the precipitation features will only translate them positionally but will not represent their changing character. "Changes in the intensity and shape of the rainfall features are accomplished" by a morphing process, which is calculated using a time-weighted mean. For instance, considering the aforementioned time gap between 0330 and 0500, the missing values are calculated by Eqs. (3.20 and 3.21):

$$\text{Morphed Value }(0400) = 0.67{*}P_{\text{forward}}(0400) + 0.33{*}P_{\text{backward}}(0400) \tag{3.20}$$

$$\text{Morphed Value }(0430) = 0.33{*}P_{\text{forward}}(0430) + 0.67{*}P_{\text{backward}}(0430), \tag{3.21}$$

where "P_{forward} is the PMW precipitation estimate forward propagated from the initial analysis (0330 UTC), and P_{backward} is the PMW precipitation estimate backward propagated from the updated analysis (0500 UTC)" (Joyce et al. 2004). Using these propagation and morphing techniques, the CMORPH algorithm is able to generate a RR dataset with high spatial and temporal resolution and few missing points.

CMORPH "agrees well with radar for values below 0.5 mm day^{-1} but underestimates the higher" RR values, according to a study by Janowiak et al. (2005) over the US conducted during JJA 2003. In addition, they find that "CMORPH data reproduce previously documented behavior of the diurnal cycle in precipitation," which "gives credence to the utility of the CMORPH data and serves as a form of validation."

4. METHODOLOGY

4.1 Spatial and Temporal Domain

This study focuses on quasi-global TPW and RR values between February 11, 2006 and December 31, 2008. Although the CMORPH data are available from 2002, the bTPW data only became available in February 2006. Spatially, the bTPW data span from 71° S to 71° N while the CMORPH data span 60° S to 60° N, so the study domain covers all latitudes from 60° S to 60° N, for all longitudes. This study is quasi-global rather than global because data poleward of 60° were not considered. The bTPW data are available every 6 hours at roughly 00, 06, 12, and 18 UTC. Because of this, only CMORPH datasets from 00, 06, 12, and 18 UTC were used although they are available 3-hourly (CMORPH website). Since the bTPW data were not available at exactly 00, 06, 12, or 18 UTC, a dataset was considered to be 'time-matched' if its time stamp was within 2 hours of any of these times. Since the bTPW product is formed by compositing data from the previous 12 hour period, exact time-matching of the two datasets is impossible and choosing approximately coincident times is appropriate. In addition, TPW does not change drastically on a 2 hour timescale, so a slight delay should not impact the overall statistics. In some cases, datasets were missing for a given time period; for instance, no bTPW data are available between October 15, 2008 and October 27, 2008. In order to prevent the introduction of any diurnal bias into the study, the only days chosen for use in this study were those when all 4 datasets from both sources were available. All 1065 days of the 35 month study period did not fit these criteria, although 982 did, which represents approximately 92% of the temporal domain. In all, 3928 cases were used in this analysis.

Two different bTPW compositing methods are used in this analysis. In the days before and including June 6, 2006, the 'overlay' method is used, which adds only the most recent observations to the quasi-global image (i.e., the most recent observations are weighted '1' while previous observations in the 12 hour period are weighted '0'). This 'overlay' method results in more visible 'seams' due to the various satellite swaths comprising the image. For the days after and including June 8, 2006, the 'uniform' method is used, which assigns equal weights to all the observations gathered over the previous 12 hour period. The 'uniform' method results in a smoother global image of TPW.

The bTPW data are also available at a higher resolution than the CMORPH 0.25°×0.25° resolution, so the bTPW data were mapped to 0.25°×0.25° grid boxes. For this task, two options were available: choose one TPW value for each grid box or average together all available TPW values. Usually only one was available but, with the bTPW's higher resolution, sometimes more than one TPW value was present. TPW retrieval becomes confounded near coastlines, where one pixel may contain both land and ocean backgrounds. If, for instance, two TPW values were present in a coastal grid box, one value may be 0 mm (i.e., a missing value over a land surface) while the other is 40 mm (i.e., over ocean). The average, then, is 20 mm, which is inaccurate. Thus the decision was made to assign only one TPW value to each grid box in order to completely avoid these sorts of inaccuracies. When TPW values were compared for open ocean data, the 'choose one' and 'average all' TPW distributions were nearly identical, indicating that using only one TPW value when two are available does not drastically influence any results.

If enough rain is present in a satellite footprint, the sensor cannot make an accurate TPW measurement because raindrop emission overwhelms any water vapor signature, as will be described further in Sec. 5.4.1. However, even a non-simultaneous TPW value should be close to the value present during the rain event since a rainfall event does not deplete the TPW over an area. TPW variations occur on a longer timescale than RR variations so, even if TPW and RR measurements are not concurrent, it would be appropriate to compare a TPW observation to an observation of RR. A study of daily or other such short-timescale fluctuations would be inappropriate with these datasets since each map of TPW includes data collected over several hours, which is a long time relative to the temporal extent of a typical rainfall event and the diurnal cycle.

4.2 Rainfall Threshold Estimation

A rainfall threshold of 0.1 mm hr^{-1} was used as the boundary value between rain and no-rain scenarios. Thus the term 'raining' in this study means that a rain rate greater than or equal to 0.1 mm hr^{-1} has been detected. Trenberth (1998) also uses this value. The sensitivity of this threshold is examined in Secs. 5.2 and 5.4.4. In contrast, Ferraro (1997) asserts that the lowest detectable RR for SSM/I is 0.45 mm hr^{-1} over land and 0.2 mm hr^{-1} over ocean. However, rain rates can be detected over the ocean using an alternative RR algorithm that is incorporated when the atmospheric water vapor is sufficiently high but the scattering from ice particles is not sufficiently high to detect RR (Ferraro 1997). The AMS Glossary Website indicates that drizzle is defined as liquid precipitation from trace amounts to less than 1 mm hr^{-1} with a drop size less than 0.5 mm. Liquid precipitation is classified as rain when the RR is greater than 1 mm hr^{-1} or when the drop size exceeds 0.5 mm (AMS Glossary Website).

Using a given threshold value, the rainfall frequency estimations (in percent) used in Secs. 5.2, 5.3, and 5.4.2 were calculated by Eq. (4.1):

$$100 \times \frac{\#\,\text{data points with RR} \geq \text{threshold}}{\#\,\text{data points with RR} \geq 0.0\,\text{mm hr}^{-1}} \tag{4.1}$$

The use of a higher threshold would result in a lower rainfall frequency estimation.

4.3 Histogram Construction

For RR data, a bin size of 0.5 mm hr^{-1} was chosen. If the chosen RR bin size were too large, the details of the distribution would be lost. If the chosen bin size were too small, gaps would be present in the histogram where data was lacking for that range of rain rates. Choosing a varying bin size was considered since the occurrences of low RR events are much more frequent than higher RR events. However, this choice resulted in a nonphysical 'jump' from one bin to the next where the bin size varied. Thus the choice of a constant bin size of 0.5 mm hr^{-1} is used, with the exception that the first bin represents the absence of rain (i.e., $0 \leq \text{RR} < 0.1$ mm hr^{-1}) and the second bin is slightly less than 0.5 mm hr^{-1} wide (i.e., $0.1 \leq \text{RR} < 0.5$ mm hr^{-1}). Above 0.5 mm hr^{-1}, the bin size becomes a constant 0.5 mm hr^{-1}. For TPW data the choice of a 1 mm bin size was simpler, since TPW tends to be more symmetrically distributed.

For display purposes, the number of occurrences in each bin could be plotted as a function of the bottom, middle, or top of each bin. In this study, the bottom of the bin was chosen. For instance, in the RR distributions shown in Sec. 5.4.2, the proportion of rain events plotted for RR=3.0 mm hr^{-1} includes all instances of RR in the range $3.0 \leq \text{RR} < 3.5$ mm hr^{-1}. In addition, only RRs between 0.1 and 10 mm hr^{-1} are displayed because there are so few occurrences of rain at higher rain rates and the occurrences of no rainfall are so frequent that including them causes the details of the distribution to be unclear. The distributions are most clear when a sufficient number of events have occurred to visibly populate the histograms.

The RR distributions approximate an exponential decay, the equation for which is given by Eq. (4.2):

$$E(t) = E_o e^{-t/\tau} \tag{4.2}$$

The linear form of Eq. (4.2) is given by Eq. (4.3):

$$\ln E(t) = \ln E_o + \frac{-1}{\tau} t\,, \tag{4.3}$$

where $-1/\tau$ is the slope of the linear fit, 't' is the RR, ln E_o is the y-intercept, and ln E(t) is the natural logarithm of the proportion of total occurrences. Thus, a distribution is exponential if taking the natural logarithm of the ordinate values results in a linear trend. A relatively small time constant, τ, indicates that the decay is relatively rapid and corresponds to a steeper slope. As will be seen in Sec. 5.3, the distribution of RR is not strictly exponential, but comparing the slopes of exponential fits consistently depicts the differences between RR distributions.

4.4 Averaging

Daily, monthly, seasonal, and annual averages were calculated in such a way as to avoid any bias toward time periods containing more cases.

4.4.1 Total Precipitable Water

The TPW monthly mean is calculated at each grid point for each of the 35 months by:

$$\frac{\sum (\text{mm TPW})}{\#\,\text{data}} \tag{4.4}$$

These values are then converted to seasonal mean TPW estimations by weighting each monthly mean TPW by the proportion of time in that month relative to the time comprising that season, as shown in Eq. (4.5). For instance, the March 2006 mean TPW was weighted by 31÷276 (i.e., 31 days in March ÷ 276 days in the 3 MAM seasons).

$$\sum(\text{monthly mean TPW} \times \frac{\#\,\text{days}/\text{month}}{\#\,\text{days}/\text{season}}) \tag{4.5}$$

The annual mean TPW is then calculated by weighting the average seasonal TPW by the proportion of time of that season relative to the total 35 month period:

$$\sum(\text{seasonal mean TPW} \times \frac{\#\,\text{days}/\text{season}}{\#\,\text{days}/\text{35 month period}}) \tag{4.6}$$

4.4.2 Rainfall Rate

The monthly mean RR in mm month^{-1} was calculated at each location for each of the 35 months by:

$$\frac{\sum(\text{mm hr}^{-1}\ \text{RR})}{\#\,\text{data}} \times \frac{24\ \text{hours}}{\text{day}} \times \frac{\#\,\text{days}}{\text{month}} \tag{4.7}$$

From these values, the seasonal monthly mean RR in mm month^{-1} was calculated by weighting each monthly mean RR by the proportion of time of that month relative to the season, as in Eq. (4.5).

The annual mean RR in mm day^{-1} is calculated in a similar way. First the monthly mean RR in mm month^{-1} was converted to the mean mm day^{-1} for that month by dividing by the number of days in that month:

$$\frac{\#\,\text{mm}/\text{month}}{\#\,\text{days}/\text{month}} \tag{4.8}$$

Then each of these daily mean RR values was weighted by:

$$\frac{\#\,\text{days}\big/\text{month}}{\#\,\text{days}\big/35\ \text{month period}} \tag{4.9}$$

and summed to estimate the mean daily RR at each grid point.

4.4.3 Area-Weighting

Any mean values calculated for values at varying latitudes, such as those described in Secs. 5.1, 5.2, and 5.3, were computed by first finding the zonal mean at each latitude. Then an area-weighted mean is computed, which is necessary since the grid boxes at the equator are physically larger than grid boxes at higher latitudes. This area-weighted mean takes the form:

$$\frac{\sum_i \text{value}_i\, w_i}{\sum_i w_i} \tag{4.10}$$

where each weight w_i is the cosine of the center latitude. For instance, in the grid box from 60° to 59.75°, the center latitude is 59.875°.

5. OBSERVED TPW AND RR RESULTS

5.1 Total Precipitable Water Climatology

The global TPW distribution shown in Fig. 5.1 displays a similar pattern to Trenberth's (1998) estimates in Fig. 2.1. The west Pacific warm pool has annual mean TPW values between 50 and 60 mm, TPW values between 40 and 50 mm encircle the globe at the equator, the South Pacific Convergence Zone (SPCZ) displays relatively high values, and TPW generally decreases poleward of the equator, with the lowest values in the highest latitudes. In addition, the oceanic desert regions are evident from the relatively low TPW values off the west coasts of North America, South America, and northern and southern Africa. While the bTPW dataset's only over-land values are over the United States, the same

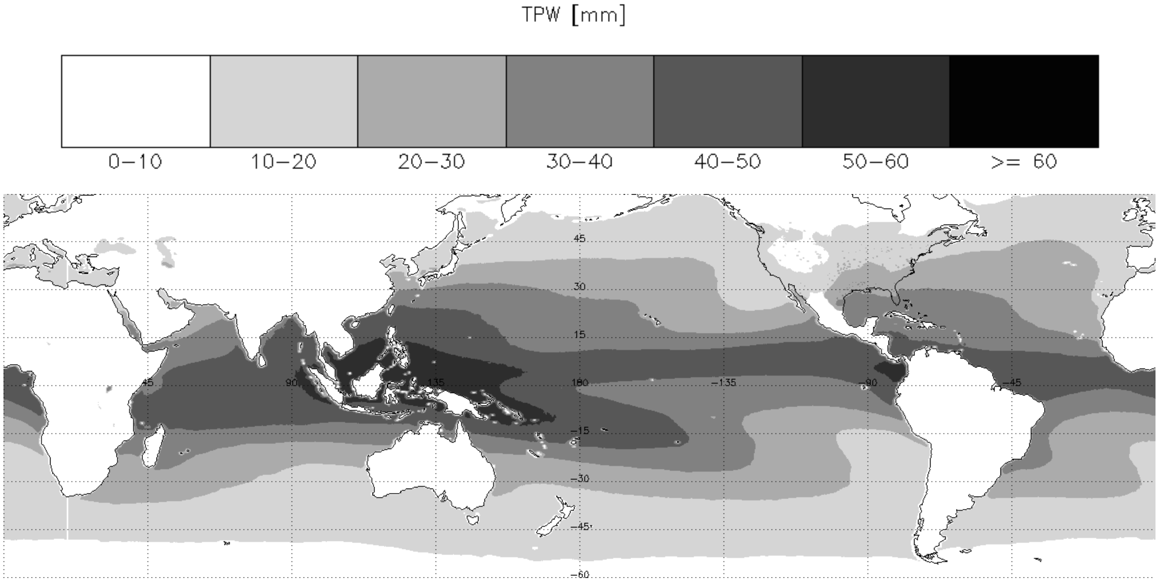

FIG. 5.1. Annual mean TPW in mm. No annual mean TPW values exceed 60 mm. These 10 mm contours match the contours chosen for Figs. 2.1 and 2.3.

patterns are present there as in Fig. 2.1: the western half of the country tends to have lower TPW than the eastern half, and the southeastern US has the highest TPW values. The annual mean zonal profile of TPW shown on the right of Fig. 2.1 corresponds well with the distribution displayed in Fig. 5.2. In both estimates, the global distribution of TPW peaks slightly north of the equator, around 7° N, at 45 mm, which is consistent with the ITCZ's annual mean location north of the equator. At 20° N and S, the zonal mean TPW is around 30 mm in both Figs. 5.2 and 2.1. The quasi-global mean TPW is 24.94 mm. Again, this is the mean for the domain containing ocean regions between 60° N and 60° S and the continental United States (CONUS). This value is slightly higher than the 24.52 mm global mean TPW calculated by Sudradjat et al. (2005). This slight increase is expected because this study does not include data from areas poleward of 60° and does not include data from land areas other than CONUS. The inclusion of these additional areas would tend to lower the global mean.

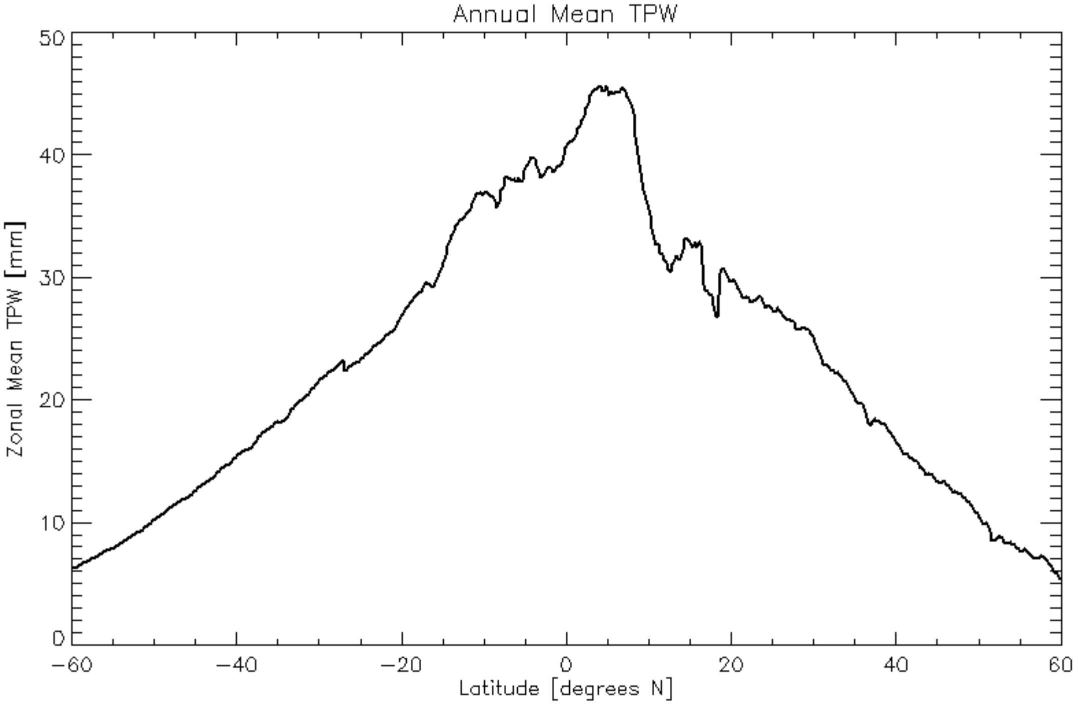

FIG. 5.2. Zonal profile of annual mean TPW over the ocean.

The seasonal mean TPW plots shown in Fig. 5.3 correspond to similar plots constructed by Ferraro et al. (1996) in Fig. 2.3. The plots are roughly similar—the west Pacific warm pool contains the highest TPW year-round, with the ITCZ having its highest TPW values in the March through November time frame. The TPW minima are in the northern polar regions during DJF and in the southern polar regions during JJA (i.e., during each hemisphere's winter season), following the movement of the solar irradiation maximum. The SPCZ extends its farthest eastward in DJF and retreats its farthest westward during JJA. In addition, the seasonal differences in the west Pacific warm pool are similar in both depictions: TPW is fairly latitudinally stratified from September through May, while during the NH summer monsoon months, TPW increases significantly around southeast Asia and India.

One difference between the two studies' results is that an occurrence of the double ITCZ is present in MAM of Fig. 5.3 but is absent in Ferraro et al.'s (1996) eight-year study (Fig. 2.3). As Quantz (2009) asserts, the double ITCZ is part of the early boreal springtime climatology of the eastern Pacific. Although the MAM plot calculated by Ferraro et al. (1996) does not display this southern band of the ITCZ, it does show there to be relatively high TPW values in the eastern Pacific just south of the equator even though a region of relatively low TPW at the equator is not present to differentiate between two distinct bands of the ITCZ. Another difference is that the zonal band of high TPW at the equator is consistently greater than 50 mm between March and November in Fig. 2.3, but the same region in Fig. 5.3 shows TPW to be between 40 and 50 mm (a result supported by the fact that the zonal TPW maximum is about 45 mm, as seen in Fig. 5.2).

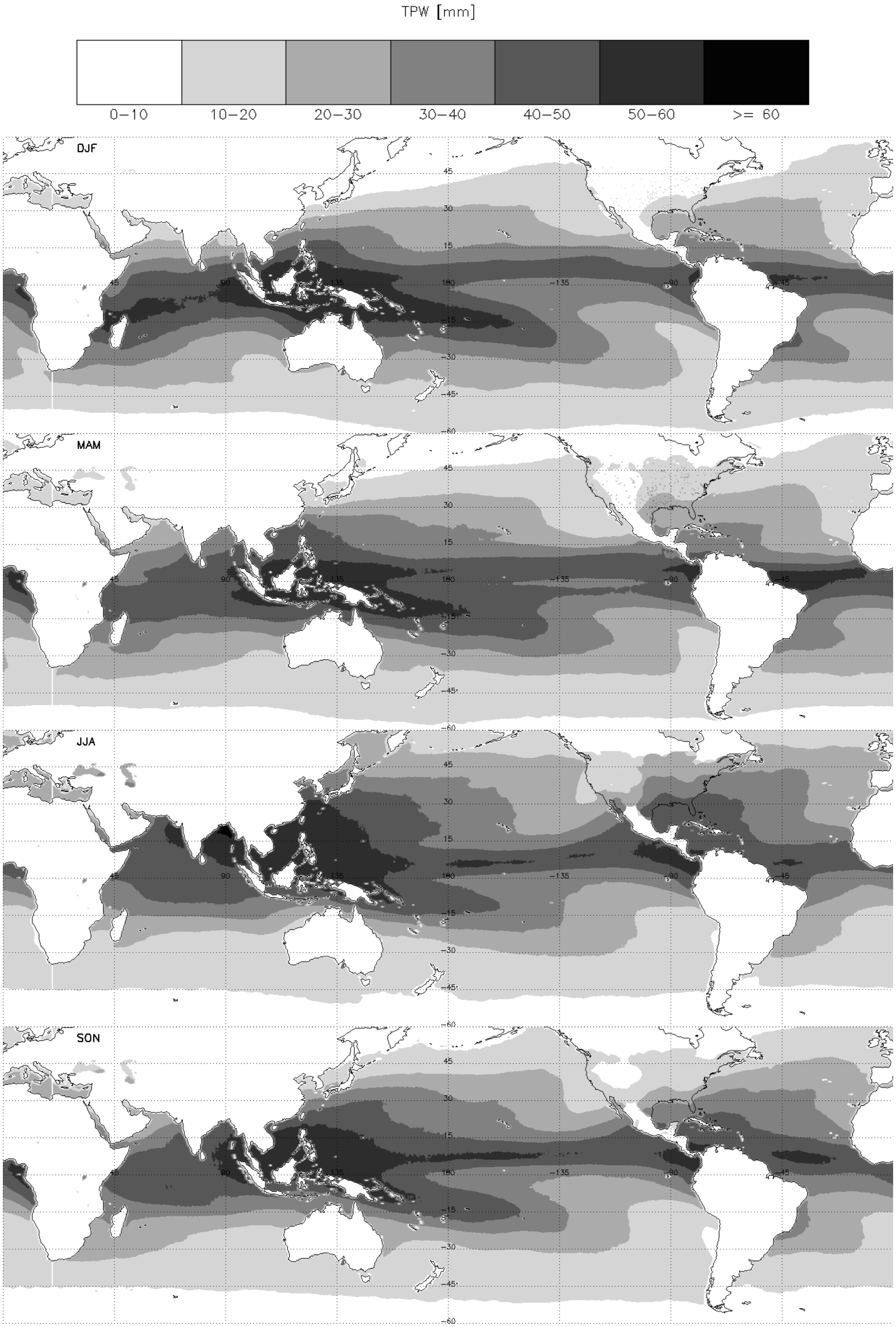

FIG. 5.3. Seasonal mean TPW in mm for DJF, MAM, JJA, and SON. The color scale was constructed to compare directly with Fig. 2.3. No seasonal mean values exceed 60 mm.

5.2 Rainfall Rate Climatology

The global mean distribution of RR shown in Fig. 5.4 displays similarities to the distribution constructed by Legates and Willmott (1990) (Fig. 2.4). For instance, elevated RRs are present over the ocean in the ITCZ, SPCZ, west Pacific warm pool, and midlatitude storm tracks and over land in the Amazon Basin and the African savannah and rainforest. A marked difference is present in the oceanic desert regions, which are quite extensive in Fig. 5.4; the region off the west coast of South America extends nearly to 180° W. In Fig. 2.4, however, the same region of $0 \leq RR < 0.5$ mm day^{-1} does not extend west of 90° W. This difference is most likely due to the fact that Legates and Willmott (1990) used data from rain gauges, which can detect light rainfall, whereas the sensors used in the present study are not as sensitive to the light stratiform rainfall characteristic of these oceanic desert regions. Another difference is that the southern band of the ITCZ is present in the eastern Pacific in the Fig. 5.4 where it is absent in the annual mean values from previous studies (Figs. 2.4 and 2.5).

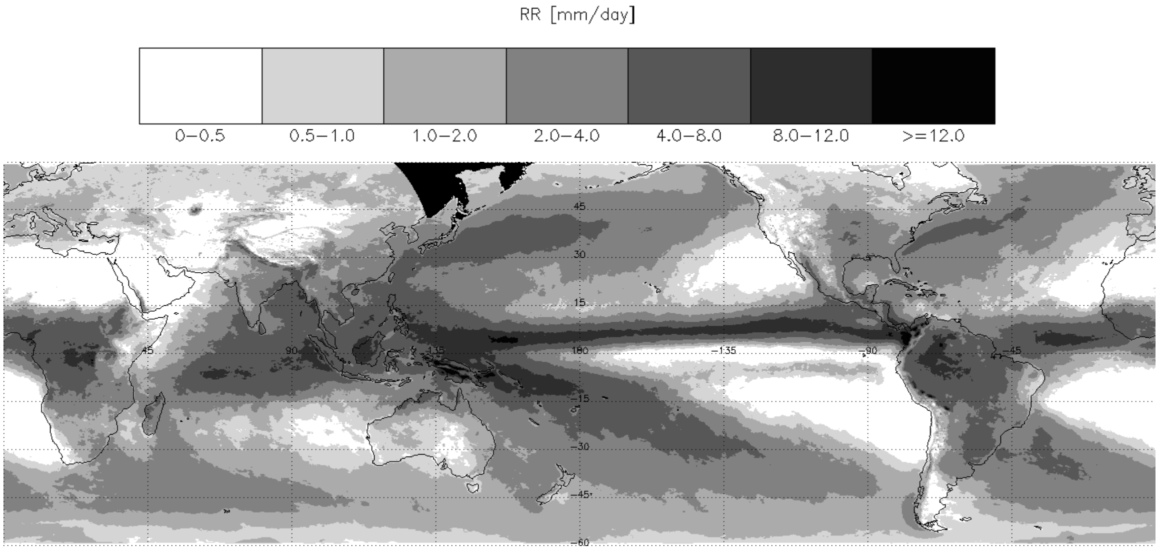

FIG. 5.4. Annual mean daily RR in mm day^{-1}. The color scale was constructed to compare with Fig. 2.4.

The global mean RR measured in this study is 2.63 mm day^{-1}, which is close to the values shown in Table 2.1. The global ocean and land RRs shown in Table 5.1 follow the same pattern as those shown in Table 2.1; that is, the oceanic RR is the highest and RR over land is the lowest. The global mean land RR in this study of 2.57 mm day^{-1} appears to overestimate older studies' values of around 2 mm day^{-1}. The global mean oceanic RR in this study of 2.68 mm day^{-1} underestimates previous studies' values of around 3 mm day^{-1}.

TABLE 5.1. Annual mean daily RR for different surface types and averaging techniques.

Surface Type	RR [mm day^{-1}]
Ocean	2.68
Land	2.57
All Surfaces	2.63

The zonal distribution of rainfall in Fig. 5.5 is similar to the zonal distribution of TPW in Fig. 5.2, with the exception of significant differences between land- and ocean-falling rain. As can be seen in Fig. 5.5b, the annual mean distribution of rainfall over land is fairly symmetric, with its peak just south of the equator, a similar finding as in Fig. 2.6a. As seen in Fig. 5.4, the majority of the over-land rain occurs in the Amazon Basin and in the sub-Saharan African savannas and rainforests, which explains the slightly southern peak in Fig. 5.5b. In Fig. 5.5a, however, there is a double peak in the tropics, with the highest of the two just north of the equator, around 7° N, which corresponds to the peak in the zonal TPW displayed in Fig. 5.2 and is likely due to the preferred location of the ITCZ north of the equator. The southern peak is likely due to the large amount of rainfall that occurs in the western Pacific. The southern peak is likely lower than the northern peak because the oceanic deserts in the eastern oceans are much stronger in the SH than in the NH. This double peak in tropical oceanic rainfall is present in Fig. 2.6b, which also shows a stronger northern peak. As in the plots by Ferraro et al. (1996) shown in Fig. 2.6, the midlatitude secondary peaks in oceanic rainfall are present, with slightly more midlatitude rainfall occurring in the NH. The CMORPH data differ from their data in that the CMORPH annual estimates are higher. For instance, the equatorial low from Fig. 2.6b shows less than 1000 mm yr^{-1} of rainfall, while this study estimates more than 1000 mm yr^{-1} of rainfall in the

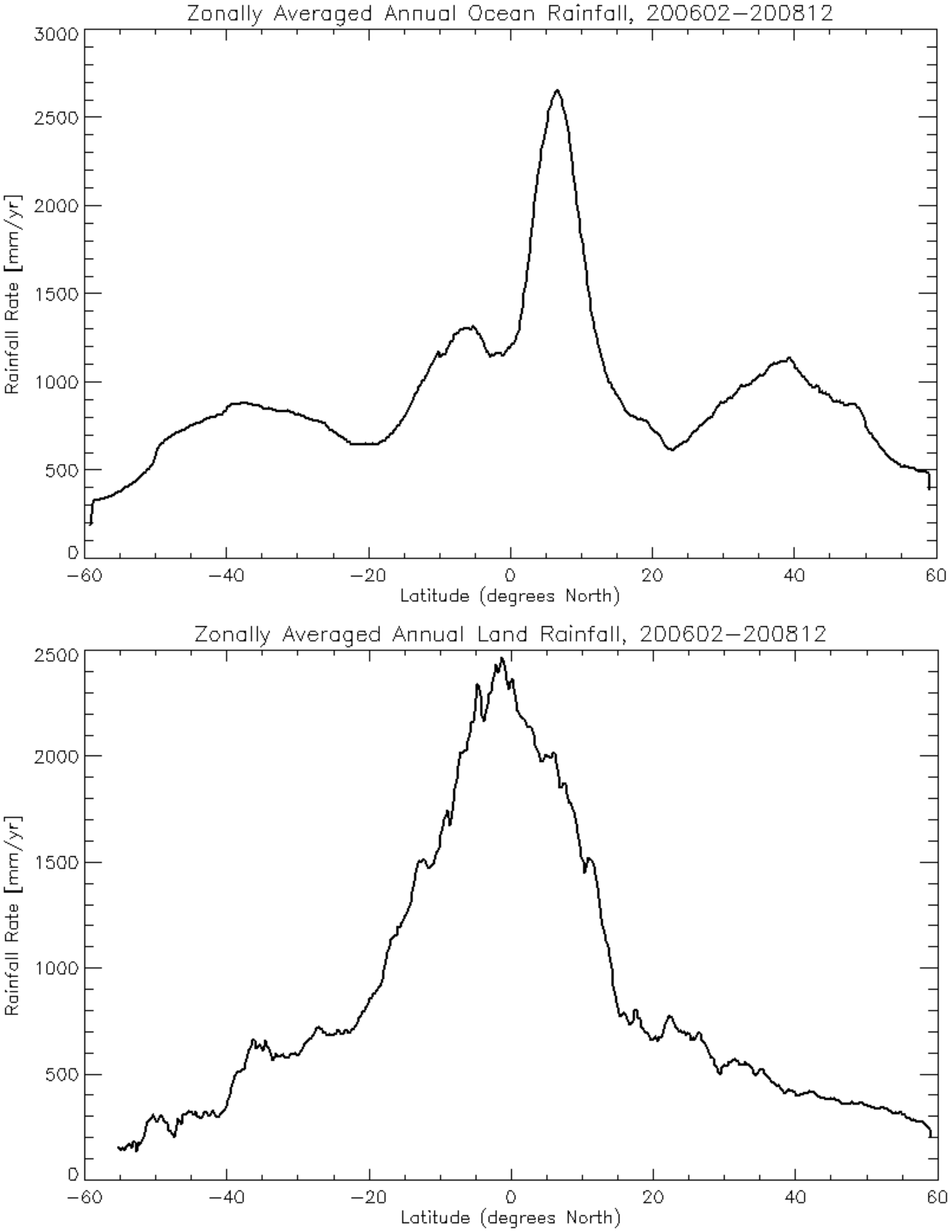

FIG. 5.5. Zonal mean annual rainfall in mm yr^{-1} over (a) ocean and (b) land.

same latitude zone. A similar trend is found at all latitudes. Over land, in both Figs. 2.6a and 5.5b, there is a steep decline in annual rainfall poleward of the equator. There is a significant difference between hemispheres: in the NH, this steep decline ends around 15° N while in the SH it ends around 20° S.

Rainfall frequency was also calculated to estimate its variability around the 10% global average (Trenberth 1998). As is evident in Fig. 5.6 and Table 5.2, rainfall frequency is

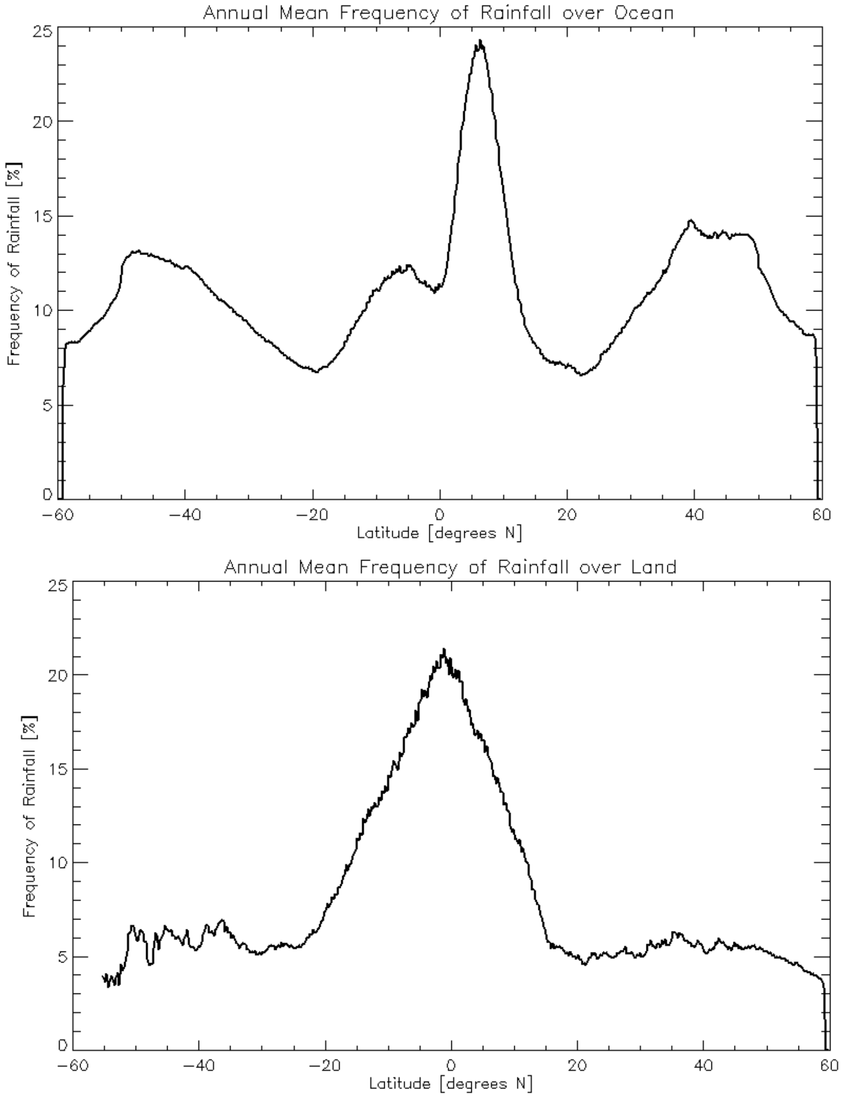

FIG. 5.6. Zonally averaged rainfall frequency over (a) ocean and (b) land.

TABLE 5.2. Mean rainfall frequency separated by surface type and latitude zone.

Latitude Zone	**Ocean Frequency [%]**	**Land Frequency [%]**
60-45° N	10.99	4.68
45-30° N	12.72	5.65
30-15° N	7.56	5.15
15-0° N	16.48	13.91
0-15° S	11.02	16.41
15-30° S	7.63	6.90
30-45° S	11.32	5.91
45-60° S	10.23	5.19

quite variable and the zonal distribution of rainfall frequency is analogous to the zonal distribution of rainfall (Fig. 5.5). There is a double peak of rainfall in the tropics, with rain falling more frequently around 7° N than around 7° S. There are secondary maxima in the midlatitudes. Over land, the distribution is more symmetric, with the peak occurring just south of the equator, around 2° S. The tropical and midlatitude oceans receive rain more frequently than the subtropics. Over land, the tropics receive rain the most frequently by far, with the midlatitudes experiencing rainfall the least frequently. When Fig. 5.6 is compared to Fig. 2.8, which displays the rainfall frequency for April 2005, similar trends are present. Although the frequencies calculated in Fig. 2.8 theoretically should be higher, since those frequencies were determined by $(RR>0)\div(RR\geq0)$ and not $(RR\geq0.1)\div(RR\geq0)$, they are not. For instance, the over-land peak frequency at the equator is between 14 and 18% in Fig. 2.8, as opposed to 22% as found in Fig. 5.6b.

Because of the similarities between the zonal distributions of rainfall (Fig. 5.5) and rainfall frequency (Fig. 5.6), the general distribution of rain must be relatively consistent throughout the domain, as will be further explored in Sec. 5.4.3. For instance, if most of the rain in the tropics were to fall in heavy rain events while midlatitude rainfall occurred for more variable RRs, the rainfall frequency would be low in the tropics and high in the midlatitudes. Since this is not the case, no particular latitude can be identified at which most of the rain comes from high RR events.

The zonally-averaged frequencies of heavy rainfall (i.e., RR thresholds of 5 and 10 mm hr^{-1}) were also calculated, as shown in Figs. 5.7 and 5.8. As expected, the frequency of

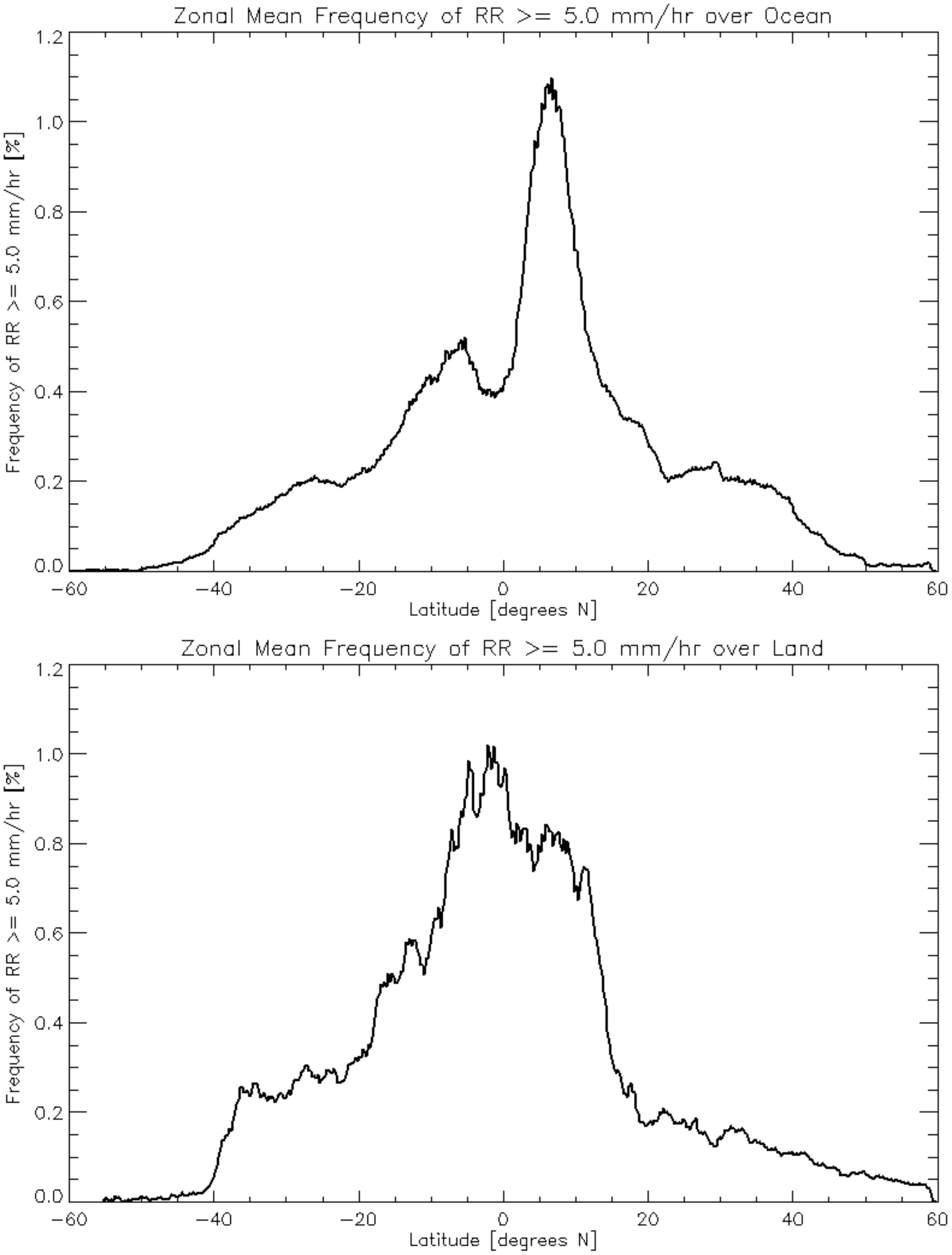

FIG. 5.7. Zonally averaged frequency of RR≥5.0 mm hr^{-1} over (a) ocean and (b) land.

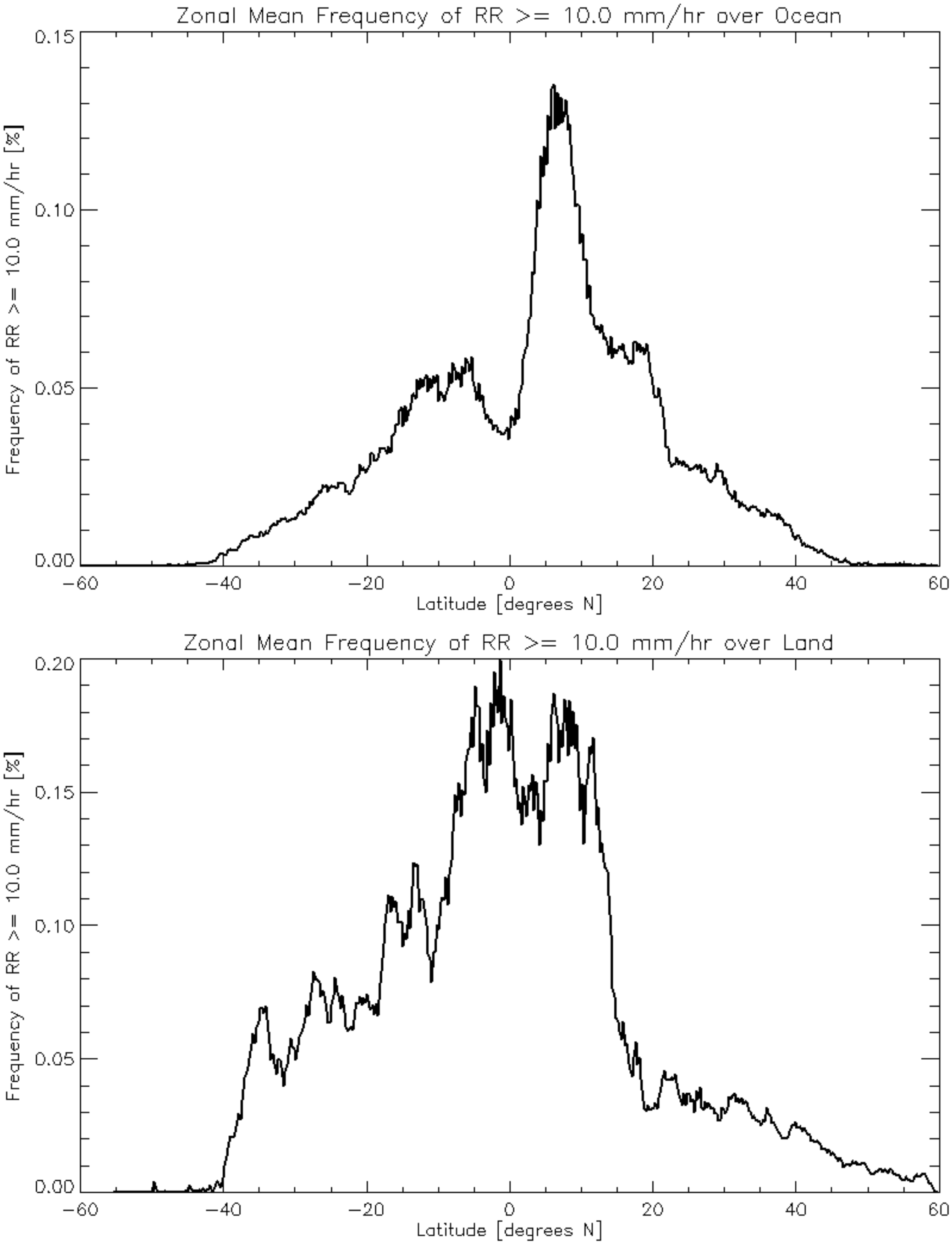

FIG. 5.8. Zonally averaged frequency of RR≥10.0 mm hr^{-1} over (a) ocean and (b) land.

RR≥10 mm hr^{-1} is less than the frequency of RR≥5 mm hr^{-1} at each respective latitude. These higher RRs are rare poleward of about 40° over both ocean and land, with the exception of the northern midlatitude land areas. This result is likely due to the fact that there is much more land area north of 40° N than south of 40° S, which means there are more data to populate the land histogram north of 40° N. These zonal profiles display similar trends to those seen in Fig. 5.6. However, Fig. 5.7b shows an approximately symmetric plot with a single peak just south of the equator, whereas Fig. 5.8b indicates the presence of a double peak, which is typically characteristic of oceanic, not land, rainfall.

Table 5.3 displays the mean rainfall frequency at different RR thresholds over the ocean and over land. Oceanic rainfall occurs more frequently than rainfall over land, which is a similar finding as presented in Sec. 2.3.2. However, Table 5.3 shows that heavier RRs are more frequent over land surfaces than over the ocean. One reason for this discrepancy between rainfall and heavy rainfall trends may be that surface heating and orographic effects may contribute to more intense rainfall over land areas when compared with ocean areas.

TABLE 5.3. Rainfall frequency according to surface type and RR threshold.

		RR Threshold	
Surface Type	**0.1 mm hr^{-1}**	**5.0 mm hr^{-1}**	**10.0 mm hr^{-1}**
Ocean	11.04 %	0.27 %	0.03 %
Land	8.58 %	0.34 %	0.07 %

The seasonal monthly mean rainfall totals shown in Fig. 5.9 are comparable to the analogous plots by Ferraro et al. (1996) shown in Fig. 2.10. For instance, rainfall amounts exceed 400 mm month^{-1} around the Bay of Bengal and in the eastern tropical Pacific during JJA. A southern band of the ITCZ is present during MAM, with values between 100 and 200 mm month^{-1}. In addition, the heaviest RRs in the SPCZ reach their farthest eastward during DJF. Most of the land rainfall during DJF occurs over the SH land areas while most of the land rainfall during JJA occurs over the NH land areas (i.e., each hemisphere's summer season). Comparing these plots with the seasonal mean TPW distribution displayed in Fig. 5.3 reveals that the most rainfall tends to occur in the area with the highest TPW: the ITCZ, SPCZ, the west Pacific warm pool, and the midlatitude storm tracks. For instance, TPW is

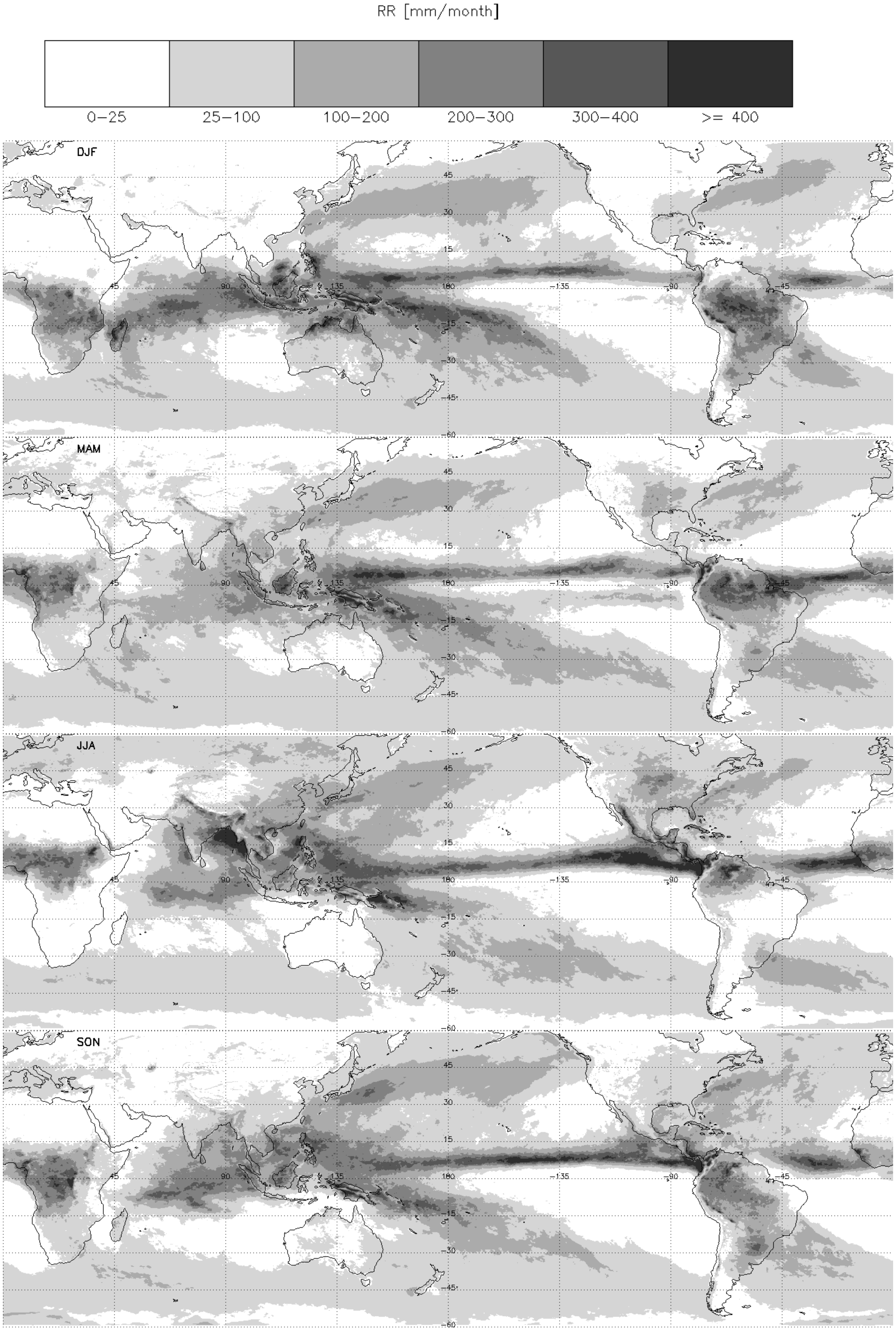

FIG. 5.9. Seasonal mean rainfall in mm month^{-1} for DJF, MAM, JJA, and SON. The color scale was constructed to facilitate comparison with the results shown in Fig. 2.10.

relatively low in the Bay of Bengal during DJF and high during JJA; similarly, monthly mean rainfall is relatively low in the same area during DJF and high during JJA. In the same way, areas characterized by low TPW, such as oceanic desert regions, receive relatively little rainfall. A notable exception exists in the midlatitude storm tracks, which are associated with relatively high rainfall amounts but not with high TPW values. In these areas, regional dynamics are a more significant factor in the creation of rainfall, as described in Sec. 2.4. Some orographic influences on the occurrence of rain are also evident in Fig. 5.9. In particular, the relatively high rainfall in the Himalayan and Andes Mountains is present in all seasons.

Figs. 5.10-12 display the seasonal mean rainfall frequency distributions using three different rain/no-rain thresholds: 0.1, 0.5, and 1.0 mm hr^{-1}, respectively. When these rainfall frequency maps are compared to the Ferraro et al. (1996) seasonal rainfall frequencies shown in Fig. 2.7, a rain/no-rain threshold of 0.5 mm hr^{-1} appears to best replicate the results (i.e., Fig. 5.11). For instance, Fig. 5.10 shows that using the 0.1 mm hr^{-1} threshold estimates rainfall frequency to be greater than 20% throughout the ITCZ, west Pacific warm pool, midlatitude storm tracks, Amazon Basin, and sub-Saharan Africa. In contrast, Ferraro et al. (1996) observe that these very high rainfall frequencies occur, but the area of occurrence is limited and seasonally dependent. For instance, in Fig. 2.7, rain falls more than 20% of the time in the eastern ITCZ only during JJA; Fig. 5.10 shows the same observation. However, when the zonal rainfall frequencies are considered, as shown in Table 5.4, the 0.5 mm hr^{-1} threshold results in quasi-global mean rainfall frequencies less than 5%, whereas the 0.1 mm hr^{-1} threshold results in quasi-global mean rainfall frequencies around 10%, which is closer to the conclusion from a previous study (Trenberth 1998). When rainfall frequencies using a threshold of 1.0 mm hr^{-1} are estimated (Fig. 5.12), the difference between quasi-global

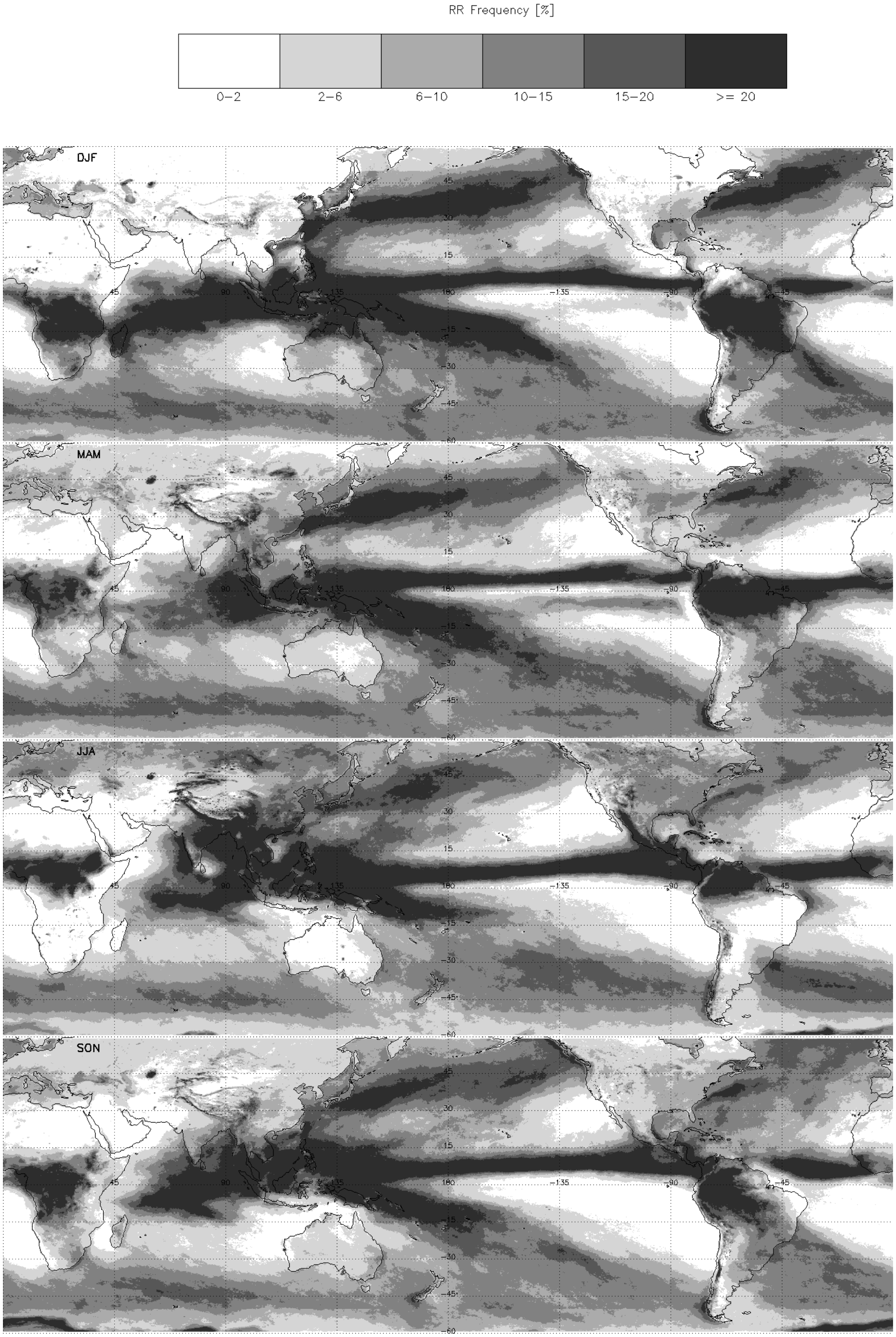

FIG. 5.10. Seasonal mean rainfall frequency for DJF, MAM, JJA, and SON using a rain/no-rain threshold of 0.1 mm hr^{-1}. The color scale was chosen for direct comparison with Fig. 2.7.

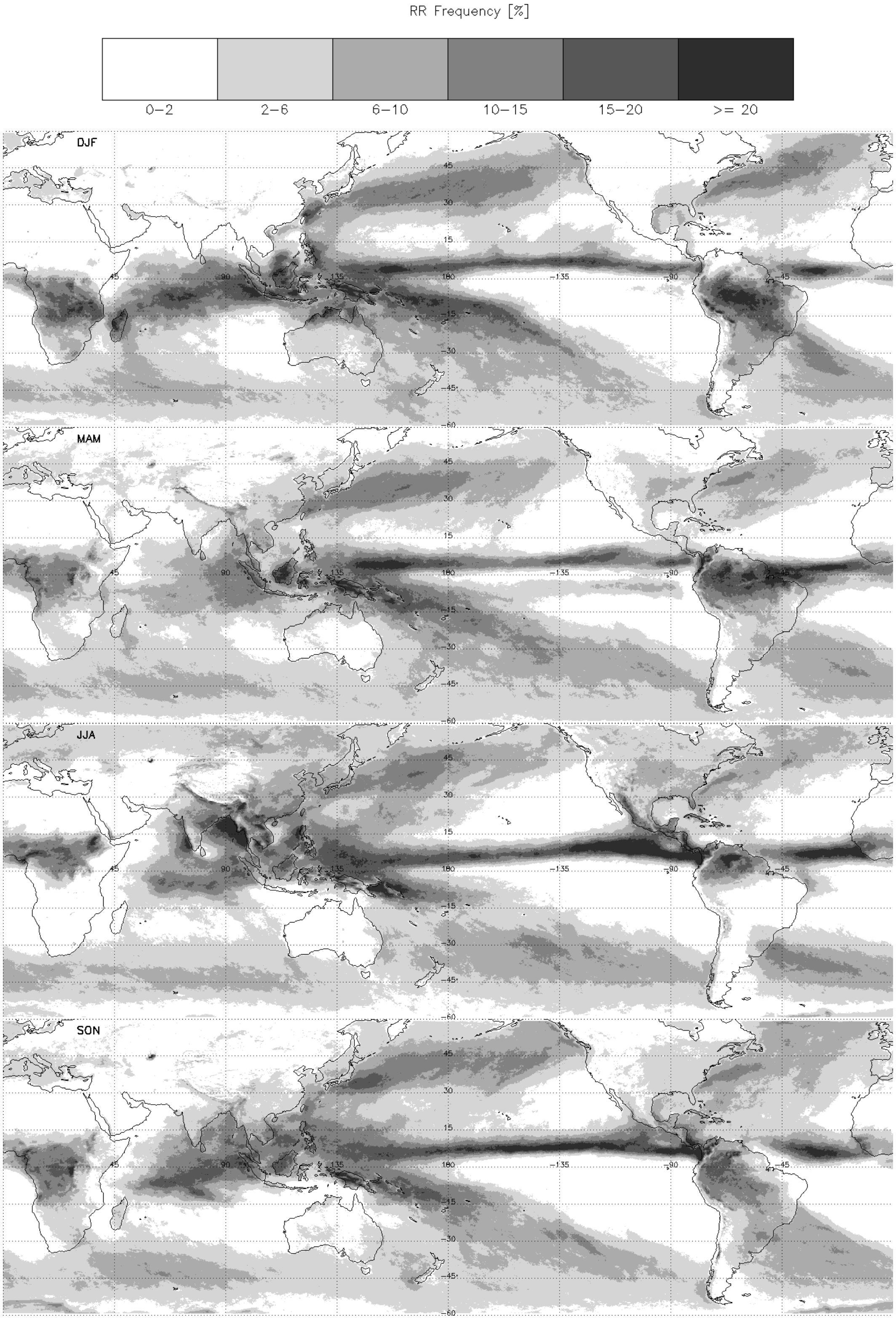

FIG. 5.11. Seasonal mean rainfall frequency for DJF, MAM, JJA, and SON using a rain/no-rain threshold of 0.5 mm hr^{-1}. The color scale was chosen for direct comparison with Fig. 2.7.

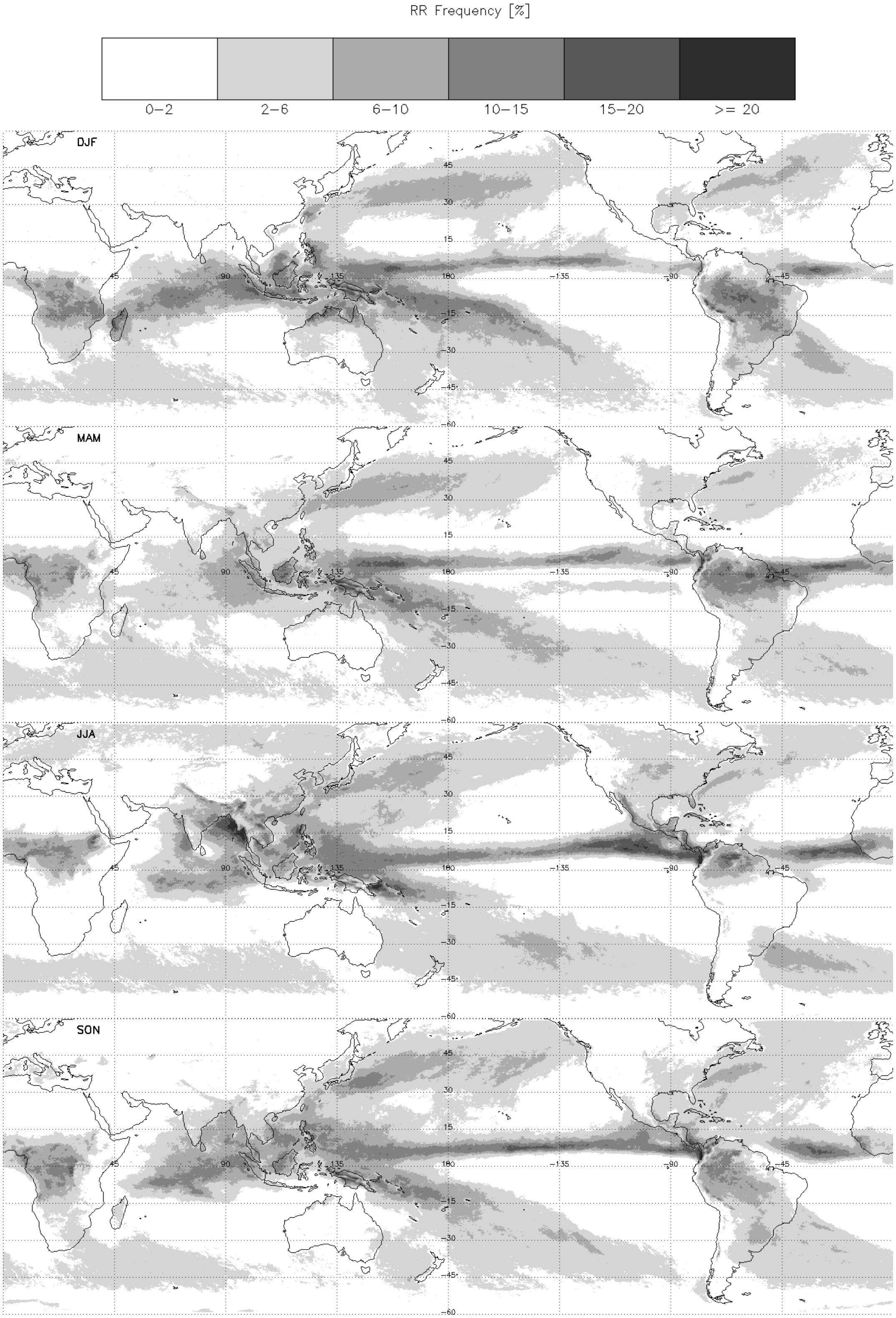

FIG. 5.12. Seasonal mean rainfall frequency for DJF, MAM, JJA, and SON using a rain/no-rain threshold of 1.0 mm hr^{-1}. The color scale was chosen for direct comparison with Fig. 2.7.

TABLE 5.4. Global mean rainfall frequency, separated according to season and RR threshold.

	RR Threshold		
Season	**0.1 mm hr^{-1}**	**0.5 mm hr^{-1}**	**1.0 mm hr^{-1}**
DJF	10.31 %	4.88 %	2.76 %
MAM	10.30 %	4.79 %	2.76 %
JJA	10.17 %	5.00 %	2.92 %
SON	10.09 %	4.95 %	2.88 %

rainfall frequencies as compared to previous studies is vastly underestimated, both in the quasi-global distribution (Fig. 5.12) and the domain means (Table 5.4). Thus, the use of a rain/no-rain threshold in the range of 0.1 to 0.5 mm hr^{-1} is more appropriate.

5.3 Rainfall Behavior in TPW Regimes

The quasi-global rainfall rate distributions change for different TPW regimes, as can be seen in Fig. 5.13. In Fig. 5.13a, constructed for rainfall occurring coincident with TPW between 0 and 15 mm, there are few occurrences of RR $\geq$ 2 mm hr^{-1}. The proportion of these higher RRs is greater in Fig. 5.13e, for TPW values between 60 and 75 mm. It is important to note that spatial and temporal TPW dependencies have not been accounted for in these plots. For instance, few high TPW values occur in the high latitudes and few low TPW values occur in the low latitudes, as is evident from Fig. 5.3. As described in Sec. 2.4, atmospheric dynamics are an important factor when considering the occurrence of rainfall and TPW. So although more heavy rainfall events occur in the presence of high TPW values, the regions that experience these conditions are in areas of moisture convergence and ascending water vapor, conditions that facilitate the production of rainfall. Similarly, areas experiencing low TPW values and relatively few high RR events are in regions of moisture divergence and atmospheric subsidence, conditions that tend to hinder the production of rainfall. Thus high TPW is not the sole factor in the production of heavy rainfall.

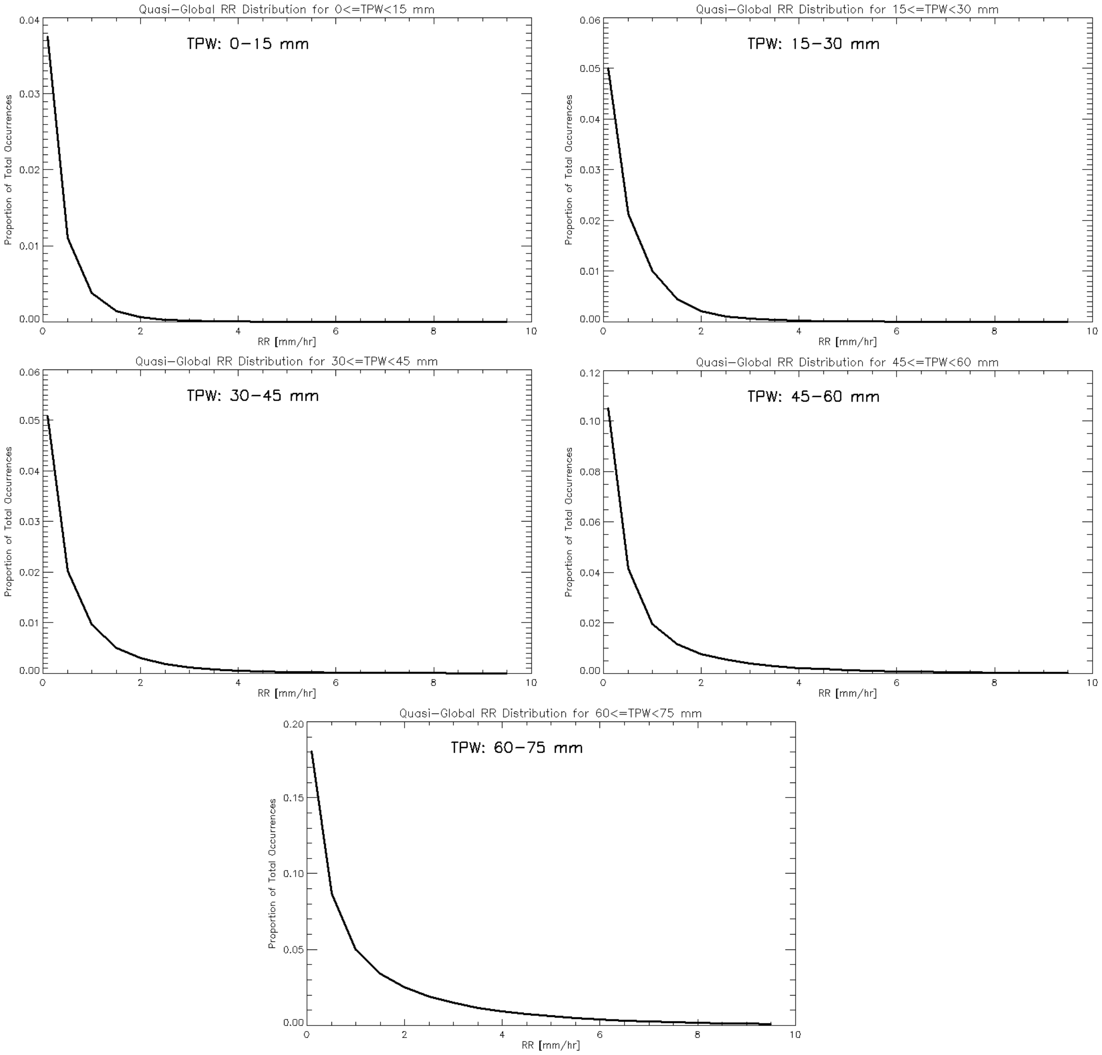

FIG. 5.13. Quasi-global RR distributions according to TPW ranges (a) 0-15 mm, (b) 15-30 mm, (c) 30-45 mm, (d) 45-60 mm, and (e) 60-75 mm. All 35 months of data were used to calculate these distributions. The y-axis displays the proportion of total occurrences; the scale varies from plot to plot.

An exponential fit was applied to each distribution using the method described in Sec. 4.3. These exponentially-fit RR distributions can be seen in Fig. 5.14 and the slope of each exponential fit can be seen in Table 5.5. As is evident from Table 5.5, the more negative slopes (i.e., faster rates of exponential decay) are associated with lower TPW regimes. This result means that there is a higher proportion of heavy rainfall events when the atmosphere contains more water vapor. The exponentially-fit RR distributions in Fig. 5.14 are not strictly linear, which indicates that the global mean RR distributions for each TPW range are not

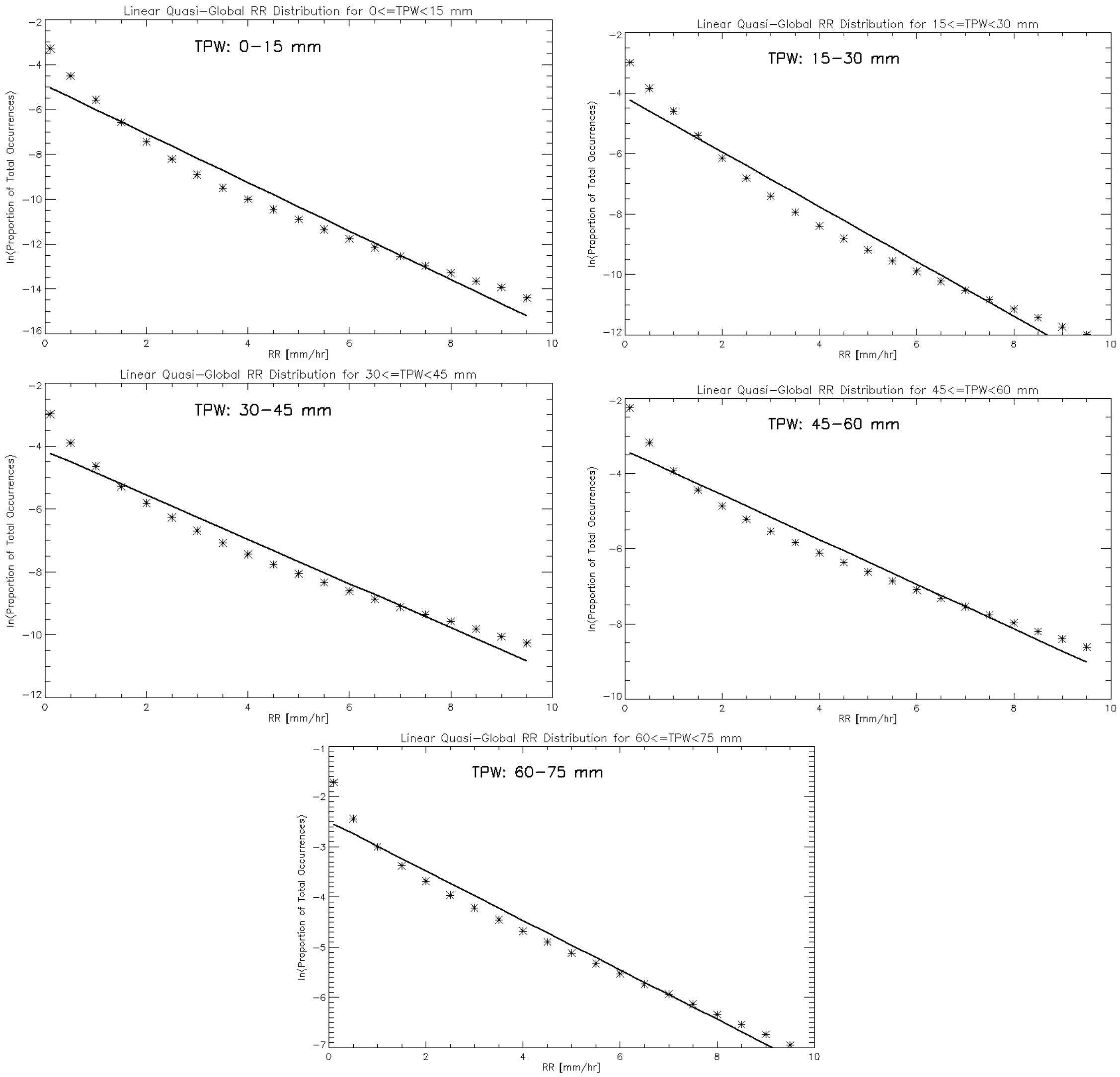

FIG. 5.14. Quasi-global linear RR distributions according to TPW ranges (a) 0-15 mm, (b) 15-30 mm, (c) 30-45 mm, (d) 45-60 mm, and (e) 60-75 mm. All 35 months of data were used to calculate these distributions. The y-axis displays the natural logarithm of the proportion of total occurrences; the scale varies from plot to plot.

TABLE 5.5. Slopes of exponential fits for different TPW regimes.

TPW Range	Slope of Exponential Fit
0-15 mm	-1.01
15-30 mm	-0.90
30-45 mm	-0.70
45-60 mm	-0.59
60-75 mm	-0.49

strictly exponential. However, fitting an exponential decay equation to the RR distribution results in a slope that describes the general behavior of the rainfall as compared with the slopes of other RR distributions.

These quasi-global RR distributions also demonstrate the probabilities of rainfall at different RR thresholds, as shown in Table 5.6. The driest regime experiences the lowest probability of rainfall, while the moistest regime experiences the highest probability of rainfall, at 45.9%. That is, on average, any area with TPW between 60 and 75 mm has a 45.9% chance of rainfall. These TPW values are relatively infrequent since the annual mean TPW (Fig. 5.1) does not yield any values over 60 mm. Heavier RRs are much less probable; on average, a RR ≥ 5 mm hr^{-1} will occur less than 3% of the time even for high TPW values. In addition, these probabilities are not absolute due to the spatial and temporal dependence of TPW described above. That is, local dynamics are a key factor in the determination of rainfall.

TABLE 5.6. Global mean rainfall frequency for different RR thresholds and TPW regimes.

	RR Threshold			
TPW Range	**0.1 mm hr^{-1}**	**1.0 mm hr^{-1}**	**5.0 mm hr^{-1}**	**10.0 mm hr^{-1}**
0-15 mm	2.338 %	0.298 %	0.003 %	0.0001 %
15-30 mm	7.640 %	1.536 %	0.026 %	0.002 %
30-45 mm	16.591 %	4.319 %	0.180 %	0.018 %
45-60 mm	29.885 %	9.371 %	0.767 %	0.088 %
60-75 mm	45.894 %	18.839 %	2.694 %	0.340 %

Figure 5.15 shows the zonal distributions of the slopes of the exponentially-fit RR distributions in the different TPW regimes. It is apparent in Fig. 5.15a and 5.15b that the low latitudes rarely experience low TPW values, since the slopes in this region are so inconsistent. The reason for the highly variable slopes in this region is likely that there are few occurrences of rain (because there are few occurrences of such low TPW values) to

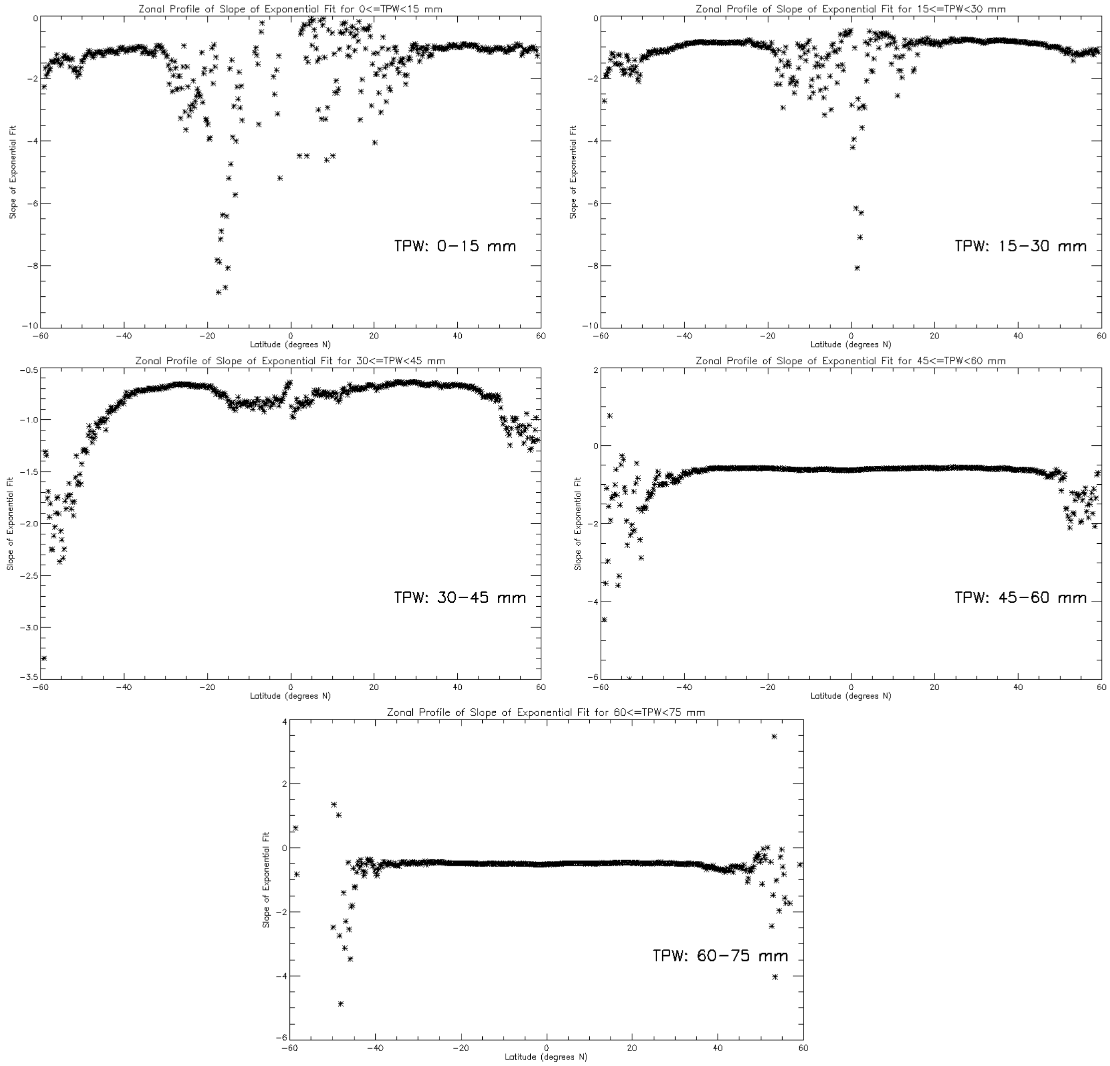

FIG. 5.15. Quasi-global zonal mean slope of exponential fit according to TPW ranges (a) 0-15 mm, (b) 15-30 mm, (c) 30-45 mm, (d) 45-60 mm, and (e) 60-75 mm. All 35 months of data were used to calculate these distributions. The y-axis scale varies from plot to plot.

sufficiently populate the RR distributions at those latitudes. A similar pattern is present for the higher TPW regimes at the higher latitudes (Fig. 5.15d and e); those areas rarely experience such high TPW values. Not considering these highly variable areas, Fig. 5.15a shows that the slopes at higher latitudes to be around -1, the slopes in Fig. 5.15c are typically between -1 and -0.5, and the slopes at lower latitudes in Fig. 5.15e hover around -0.5. These results are consistent with the global mean RR distribution slopes displayed in Table 5.5.

Figure 5.16 shows the zonal distributions of the probability of rainfall in the different TPW ranges. In Fig. 5.16a, the values between 20° N and 20° S are considered to be

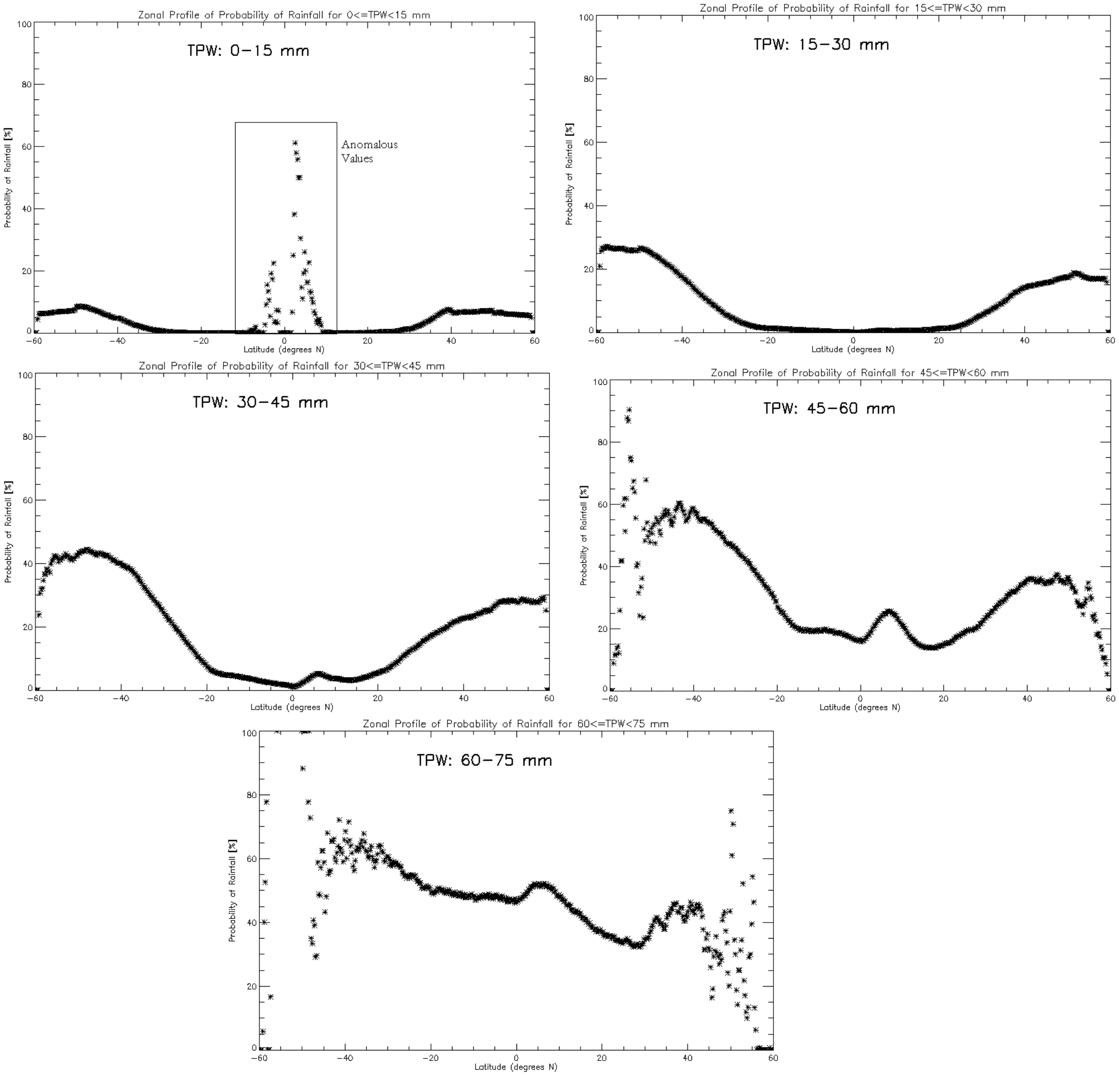

FIG. 5.16. Quasi-global zonal mean probability of rainfall according to TPW ranges (a) 0-15 mm, (b) 15-30 mm, (c) 30-45 mm, (d) 45-60 mm, and (e) 60-75 mm. All 35 months of data were used to calculate these distributions. The box in the tropical region of (a) indicates anomalous values.

anomalous since these tropical latitudes rarely experience TPW values so low. It would be strange for rainfall to occur at such relatively low TPW values in the tropics. Additionally, in Fig. 5.16b, the probability of rainfall at the tropical latitudes is essentially zero, which is further evidence that any significant probability of rainfall in the tropics for very low TPW is not a physical result. These anomalous values are thought to be occurring in coastal regions, where TPW retrievals are more prone to error. In Table 5.6, the first row (i.e., the TPW range between 0 and 15 mm) displays corrected values. That is, the probabilities of rainfall between 20° N and 20° S were re-assigned to be 0% because the original probabilities are considered to be anomalous, as described above.

Figure 5.16a, b, and c demonstrate that rainfall is much more probable in the midlatitudes than in the tropics for these lower TPW values. This result is due to the zonal distribution in TPW; the higher latitudes tend to experience lower TPW values. In addition, rainfall becomes more probable at the higher latitudes as TPW increases. Rainfall in the tropics only becomes significantly probable for TPW values greater than 45 mm, as shown by Fig. 5.16d and e. This makes sense because the low latitudes tend to experience relatively high TPW values, as seen in the annual mean (Fig. 5.1). For TPW greater than 60 mm in the tropics, the probability of rainfall is about 50%, which is consistent with the value given in Table 5.6. In sum, rainfall poleward of about 30° may occur for TPW values between 0 and 60 mm, while tropical rainfall generally occurs only for TPW values greater than 45 mm. One consideration with regard to these TPW-differentiated RR distributions is that TPW may not be measured during a rainfall event, as will be further examined in Sec. 5.4.1. In actuality, the probabilities of rainfall could be higher since rainfall events concurrent with a missing TPW value were not considered.

5.4 Regional Studies

The nine locations more extensively studied were chosen to be representative of the different oceanic climate regimes. Their approximate locations are detailed in Table 5.7 and in Fig. 5.17. The plots at different locations are done for all 35 months of data, but for only one grid point, as opposed to the inclusion of several surrounding grid points. In an earlier investigation not detailed in this thesis, it was found that the statistics for a location do not

TABLE 5.7. Approximate locations of intensive study areas.

Location	**Longitude**	**Latitude**
East of Florida	70° W	30° N
Indian Ocean	75° E	8° S
East of Japan	142° E	35° N
South of Panama	83° W	4° N
South Atlantic Ocean	22° W	45° S
North Atlantic Ocean	30° W	50° N
West Pacific	155° E	6° N
Southeastern Pacific	120° W	8° S
South Pacific Convergence Zone	170° E	10° S

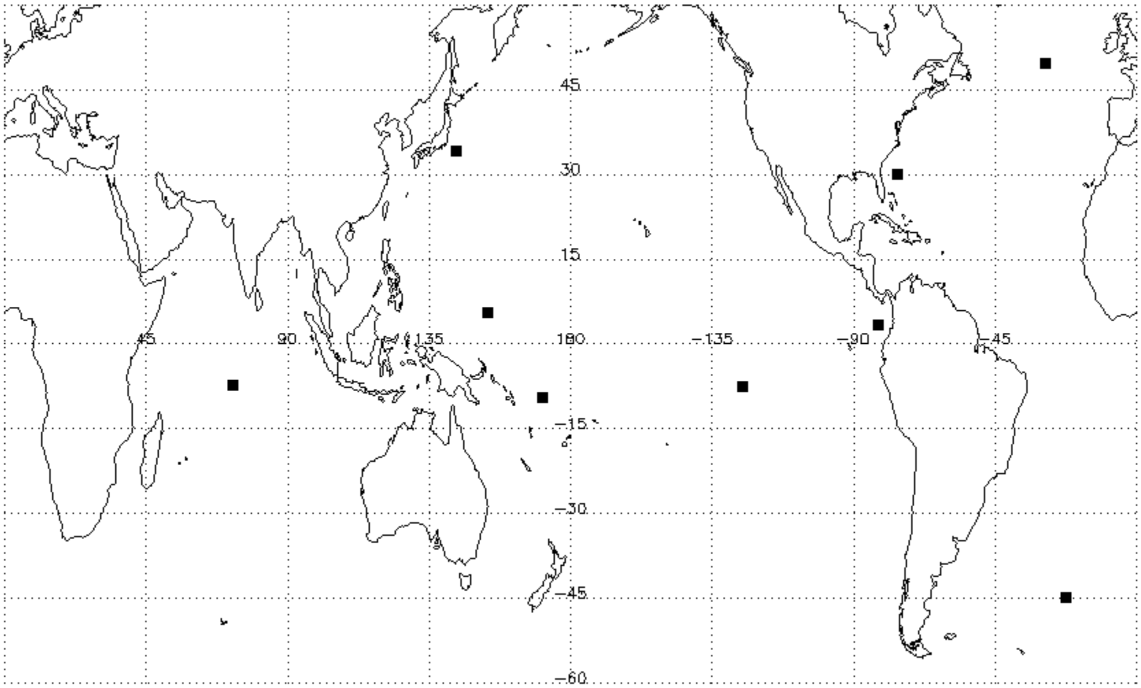

FIG. 5.17. Approximate locations of the nine intensive study areas.

essentially change as the size of the domain is changed from one grid point to 0.75°, 3°, or 10° grid boxes. Thus, the data at one grid point display the characteristics of a region as well as the data from a larger domain do.

5.4.1 June 2007 Time Series

The time period of 1-30 June 2007 was chosen to display time series of TPW and RR data at two locations because data are available at each time period during this particular month. In this way, a complete time series could be constructed without the need to fill in any time gaps. The horizontal line at RR=0.1 mm hr^{-1} in the RR time series plots indicates the rain/no-rain threshold.

The probable reason that the TPW varies so little each day is that the bTPW data product results from 12 hours of data. Although Wu et al. (2003) found that TPW has a noticeable diurnal cycle, the bTPW processing effectively eliminates this. Wu et al. (2003) also found that, although this diurnal cycle in TPW exists, the magnitude of its variation is only around 4 mm even over typically moist Sumatra Island. Any large variations in TPW will most likely occur on the time scale of days. Rain rate, however, varies on a time scale of minutes to hours, as is evident from the RR time series shown in Figs. 5.18-5.19b.

These concurrent TPW and RR time series also demonstrate the inability of the satellite sensors to successfully detect the TPW if rain is falling. For all locations, the TPW is missing at numerous timesteps, often at the same time period as when rain is detected. When TPW is observed when rain is present, the likely explanation is that the TPW was measured either before or after the rain event. For instance, in Fig. 5.18 on day 175, a heavy rain event was observed, and the concurrent TPW was also measured. In contrast, on day 178, a much lighter rain event occurred, but TPW could not be accurately detected, likely because the satellite was viewing the area when the rain was falling. In the opposite sense, when neither TPW nor any rain is measured, it is likely that the TPW was measured when it was raining, but the RR was measured before or after any rain event. Although both RR and TPW are estimated using measurements from sensors on the same satellites, the CMORPH and bTPW data products use different methods to combine these data. For example, if a TMI RR measurement was chosen for the CMORPH product and a combination of AMSU and

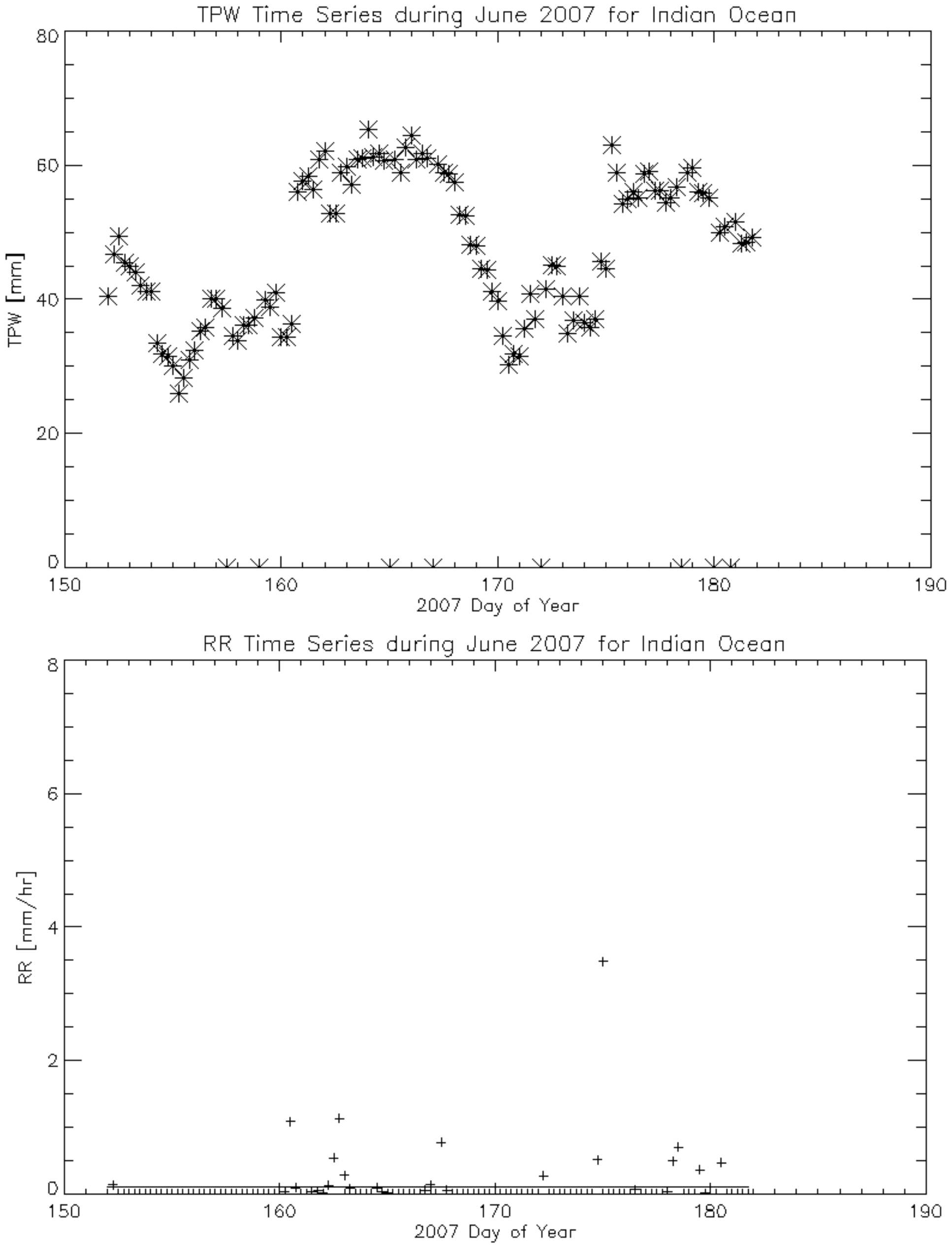

FIG. 5.18. Time series of (a) TPW and (b) RR in the Indian Ocean location during June 2007.

SSM/I measurements were used to form the bTPW product, all 3 measurements may have been taken at different times, resulting in the sorts of inconsistencies seen in these time series. Figure 5.19 supports this theory. For all rain events before day 180, TPW was successfully detected. Around day 180, however, the RR is never observed to be below

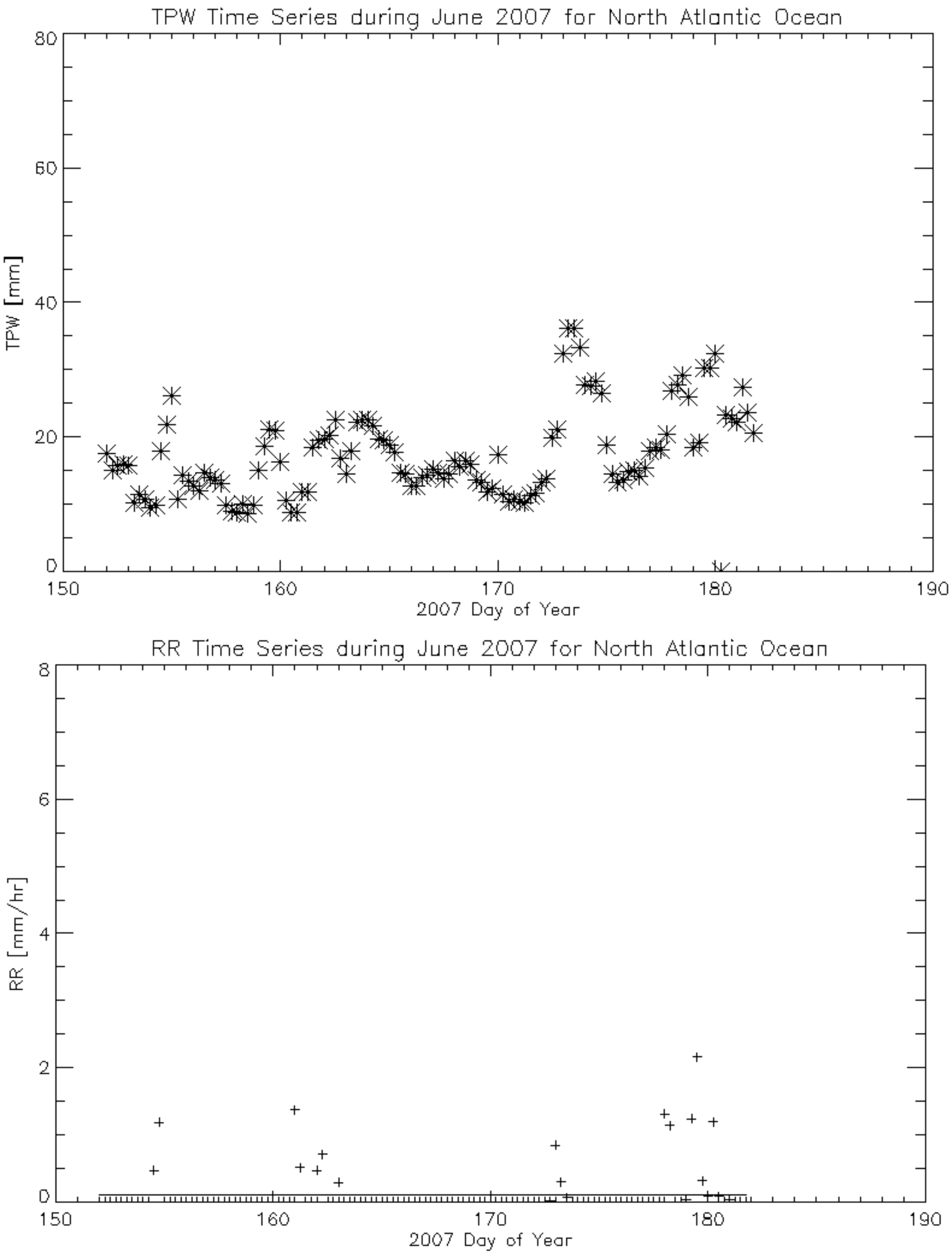

FIG. 5.19. Time series of (a) TPW and (b) RR in the North Atlantic Ocean location during June 2007.

the rain/no-rain threshold and, as predicted, TPW could not be detected. While sporadic rain events may or may not preclude a TPW measurement, a long-lived event such as the one observed in Fig. 5.19 will likely make a valid TPW estimation impossible.

5.4.2 TPW and RR Distributions

The areas located in the western ocean storm tracks (i.e., off the east coasts of Florida and Japan; Fig. 5.20a and c) have the broadest distributions of TPW, which is most likely due to the seasonal changes in TPW as a result of the migration of the maximum solar irradiance. Supporting this fact are Amenu and Kumar (2005), who state that "interseasonal variability attains a maximum around the midlatitudes and a minimum around equatorial and polar areas." In tropical areas, shown in Figs. 5.20b, d, g, and i, the TPW distributions are skewed right, having a greater proportion of high rather than low TPW values. The opposite is true in Fig. 5.20e, f, and h, which display skew-left distributions, representative of areas generally having lower TPW. These results are expected from the quasi-global TPW annual mean plot shown in Fig. 5.1.

As Fig. 5.21 shows, the rain rate distributions are relatively similar at all locations in that they all approximate exponential decay, even though the rainfall amounts and frequencies are vastly different from location to location. Over the southeastern Pacific (Fig. 5.21h), rain occurred about 2.3% of the time. In contrast, rain occurred 31.2% of the time in the west Pacific warm pool (Fig. 5.21g). An exponential fit was applied to each distribution, as described in Sec. 4.3. These exponentially-fit RR distributions can be seen in Fig. 5.22, where it is evident that taking the natural logarithm of the proportion of total occurrences results in an approximately linear trend, which is the trademark of exponential decay. The slopes of each distribution can be found in Table 5.8 along with the mean TPW and rainfall frequency at each location. The results indicate that typically drier regions (i.e. regions with low rainfall frequencies and relatively low mean TPW), such as the southeastern Pacific, are associated with a steeper (i.e., more negative) rate of decay relative to areas receiving rain more frequently. A quicker exponential decay here is associated with fewer heavy rain events

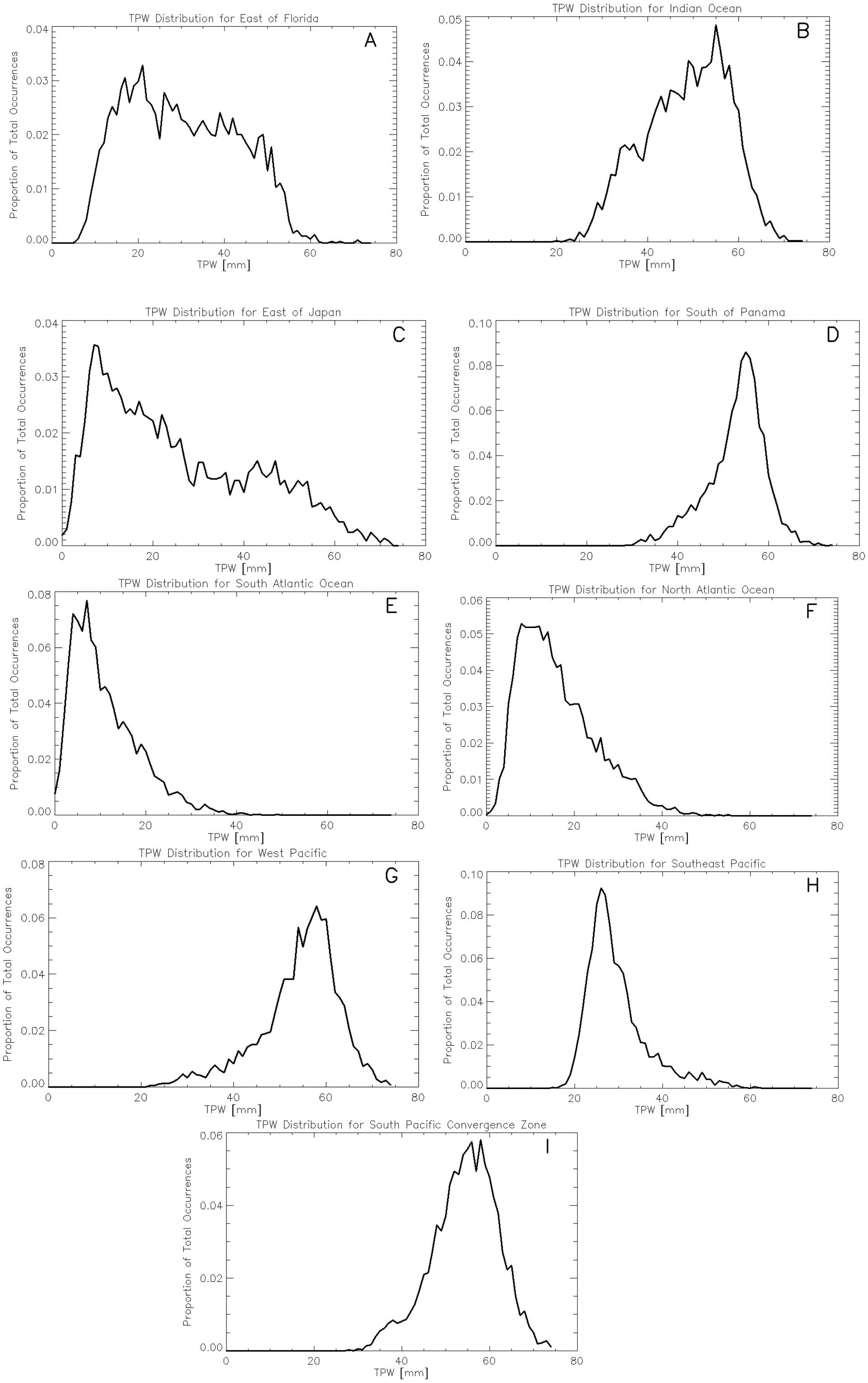

FIG. 5.20. Annual mean TPW distributions for each location: (a) East of Florida, (b) Indian Ocean, (c) East of Japan, (d) South of Panama, (e) South Atlantic Ocean, (f) North Atlantic Ocean, (g) West Pacific, (h) Southeast Pacific, and (i) South Pacific Convergence Zone. All 35 months of data were used to calculate these distributions. The y-axis displays the proportion of total occurrences; the scale varies from plot to plot.

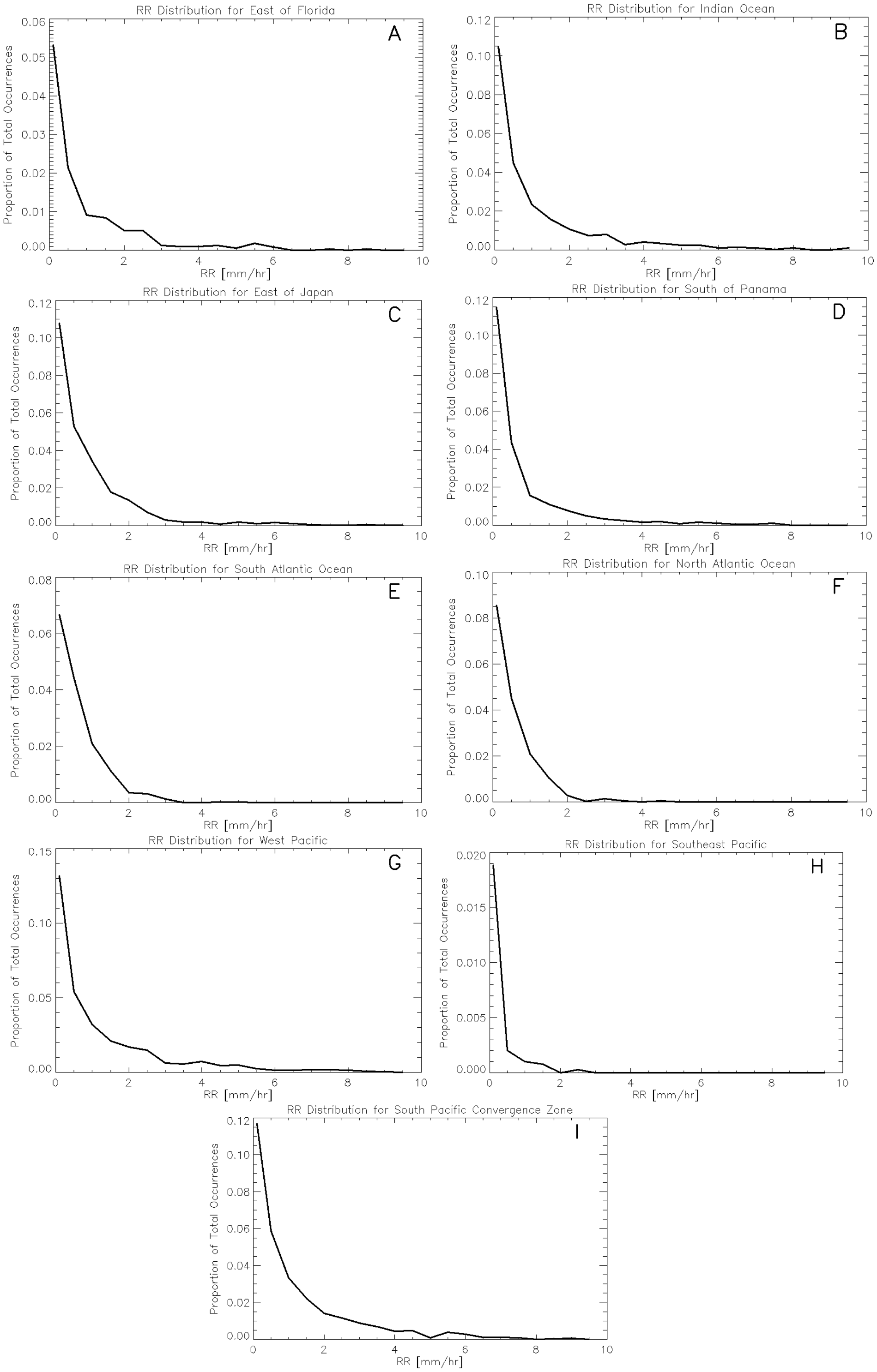

FIG. 5.21. Annual mean RR distributions for each location: (a) East of Florida, (b) Indian Ocean, (c) East of Japan, (d) South of Panama, (e) South Atlantic Ocean, (f) North Atlantic Ocean, (g) West Pacific, (h) Southeast Pacific, and (i) South Pacific Convergence Zone. All 35 months of data were used to calculate these distributions. The y-axis displays the proportion of total occurrences; the scale varies from plot to plot.

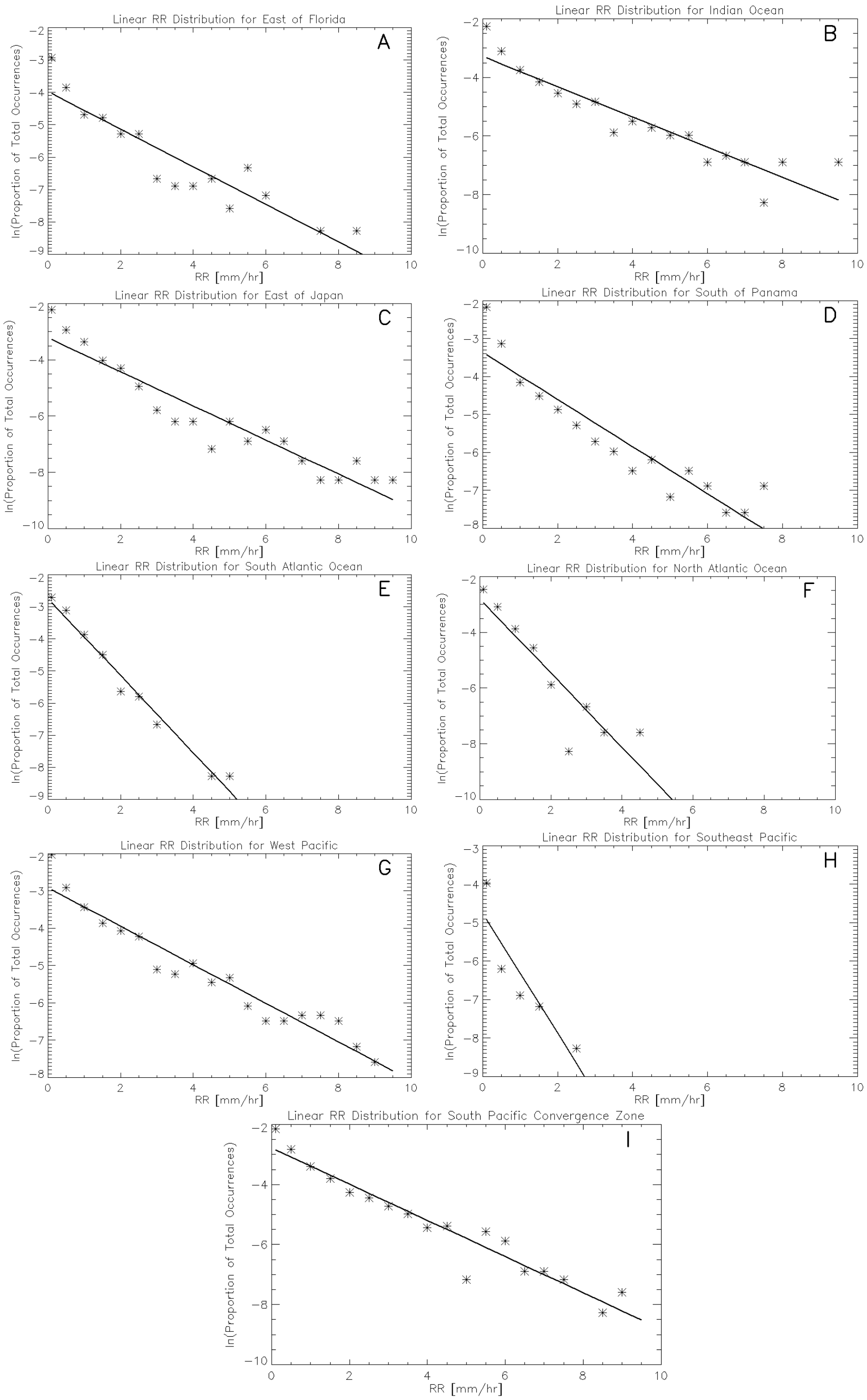

FIG. 5.22. Annual mean RR distribution for each location plotted with its exponential fit: (a) East of Florida, (b) Indian Ocean, (c) East of Japan, (d) South of Panama, (e) South Atlantic Ocean, (f) North Atlantic Ocean, (g) West Pacific, (h) Southeast Pacific, and (i) South Pacific Convergence Zone. All 35 months of data were used to calculate these distributions. The y-axis displays the natural logarithm of the proportion of total occurrences; the scale varies from plot to plot.

relative to the amount of light rain events. The slower exponential decay is then associated with more heavy rain events relative to the number of light rain events. For instance, Figs. 5.21g and 5.22g display a shallower slope and a higher proportion of heavy RRs when compared with the steeper-sloped Figs. 5.21f and 5.22f. These results imply that vastly different RR distributions are associated with different rainfall characteristics in these types of areas. The southeastern Pacific is generally covered by marine stratocumulus clouds, which are not associated with heavy rainfall, while the western Pacific frequently experiences convective rain events, which are able to produce much heavier rainfall.

TABLE 5.8. Slopes of the exponentially-fit RR distributions, mean TPW, and rainfall frequency for each location.

Location	**Slope of Exponential Fit**	**Mean TPW [mm]**	**Rainfall Frequency [%]**
East of Florida	-0.580	30.66	11.11
Indian Ocean	-0.516	48.49	23.71
East of Japan	-0.605	25.69	24.96
South of Panama	-0.621	52.86	21.29
South Atlantic Ocean	-1.200	11.04	15.16
North Atlantic Ocean	-1.328	16.18	16.76
West Pacific	-0.516	54.28	31.20
Southeastern Pacific	-1.556	29.62	2.29
South Pacific Convergence Zone	-0.603	54.42	29.37

Figure 5.23 displays the seasonal variations in the location east of Florida. This midlatitude location experiences more seasonal variations than the tropical location in the western Pacific (Fig. 5.24). As is evident in Table 5.9, the mean TPW in the location east of Florida has a seasonal mean range of 19.6 mm while the mean TPW in the western Pacific location varies less than 5 mm on average. In addition, the slopes of the RR distributions are much more variable in the location east of Florida than in the western Pacific location. In this way, annual mean TPW and RR values should be fairly representative of tropical locations throughout the year, while seasonal mean values are necessary to describe a midlatitude region's more variable TPW and RR distributions.

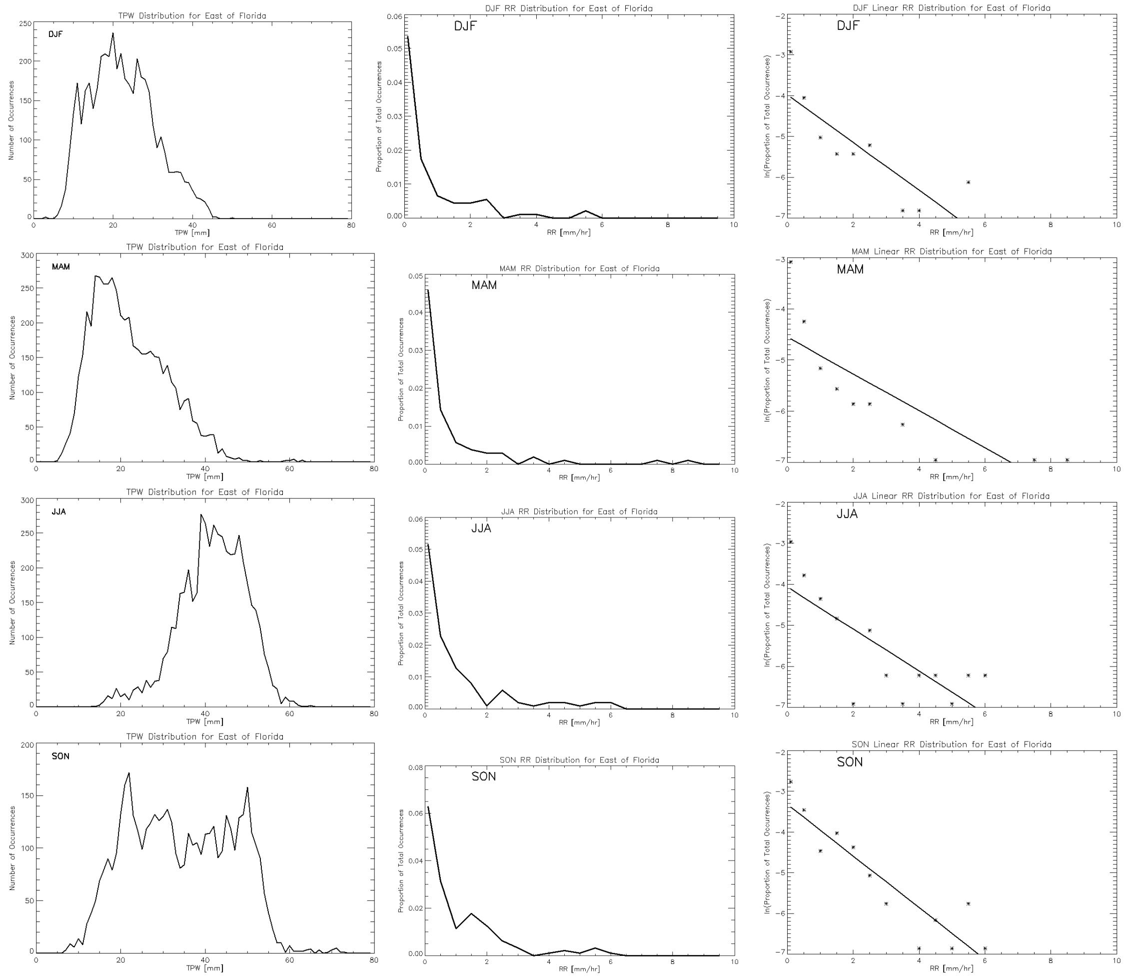

FIG. 5.23. Seasonal TPW, RR, and exponentially-fit RR distributions for DJF, MAM, JJA, and SON for the location east of Florida. The scale of the y-axis changes from plot to plot.

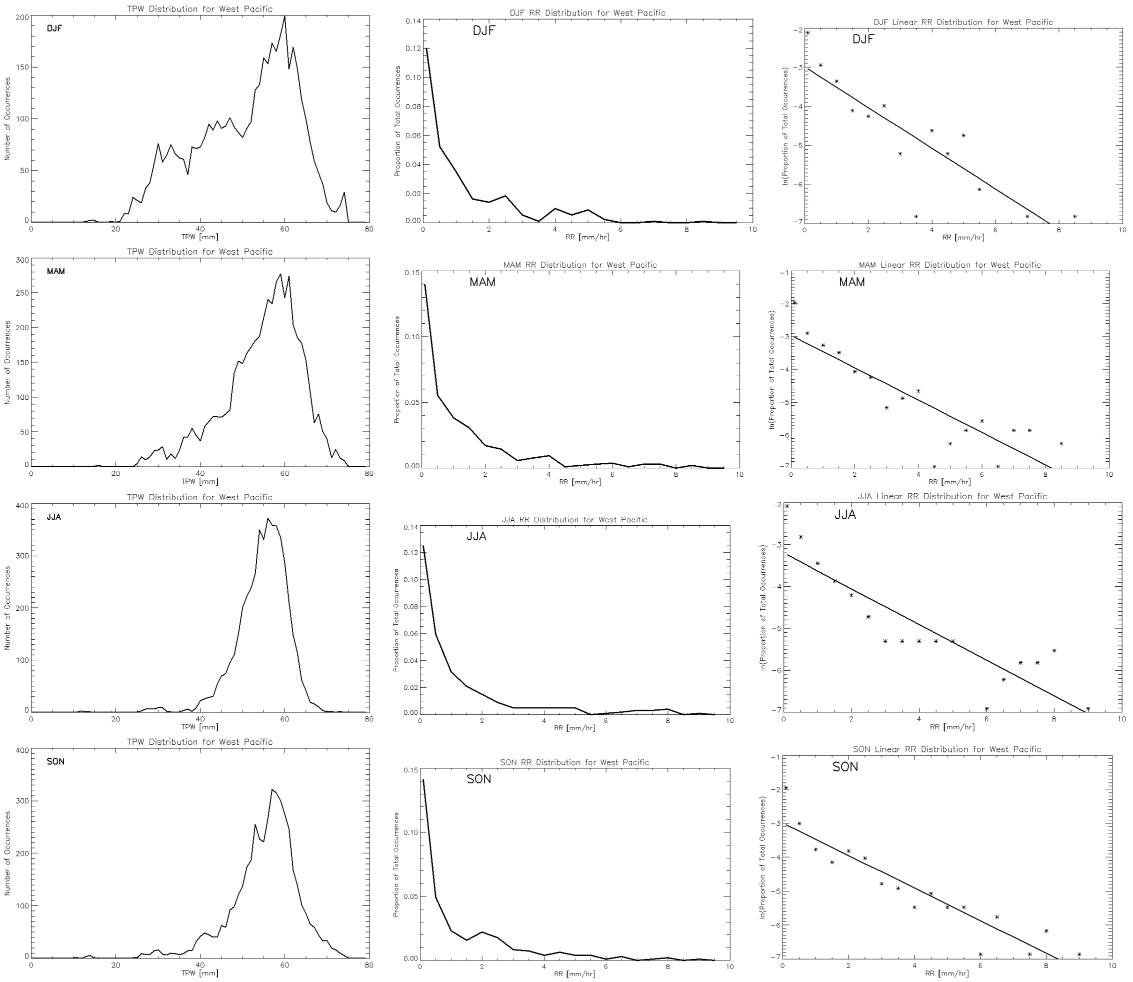

FIG. 5.24. Seasonal TPW, RR, and exponentially-fit RR distributions for DJF, MAM, JJA, and SON for the location in the west Pacific. The scale of the y-axis changes from plot to plot.

TABLE 5.9. Slopes of the exponentially-fit RR distributions and mean TPW in DJF, MAM, JJA, and SON for the locations east of Florida and in the west Pacific.

Location	Season	Slope of Exponential Fit	Mean TPW [mm]
East of Florida	DJF	-0.59	22.29
	MAM	-0.36	22.07
	JJA	-0.51	41.69
	SON	-0.64	34.30
West Pacific	DJF	-0.52	50.79
	MAM	-0.49	54.73
	JJA	-0.43	54.73
	SON	-0.48	55.21

5.4.3 TPW vs RR

Figure 5.25 displays the scatter plots of RR vs. TPW at each location. While an initial hypothesis estimates that higher RRs correspond to higher TPW values, this is not the case. Rather, it appears that these plots are similar to the corresponding TPW distributions shown in Fig. 5.20. This result indicates that TPW does not imply RR, but that rain occurs in the presence of almost any TPW value. However, high RRs (i.e., RR$\geq$5 mm hr^{-1}) are more likely in regions with typically higher TPW values (e.g. the western Pacific and the Indian Oceans), while these RRs are generally absent from drier regions (e.g., the north Atlantic and the southeastern Pacific Oceans). RR=0 is observed at nearly every TPW value in each plot since, in some cases, the other factors necessary for rain to fall were not present. Because rain typically falls at certain TPW values according to the region being observed, a threshold for the occurrence of rain or heavy rain could be estimated. For instance, in the region south of Panama (Fig. 5.25d), RRs greater than 1 mm hr^{-1} are virtually nonexistent for TPW values less than about 45 mm. A forecaster for that area would then deem rainfall unlikely and heavy rainfall even less likely if the TPW in that area were less than about 45 mm.

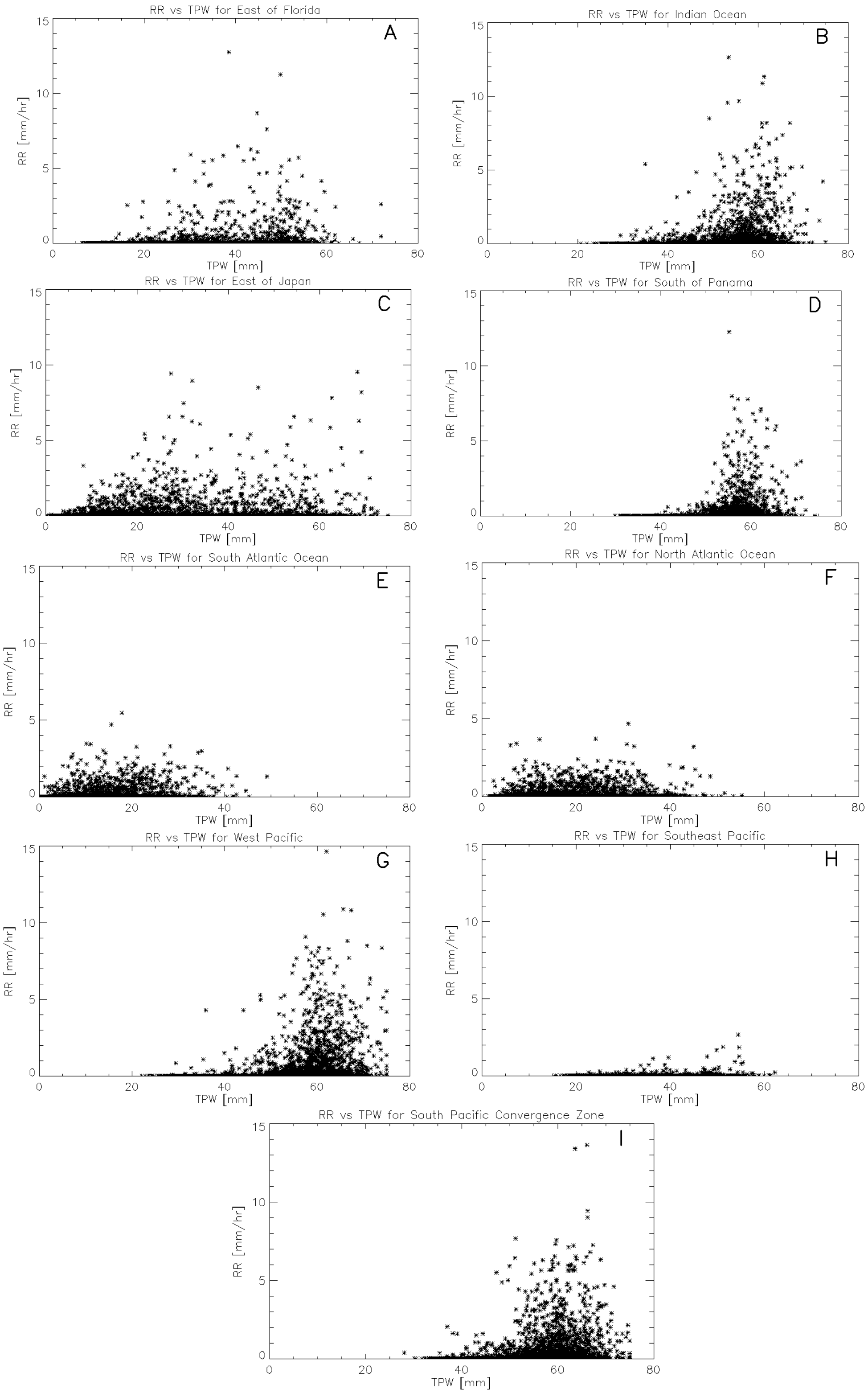

FIG. 5.25. RR vs TPW for each location: (a) East of Florida, (b) Indian Ocean, (c) East of Japan, (d) South of Panama, (e) South Atlantic Ocean, (f) North Atlantic Ocean, (g) West Pacific, (h) Southeast Pacific, and (i) South Pacific Convergence Zone. All 35 months of data were used to populate these plots.

5.4.4 Probability of Rainfall

As the rain intensity increases, rainfall becomes less likely for lower TPW values. For instance, in the region east of Florida (Fig. 5.26a), rainfall has a significant probability (e.g., greater than 15%) for TPW≥30mm, but a RR≥0.5 mm hr^{-1} does not become probable unless TPW is greater than about 50 mm (Fig. 5.27a). RR≥3.0 mm hr^{-1} is fairly improbable at all TPW values at all locations, with an exception for high TPW values in typically moist locations (Figs. 5.28b, d, g, and i). This result indicates that, while the probability of rainfall generally increases with TPW in several locations and this TPW threshold increases for slightly higher RRs, predicting heavy rainfall simply using TPW as a factor is not a valid method. When the probability of rainfall is 100% for a given TPW value (e.g., Fig. 5.27e at 39 and 49 mm of TPW), this is probably indicative of a single occurrence of that TPW value that happened to coincide with a rainfall event at or above the given threshold and is not likely indicative of a consistently high probability of rainfall.

Another feature of these conditional probability plots is that the typically drier areas (such as the South Atlantic, North Atlantic, and southeastern Pacific Oceans) have rain occurring at lower TPW values. For example, a 20% chance of rain first occurs for TPW=50 mm in the western Pacific (Fig. 5.26g), but a 20% chance of rain first occurs for TPW=13 mm in the south Atlantic Ocean (Fig. 5.26e), a typically dry region. One explanation for this fact is that low TPW values are very infrequent in very moist areas (e.g., Fig. 5.20g), while low TPW values are very frequent in drier areas (e.g. Fig. 5.20e). Perhaps moister regions would experience more rainfall at lower TPW values if these low TPW values were ever present.

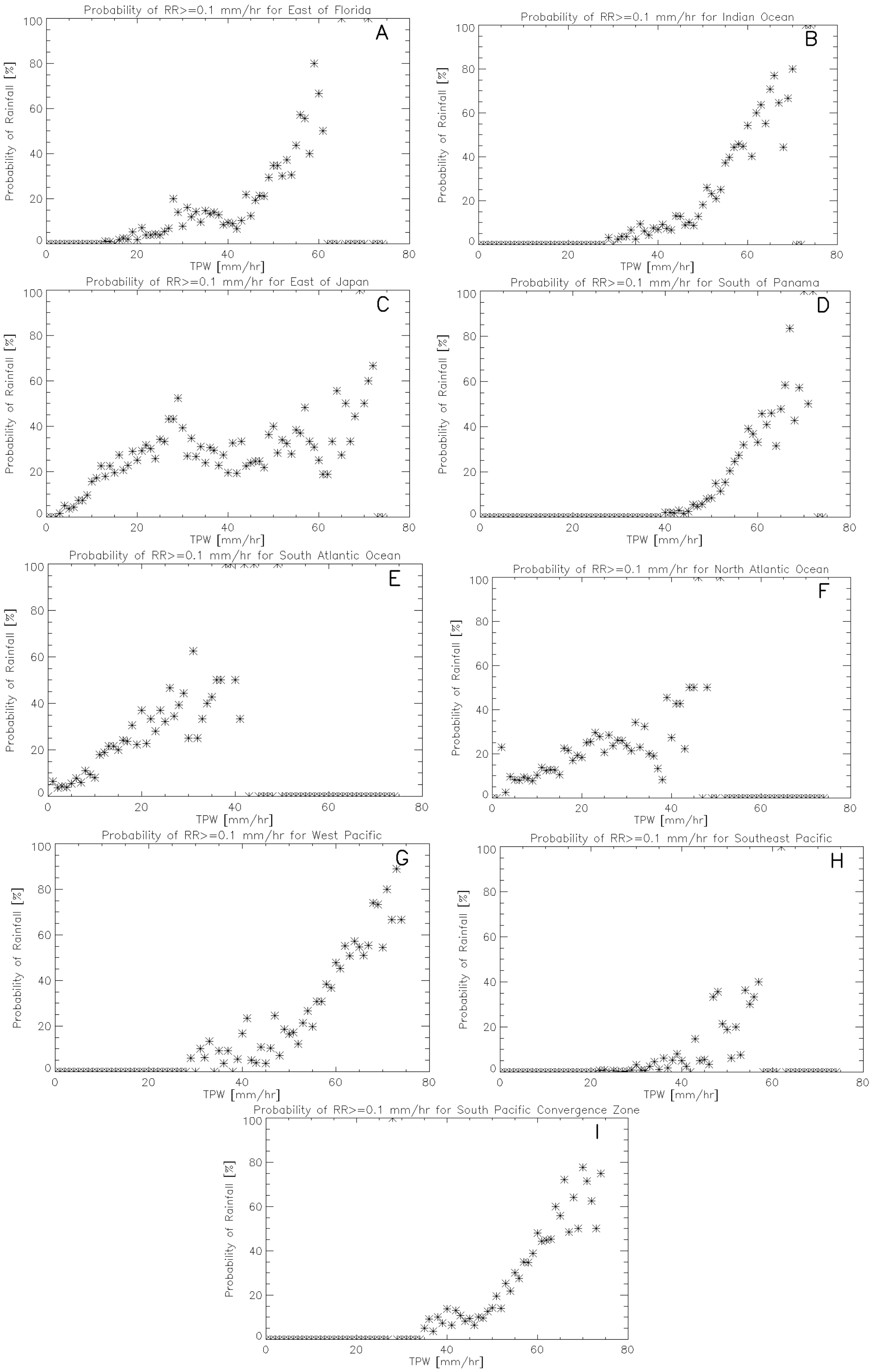

FIG. 5.26. Probability of RR ≥ 0.1 mm hr^{-1} given TPW for each location: (a) East of Florida, (b) Indian Ocean, (c) East of Japan, (d) South of Panama, (e) South Atlantic Ocean, (f) North Atlantic Ocean, (g) West Pacific, (h) Southeast Pacific, and (i) South Pacific Convergence Zone. All 35 months of data were used to calculate these values.

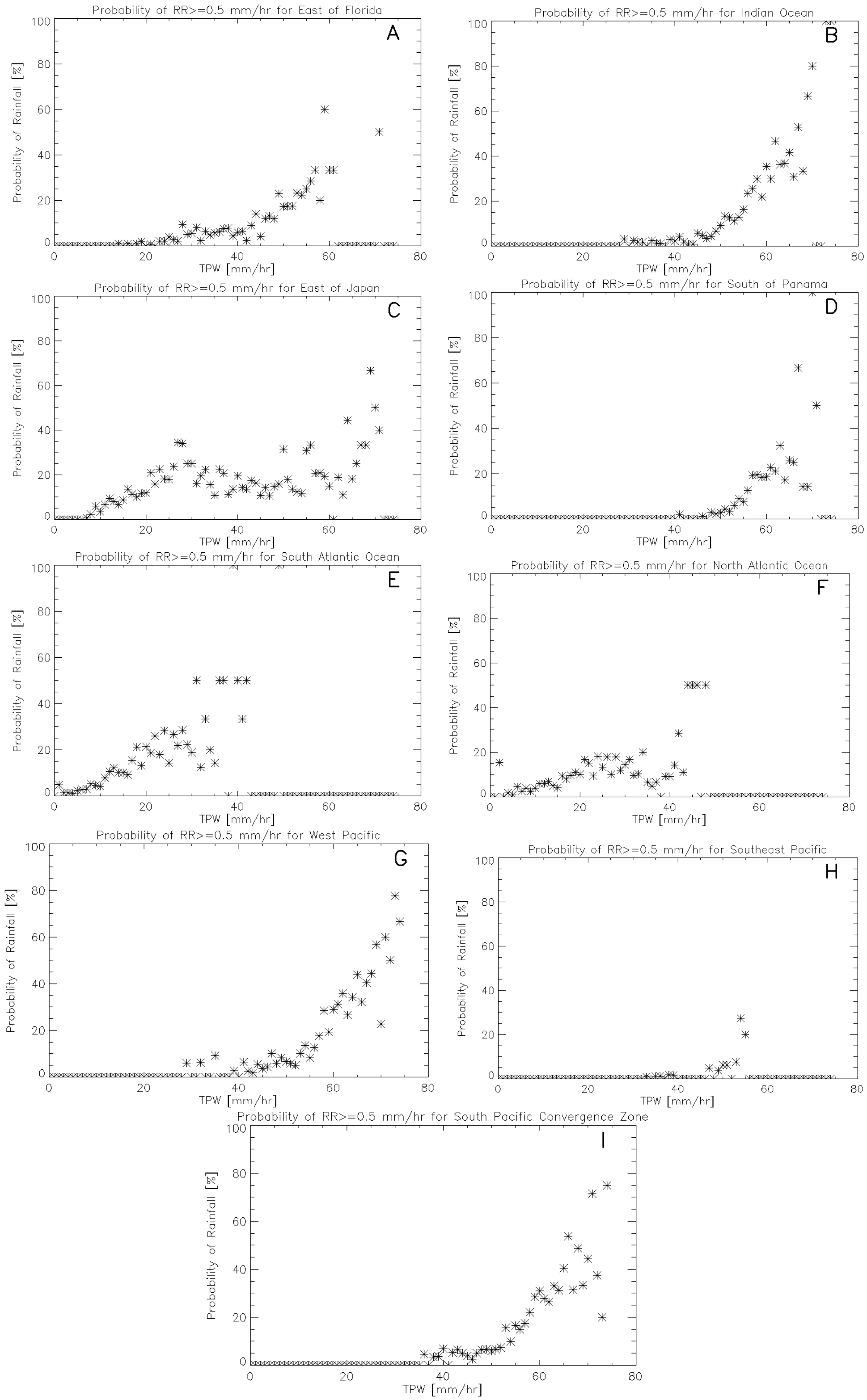

FIG. 5.27. Probability of RR ≥ 0.5 mm hr^{-1} given TPW for each location: (a) East of Florida, (b) Indian Ocean, (c) East of Japan, (d) South of Panama, (e) South Atlantic Ocean, (f) North Atlantic Ocean, (g) West Pacific, (h) Southeast Pacific, and (i) South Pacific Convergence Zone. All 35 months of data were used to calculate these values.

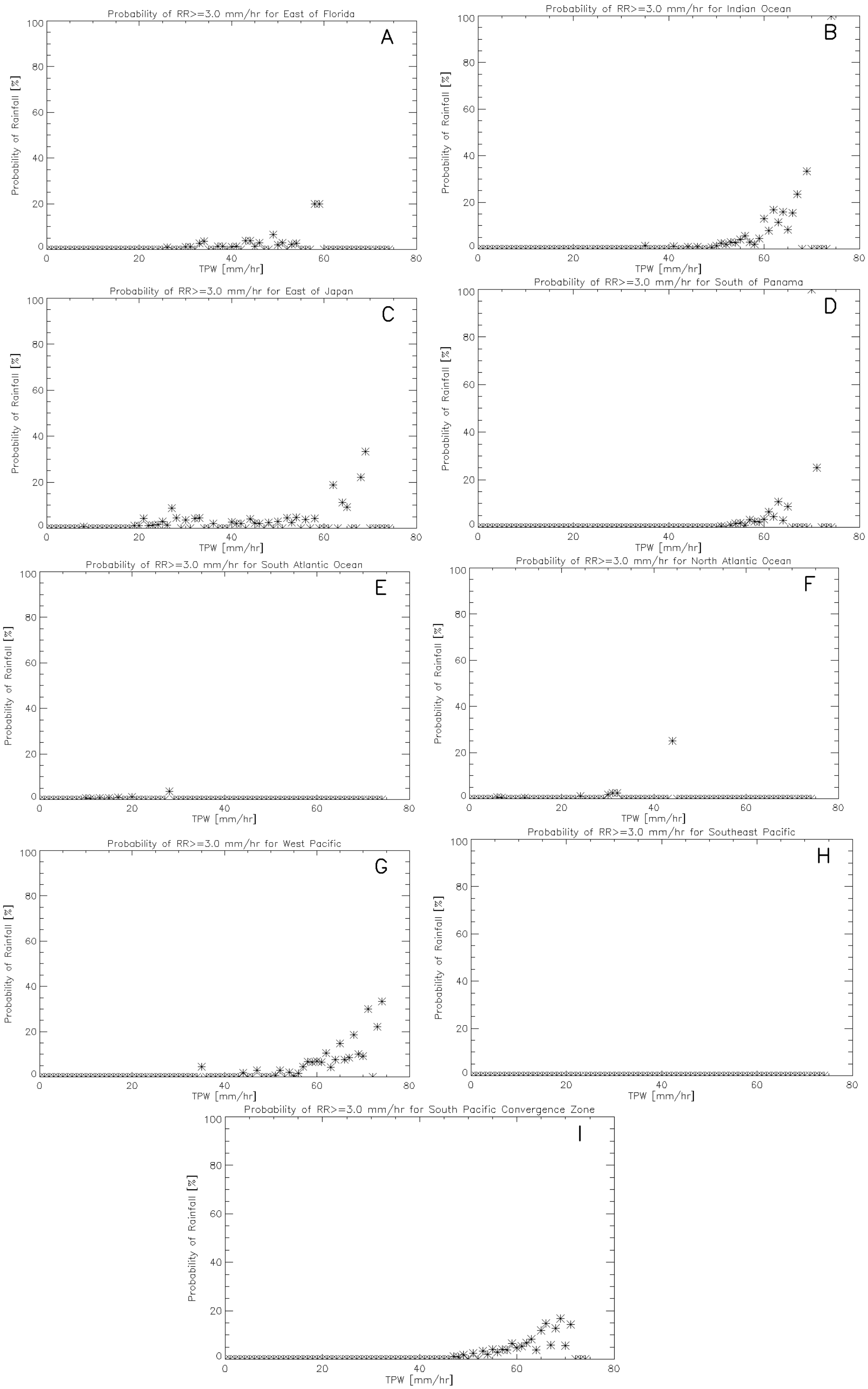

FIG. 5.28. Probability of RR ≥ 3.0 mm hr^{-1} given TPW for each location: (a) East of Florida, (b) Indian Ocean, (c) East of Japan, (d) South of Panama, (e) South Atlantic Ocean, (f) North Atlantic Ocean, (g) West Pacific, (h) Southeast Pacific, and (i) South Pacific Convergence Zone. All 35 months of data were used to calculate these values.

6. CONCLUSIONS AND FUTURE WORK

6.1 Conclusions

The climatological patterns identified in this 35 month quasi-global study are consistent with findings from previous studies, a result which indicates that the bTPW and CMORPH datasets are providing physical observations. In general, the highest oceanic TPW values are found in the ITCZ, west Pacific warm pool, and SPCZ while the lowest TPW values occur in the higher latitudes and in the oceanic desert areas off the subtropical west coasts of North America, South America, and northern and southern Africa. Similarly, the highest oceanic rainfall values and frequencies are located in the ITCZ, west Pacific warm pool, SPCZ, and midlatitude storm tracks while the lowest occur in the oceanic desert areas. Over land, rainfall totals and rainfall frequencies are at their highest over the Amazon basin and the sub-Saharan savannas and rainforests. The quasi-global mean TPW is 24.94 mm, a slight overestimate of the NVAP global mean (Sudradjat et al. 2005) as a result of this domain's exclusion of most land areas and of any data poleward of 60°. The quasi-global mean RR is 2.63 mm day^{-1}, which is close to the values presented by Xie and Arkin (1997) in Table 2.1.

The CMORPH quasi-global rainfall and rainfall frequency distributions are in approximate agreement with results from Legates and Willmott (1990), Ferraro et al. (1996), and even McDonald (1938; see Appendix C). This approximate agreement of older results with newer datasets provides evidence that the climatological rainfall patterns over the domain may not have undergone significant changes during this century.

Since rainfall frequency is somewhat analogous to total rainfall, as is evident when comparing Figs. 5.5 and 5.6, it can be concluded that very heavy rainfall does not contribute to the majority of rainfall in any given area. Rather, according to Figs. 5.13 and 5.21, most of an area's rain results from an abundance of light rainfall events and fewer heavy rainfall events, with the RR distribution forming an approximate exponential decay. The slope of the exponential fit is related to the frequency of rainfall, with more negative slopes being associated with lower rainfall frequency, as shown in Table 5.8.

In a global sense, more negative slopes are associated with lower TPW values. That is, higher RRs are more likely when more TPW is present. However, as discussed in Sec. 2.4, atmospheric dynamics play an important role in the spatial distribution of TPW and rainfall, with more rainfall and higher TPW values typically occurring in areas of moisture convergence and upward air flow. So although heavier rainfall typically occurs in the presence of increased TPW as shown in Fig. 5.13, TPW is not the sole contributor to heavy rainfall events; convection and moisture convergence are also crucial factors. Similarly, moisture divergence and atmospheric subsidence impede the production of rainfall, which results in high RRs tending to be unlikely in areas of typically low TPW. Because dynamical patterns are so critical to rainfall production, using TPW to forecast rainfall is only appropriate when done for a particular region since this study does not correct for dynamical variability (e.g., patterns of moisture convergence and evaporation). Using TPW distributions to predict rainfall in a climatological sense is not supported by this study's results since the occurrence of rainfall depends so heavily on regional dynamics.

On average, rain occurs over about 11.0% of the ocean and 8.6% of the land at any given time, which is in general agreement with Trenberth (1998). Because these results are supported by previous studies, the use of a rain/no-rain threshold of 0.1 mm hr^{-1} is validated since it was used to make these estimations. Rainfall frequency varies greatly with latitude zone and surface type, with the northern tropical oceans experiencing rainfall over as much as 24% of the area and the northern midlatitude land areas receiving rain over as little as 5% of the area at any given time on average, as shown in Fig. 5.6 and in Table 5.2.

Since rain can occur at nearly any RR at nearly any TPW, as the plots in Fig. 5.25 show, an increase in TPW does not necessitate an increase in precipitation in a particular location. While a higher TPW in one region may correspond to a higher likelihood of rain, the cause of the rain in any region depends on local dynamics in order to create the additional conditions necessary for rainfall. The pattern of RR in a particular location tends to mirror the pattern of TPW in that area. That is, higher RRs tend to occur at the peak TPW values, likely due to the fact that those TPW values occur the most frequently. This result indicates that the other factors facilitating the production of rainfall, such as convection, are more likely to be coincident with those TPW values simply because those TPW values are present more frequently. So even though an elevated TPW does not predict the occurrence of a heavier rainfall event, a climatological increase in TPW in a region would mean that the rainfall would tend to occur in the presence of higher TPW values, although the intensity of that rainfall cannot be adequately predicted by this study.

It is important to note certain characteristics of the data used in this study. For instance, the RR algorithms described in Chapter 3 indicate that the sensors do not detect very light rain. However, the RR histograms are populated even at the very low RR values, which is a physical result since light rainfall is common. Since little to no rainfall is detected in the Southeastern Pacific, where drizzle and very light rain are typically the only precipitation types, it is likely that the reason the low ends of the RR histograms are populated is due to averaging within a satellite field of view (FOV). A typical FOV for AMSU-B, for example, is 225 km^2, an area larger than Washington, DC (Joyce et al. 2004). For AMSU-A, the smallest FOV is 2304 km^2, which is roughly the size of Terry County, Texas (Kidder and Jones 2007). The FOV size can be large compared to rain cell size, so the instrument in some cases is detecting a non-uniform precipitation picture. For instance, if a FOV consists of areas of heavier rain mixed with areas of no rain, the result may be a low rain rate. In the Southeastern Pacific Ocean, however, heavier rain is atypical, so little, if any, rain is ever detected. In addition, the TMI and SSM/I are more skilled at detecting convective rain, which supports the underestimated stratiform rainfall amounts in the Southeastern Pacific.

6.2 Future Work

Although operational forecasts would benefit from a study comparing TPW and RR over land, the absence of TPW data over land made this impossible for the current study. When an accurate over-land TPW dataset becomes available, the results from this over-ocean TPW and RR study can be compared to similar measurements observed over land surfaces. The general character of TPW and rainfall is not expected to change drastically over land, although several other factors will need to be considered for that type of study, such as orographic influences on the production of rain. The very heavy rain event in the Appalachian Mountains described in section 2.5.3, for instance, was made possible by the interaction of the dynamics with the topography. Another factor includes the great variety of land surface types, which contribute to land-air interactions. The rainfall data will be better validated over land, since radar data are more readily available over land. An important reason for better understanding where heavy rain will occur is to contribute to more accurate predictions of flash floods and water resources. Rain falling on snow can increase the melting rate, which is another reason supporting improved prediction of over-land rainfall. Topography and soil moisture also affect how the water will behave once it reaches a land surface.

Because detecting TPW when rain is occurring is not possible using passive microwave satellite methods, with the exception of a few cases where TPW is measured before or after the rain event, comparing the two parameters is only possible on a statistical basis. That is, the general characteristics of rainfall in a region may be compared to the general characteristics of local TPW, but individual events may not be analyzed using the data presented in this study. It may be possible to characterize an individual event if realistic TPW values are used to 'fill in' the data gaps when rainfall forbids a TPW measurement. For instance, if TPW was estimated to be 45 mm both before and after the rain event, that value could be assigned to the time of the missing measurement.

Another parameter that may be investigated when a missing TPW value is replaced with an estimation is the precipitation efficiency (i.e., rainfall amount ÷ TPW). This information could be useful for forecasters. For example, if the maximum precipitation efficiency for an area is 5% and the TPW for an area is expected to be 45 mm, the area should expect no more than about 2 mm hr^{-1} of rainfall. Precipitation efficiency may also be seasonally variable, especially in the midlatitudes and in areas experiencing monsoons. Additionally, it would be useful to construct reference mean TPW plots for the domain so that TPW anomaly values, rather than TPW values, may be compared with observations of rainfall.

It would also be interesting to investigate how the RR distributions change for different TPW regimes in particular locations, as was done globally in Sec. 5.3. The RR distributions in the midlatitudes may be seasonally variable in different TPW regimes. Anomalous events, such as the presence of relatively high TPW or RRs, could be characterized by a region's TPW and RR distributions and the corresponding uncharacteristic dynamics could then be further investigated. Viewed regionally, the dynamical variability in TPW and rainfall could be better controlled for than it is in Figs. 5.13-16.

The sensors used in this study are relatively insensitive to the light stratiform rain that is common in oceanic desert regions. The studies which analyzed direct observations of rainfall (i.e., Legates and Willmott (1990); McDonald (1938), see Appendix C) indicate that the satellite methods used in this study are not completely capturing the rainfall patterns in these types of regions. One improvement to this study would be to use CloudSat sensors, which are able to detect these lighter rain events, to supplement the CMORPH dataset.

In addition to studying the relationship between TPW and RR over land and improving comparisons over the ocean, these datasets could be incorporated into forecast or climate models. This study shows how TPW and RR distributions vary from location to location and how the RR distributions may be characterized by the slope of an exponential decay equation. Incorporating these regional TPW and RR characteristics could improve a model's accuracy. In addition, the current observed quasi-global distributions of TPW and rainfall, including frequencies of occurrence, could aid in validating climate models' initial conditions and in identifying significant variations for a model run to different future times. The TPW and RR distributions could also be compared with new satellite observations, either for validation purposes or to identify actual climatological changes in different regions.

REFERENCES

American Meteorological Society Glossary of Meteorology Website. Available at: http://amsglossary.allenpress.com/glossary.

Amenu, G. G., and P. Kumar, 2005: NVAP and Reanalysis-2 global precipitable water products: Intercomparison and variability studies. *Bull. Amer. Meteor. Soc.*, **86**, 245-256.

Bennartz, R., and P. Bauer, 2003: Sensitivity of microwave radiances at 85-183 GHz to precipitating ice particles. *Radio Sci.*, **38**, 8075, doi: 10.1029/2002RS002626.

CIRA Experimental Merged Total Precipitable Water Products Website. Available at: http://amsu.cira.colostate.edu/gpstpw/.

CMORPH Website. Available at: http://www.cpc.noaa.gov/products/janowiak/cmorph_description.html.

Dai, A., J. Wang, R. H. Ware, and T. Van Hove, 2002: Diurnal variation in water vapor over North America and its implications for sampling error in radiosonde humidity. *J. Geophys. Res.*, **107**, 4090, doi: 10.1029/2001JD000642.

Dinku, T., and E. N. Anagnostou, 2006: TRMM calibration of SSM/I algorithm for overland rainfall estimation. *J. Appl. Meteorol. Climatol.*, **45**, 875-886.

Ferraro, R. R., and G. F. Marks, 1995: The development of SSM/I rain-rate retrieval algorithms using ground-based radar measurements. *J. Atmos. Oc. Tech.*, **12**, 755-770.

----, F. Weng, and N. C. Grody, 1996: An eight-year (1987-1994) time series of rainfall, clouds, water vapor, snow cover, and sea ice derived from SSM/I measurements. *Bull. Amer. Meteor. Soc.*, **77**, 891-905.

----, 1997: Special sensor microwave imager derived global rainfall estimates for climatological applications. *J. Geophys. Res.*, **102**, 16715-16735.

----, F. Weng, N. C. Grody, L. Zhao, H. Meng, C. Kongoli, P. Pellegrino, S. Qiu, and C. Dean, 2005: NOAA operational hydrological products derived from the Advanced Microwave Sounding Unit. *IEEE Trans. Geosci. Remote Sensing*, **43**, 1036-1049.

Grody, N., J. Zhao, R. Ferraro, F. Weng, and R. Boers, 2001: Determination of precipitable water and cloud liquid water over oceans from the NOAA 15 advanced microwave sounding unit. *J. Geophys. Res.*, **106**, 2943-2953.

Hartmann, D. L., 1994: Global Physical Climatology. *Academic Press*, 411 pp.

Janowiak, J. E., V. E. Kousky, and R. J. Joyce, 2005: Diurnal cycle of precipitation determined from the CMORPH high spatial and temporal resolution global precipitation analyses. *J. Geophys. Res.*, **110**, D23105, doi: 10.1029/2005JD006156.

Joyce, R. J., J. E. Janowiak, P. A. Arkin, and P. Xie, 2004: CMORPH: A method that produces global precipitation estimates from passive microwave and infrared data at high spatial and temporal resolution. *J. Hydrometerol.*, **5**, 487-503.

Junker, N. W., R. H. Grumm, R. Hart, L. F. Bosart, K. M. Bell, and F. J. Pereira, 2008: Use of normalized anomaly fields to anticipate extreme rainfall in the mountains of Northern California. *Wea. Forecasting*, **23**, 336-356.

Keighton, S. J., M. Gillen, G. V. Loganathan, S. Gorugantula, and T. Eisenberger, 2001: The use of GPS integrated precipitable water measurements to supplement WSR-88D parameters in determining the potential for flash flood producing rainfall. AMS 9th Conference on Mesoscale Processes. July 30-August 2, 2001, Fort Lauderdale, FL.

Kidder, S. Q., and T. H. Vonder Haar, 1995: Satellite Meteorology: An Introduction. *Academic Press*, 456 pp.

----, and A. S. Jones, 2007: A blended satellite total precipitable water product for operational forecasting. *J. Atmos. Oc. Tech.*, **24**, 74-81.

Kummerow, C., W. S. Olson, and L. Giglio, 1996: A simplified scheme for obtaining precipitation and vertical hydrometeor profiles from passive microwave sensors. *IEEE Trans. Geosci. Remote Sensing*, **34**, 1213-1232.

----, Y. Hong, W. S. Olson, S. Yang, R. F. Adler, J. McCollum, R. Ferraro, G. Petty, D.-B. Shin, and T. T. Wilheit, 2001: The evolution of the Goddard Profiling Algorithm (GPROF) for rainfall estimation from passive microwave sensors. *J. Appl. Meteorol.*, **40**, 1801-1820.

Legates, D. R., and C. J. Willmott, 1990: Mean seasonal and spatial variability in gauge-corrected, global precipitation. *Int. J. Climatol.*, **10**, 111-127.

Levizzani, V., 1998: Intense rainfall monitoring from geostationary satellites. Prepr. AMS 9th Conference on Satellite Meteorology and Oceanography, May 25-29, 1998, Paris, France, pp. 327-330.

Mainville, S., 2004: Heavy convective rain events over Québec: A forecasting tool. AMS 22nd Conference on Severe Local Storms, October 4-7, 2004, Hyannis, MA.

Marcus, S., J. Kim, T. Chin, D. Danielson, and J. Laber, 2007: Influence of GPS precipitable water vapor retrievals on quantitative precipitation forecasting in Southern California. *J.*

Appl. Meteorol. Climatol., **46**, 1828-1839.

McDonald, W. F., 1938: Atlas of Climatic Charts of the Oceans. *United States Government Printing Office*, Weather Bureau Publication No. 1247, 130 charts.

Muller, C. J., L. E. Back, P. A. O'Gorman, and K. A. Emanuel, 2009: A model for the relationship between tropical precipitation and column water vapor. *Geophys. Res. Lett.*, **36**, L16804, doi: 10.1029/2009GL039667.

Neelin, J. D., O. Peters, and K. Hales, 2009: The transition to strong convection. *J. Atmos. Sci.*, **66**, 2367-2384.

NESDIS Operational Blended TPW Products Website. Available at: http://www.osdpd.noaa.gov/bTPW/.

Ojo, O., 1970: The distribution of mean monthly precipitable water vapor and annual precipitation efficiency in Nigeria. *Arch. Meteorol. Geophy. Bioklimatol. Ser. B*, **18**, 221-238.

Peixoto, J. P., and A. H. Oort, 1992: Physics of Climate. *American Institute of Physics*, 520 pp.

Randel, D. L., T. H. Vonder Haar, M. A. Ringerud, G. L. Stephens, T. J. Greenwald, and C. L. Combs, 1996: A new global water vapor dataset. *Bull. Amer. Meteor. Soc.*, **77**, 1233-1246.

Quantz, H. M., 2009: Observations of the double Intertropical Convergence Zone using CloudSat. M.S. thesis, Dept. Atmospheric Science, Colorado State University, Ft. Collins, 88 pp.

Schlosser, C. A., and P. R. Houser, 2007: Assessing a satellite-era perspective of the global water cycle. *J. Climate*, **20**, 1316-1338.

Smith, J. A., M. L. Baeck, M. Steiner, and A. J. Miller, 1996: Catastrophic rainfall from an upslope thunderstorm in the central Appalachians: The Rapidian storm of June 27, 1995. *Water Resour. Res.*, **32**, 3099-3113.

Spencer, R. W., 1986: A satellite passive 37-GHz scattering-based method for measuring oceanic rain rates. *J. Clim. Appl. Meteor.*, **25**, 754-766.

Sudradjat, A., R. R. Ferraro, and M. Fiorino, 2005: A comparison of total precipitable water between reanalyses and NVAP. *J. Climate*, **18**, 1790-1807.

Trenberth, K. E., 1998: Atmospheric moisture residence times and cycling: Implications for rainfall rates and climate change. *Climatic Change*, **39**, 667-694.

----, A. Dai, R. M. Rasmussen, and D. B. Parsons, 2003: The changing character of precipitation. *Bull. Amer. Meteor. Soc.*, **84**, 1205-1217.

Vila, D., R. Ferraro, and R. Joyce, 2007: Evaluation and improvement of AMSU precipitation retrievals. *J. Geophys. Res.*, **112**, D20119, doi: 10.1029/1007JD008617.

Wallace, J. M. and P. V. Hobbs, 2006: Atmospheric Science: An Introductory Survey. *Elsevier Inc.*, 483 pp.

Weng, F., L. Zhao, R. R. Ferraro, G. Poe, X. Li, and N. C. Grody, 2003: Advanced Microwave Sounding Unit cloud and precipitation algorithms. *Radio Sci.*, **38**, 8068, doi: 10.1029/2002RS002679.

Wilheit, T. T., A. T. C. Chang, M. S. V. Rao, E. B. Rodgers, and J. S. Theon, 1977: A satellite technique for quantitatively mapping rainfall rates over the oceans. *J. Appl. Meteorol.*, **16**, 551-560.

Wu, P., J.-I. Hamada, S. Mori, Y. I. Tauhid, M. D. Yamanaka, and F. Kimura, 2003: Diurnal variation of precipitable water over a mountainous area of Sumatra Island. *J. Appl. Meteorol.*, **42**, 1107-1115.

Xiao, Q., X. Zou, and Y.-H. Kuo, 2000: Incorporating the SSM/I-derived precipitable water and rainfall rate into a numerical model: A case study for the ERICA IOP-4 cyclone. *Mon. Wea. Rev.*, **128**, 87-108.

Xie, P., and P. A. Arkin, 1997: Global precipitation: A 17-year monthly analysis based on gauge observations, satellite estimates, and numerical model outputs. *Bull. Amer. Meteor. Soc.*, **78**, 2539-2558.

APPENDIX A: ABBREVIATIONS

AMS: American Meteorological Society

AMSU: Advanced Microwave Sounding Unit

bTPW : Blended Total Precipitable Water

CAPE: Convective Available Potential Energy

CI: Convective Index

CIRA: Cooperative Institute for Research in the Atmosphere

CMAP: CPC Merged Analysis of Precipitation

CMORPH: CPC Morphing Method

CONUS: Continental United States

CPC: Climate Prediction Center

CSAV: Cloud System Advection Vector

cT: Continental Tropical

DJF: December, January, February

DMSP: Defense Meteorological Satellite Program

ESMR: Electrically Scanning Microwave Radiometer

FOV: Field of view

GMS: Geostationary Meteorological Satellite

GOES: Geostationary Operational Environmental Satellite

GPROF: Goddard Profiling Algorithm

GPS: Global Positioning System

IR: Infrared

ITCZ: Intertropical Convergence Zone

IWP: Ice Water Path

JJA: June, July, August

MAM: March, April, May

mT: Maritime Tropical

NASA: National Aeronautics and Space Administration

NCAR: National Center for Atmospheric Research

NCEP: National Center for Environmental Prediction

NESDIS: National Environmental Satellite, Data, and Information Service

NH: Northern Hemisphere

NOAA: National Oceanic and Atmospheric Administration

NVAP: NASA Water Vapor Product

PDF: Probability Distribution Function

PMW: Passive Microwave

RR: Rainfall Rate

SH: Southern Hemisphere

SMMR: Scanning Multichannel Microwave Radiometer

SON: September, October, November

SPCZ: South Pacific Convergence Zone

SSM/I: Special Sensor Microwave Imager

Tb: Brightness Temperature

TIROS: Television and Infrared Operational Satellite

TMI: TRMM Microwave Imager

TOVS: TIROS Operational Vertical Sounder

TPW: Total Precipitable Water

TRMM: Tropical Rainfall Measuring Mission

UTC: Coordinated Universal Time

APPENDIX B: SINGLE OBSERVATIONS OF TPW AND RR

Figures B1-B4 display the observations of TPW and RR for two different time periods. In the annual and seasonal means presented in Chapter 5, the detailed daily variations have been averaged out. The fine resolution of the bTPW and CMORPH datasets is evident in the figures presented below. Figures B1 and B2 are the bTPW and CMORPH datasets on September 5, 2008 at 00 UTC, one of the days that Hurricane Ike was present in the western Atlantic. The circular TPW maximum in the western Atlantic is visible in Fig. B1 and a corresponding circular RR maximum is present in Fig. B2. The high TPW and RR values in the Bay of Bengal are also present, as expected, since these observations were made during the monsoon season. In addition, plumes of moisture are present in the northern and southern oceans in Fig. B1. In Fig. B2, the rain bands visible in the northern and southern oceans are generally coincident with these TPW moisture plumes, which supports the hypothesis that relatively high TPW values correspond with a higher probability of rainfall. However, this higher-latitude rainfall occurs at lower TPW values than the rainfall in the tropical latitudes and the high TPW values in the tropics are not always coincident with rainfall, so the presence of high TPW is not a strict indicator of rainfall.

Figures B3 and B4 display the bTPW and CMORPH datasets at 18 UTC on March 4, 2007. Similar moisture plumes and concurrent rainfall events as in Figs. B1 and B2 are present in the northern and southern oceans. Since the south Asian monsoon season is not occurring during this time, TPW and RR values are low in the Bay of Bengal. An instance of the double ITCZ is occurring in the eastern tropical Pacific, as evidenced by relatively high TPW to the north and south of the equator in Fig. B3 and the coincident rain bands in Fig. B4.

Another feature evident in Figs. B1 and B3 are the areas of missing bTPW data south of India (Fig. B1) and in the northwestern Pacific (Fig. B3). These are areas where no observations were made by any of the satellites over the 12-hour data compilation period. No such areas exist in the CMORPH dataset because areas lacking observations are ‘filled in’ using the IR advection technique described in Section 3.2.4.

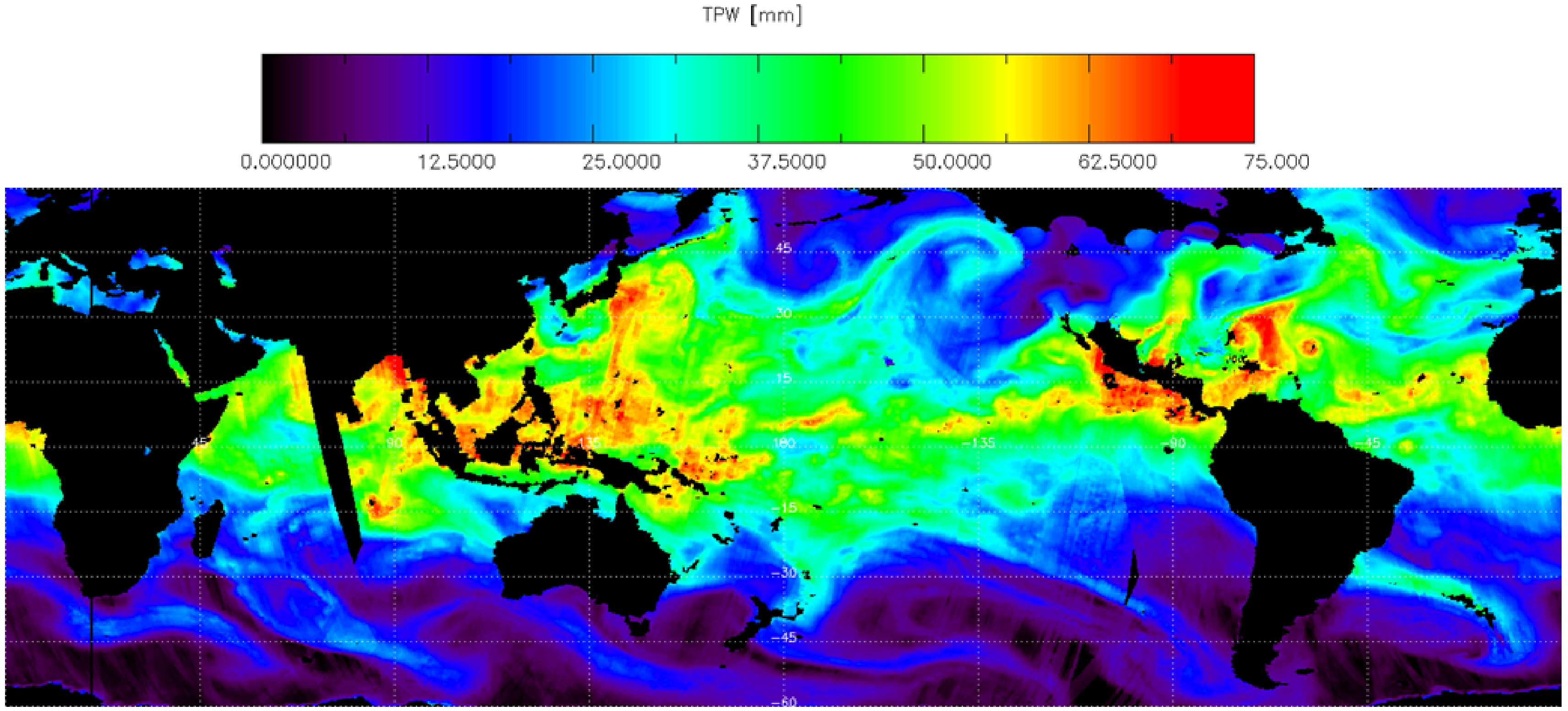

FIG. B1. TPW dataset on September 5, 2008 at 00 UTC.

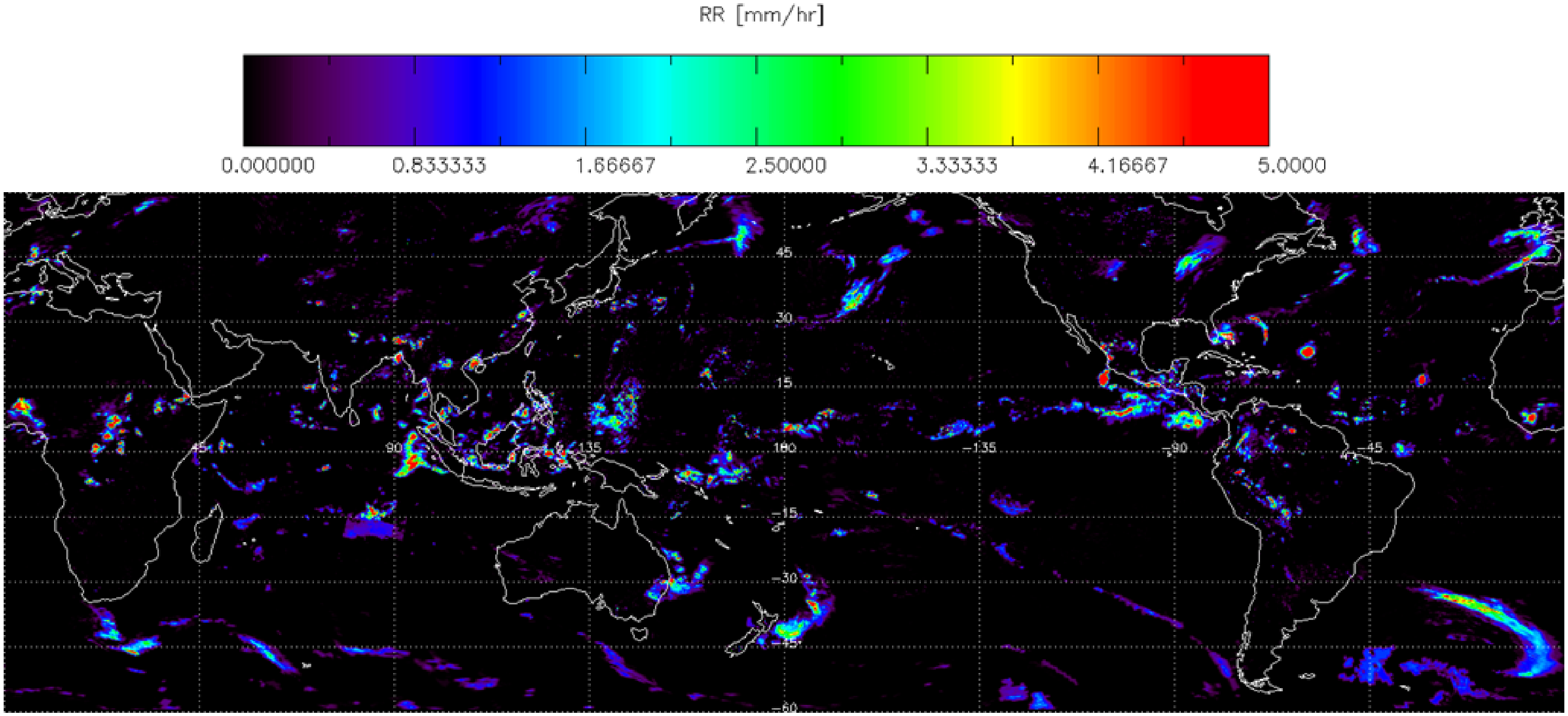

FIG. B2. RR dataset on September 5, 2008 at 00 UTC.

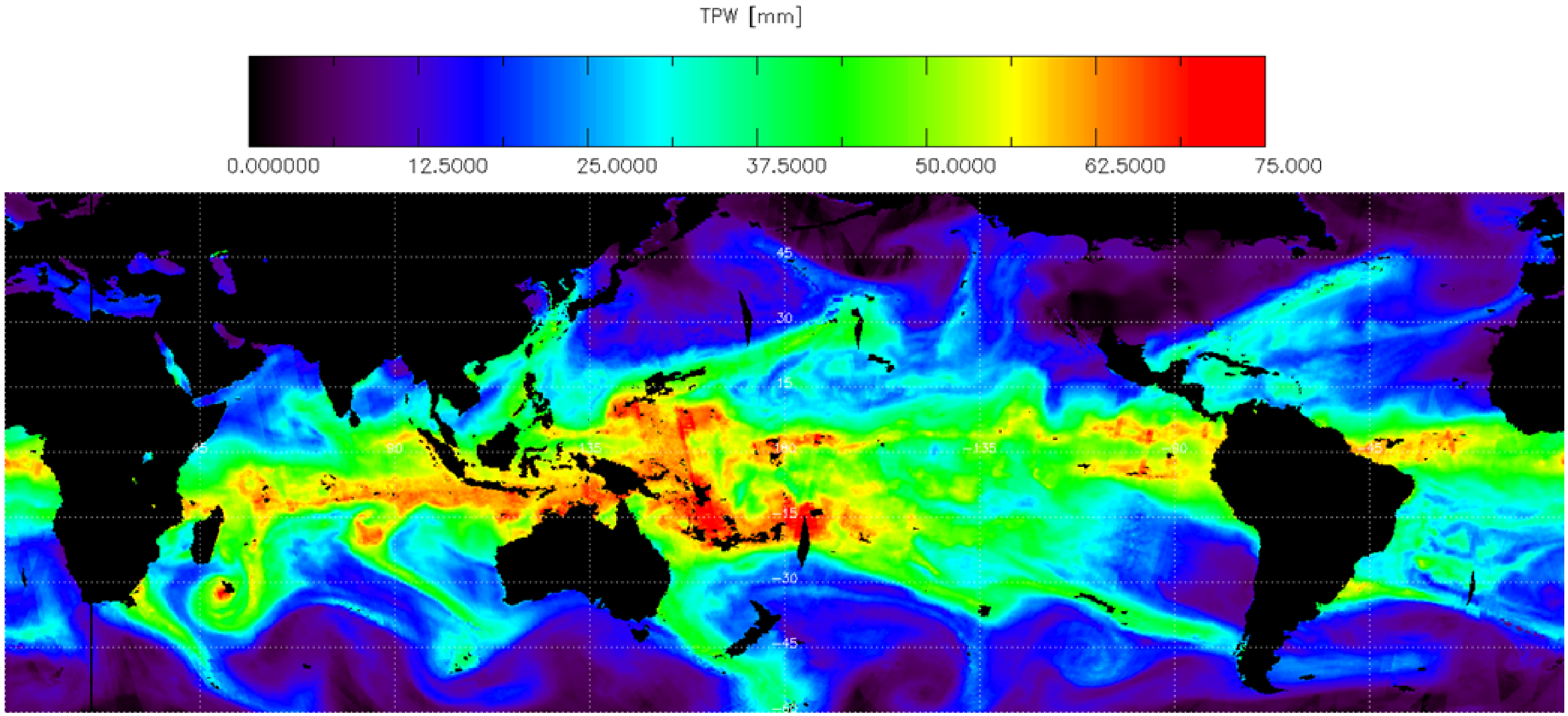

FIG. B3. TPW dataset on March 4, 2007 at 18 UTC.

N

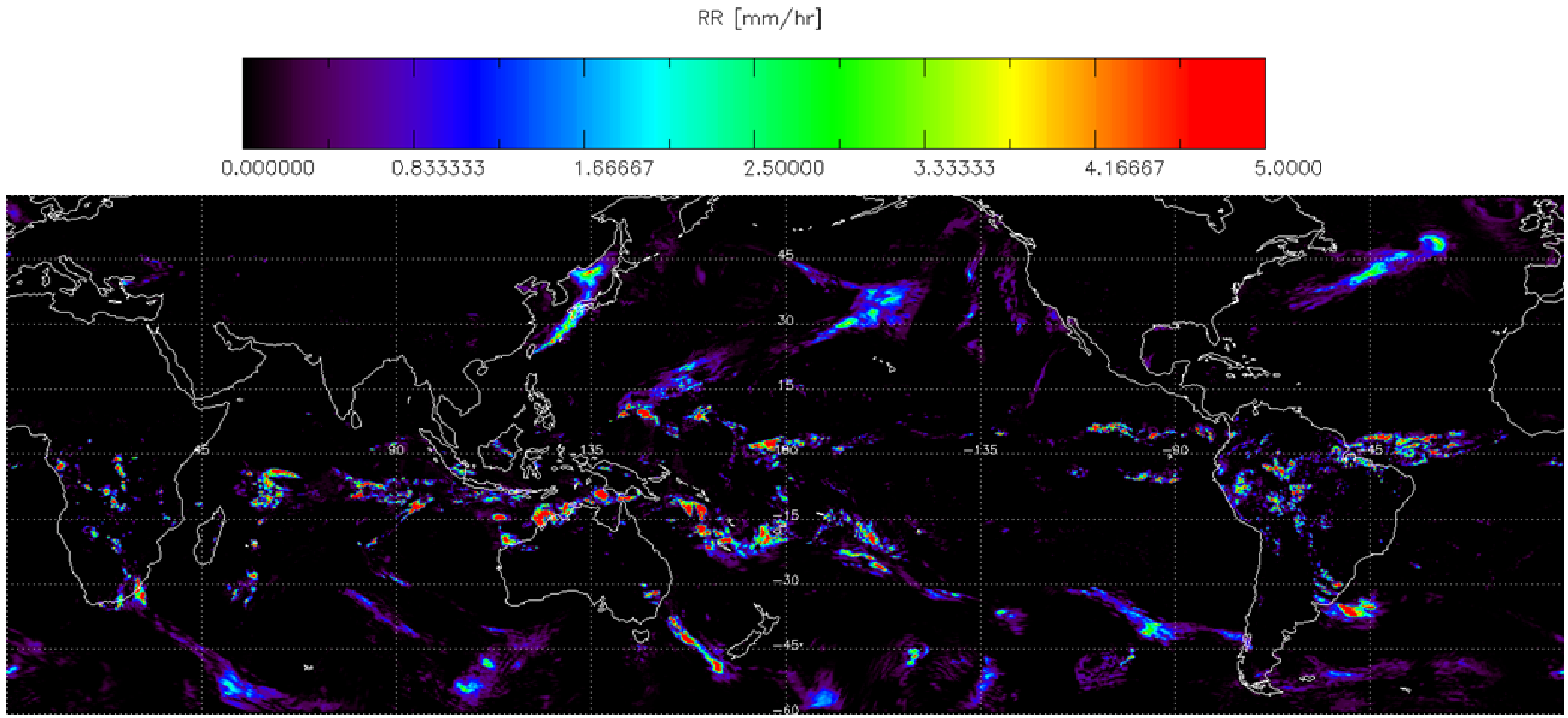

FIG. B4. RR dataset on March 4, 2007 at 18 UTC.

APPENDIX C: SEASONAL RAINFALL FREQUENCIES FROM SHIP OBSERVATIONS

Rainfall has been measured over the globe for more than 100 years. A study conducted by McDonald (1938) consists of ship observations of rainfall taken mainly between 1885 and 1933.While quantitative rainfall rates were not measured, rainfall frequencies were compiled according to the Beaufort scale, which provides for a qualitative estimation of rainfall rate. The text boxes inset on the top left of Figs. C1-C4 state: "Explanation: Percentage of all GMN observations in which the Beaufort symbols 'd,' 'r' or 'R,' and 'p,' representing respectively 'drizzle,' 'steady rain,' and 'passing showers,' occur" (McDonald 1938). McDonald (1938) describes that the Beaufort scale makes the distinction between rain and drizzle based on the drop size, as reiterated in Sec. 4.2. Only observations at Greenwich noon were used in this analysis, and additional quality control procedures were performed in order to remove values that appeared to be error-laden according to typical values for each time and location. In order to form a strictly oceanic dataset, no data from islands, continents, or in ports were used. The highest densities of observations come from the north Atlantic Ocean and the northern extratropical Pacific Ocean (McDonald 1938).

Figures C1-C4 display similar patterns to those found in Figs. 2.7 and 5.10, albeit at coarser resolution. For instance, the SPCZ appears to reach its farthest eastward in DJF and rainfall frequency increases in the Bay of Bengal during the JJA southeast Asian monsoon season. In addition, the oceanic desert regions off the west coasts of North America, South

America, and northern and southern Africa are evident in all of the figures. These regions of depressed rainfall frequencies are quite extensive in Fig. 5.10 whereas Figs. C1-C4 show more frequent rainfall in these oceanic desert regions. One explanation for this discrepancy is that the datasets comprising CMORPH do a poor job of detecting light stratiform rainfall whereas the data used to form Figs. C1-C4 do include observations of drizzle, a common occurrence over these oceanic desert areas. These 1938 results confirm the importance of supplementing the CMORPH dataset and other similarly-constructed datasets with data that is more apt to provide accurate observations of light stratiform rainfall.

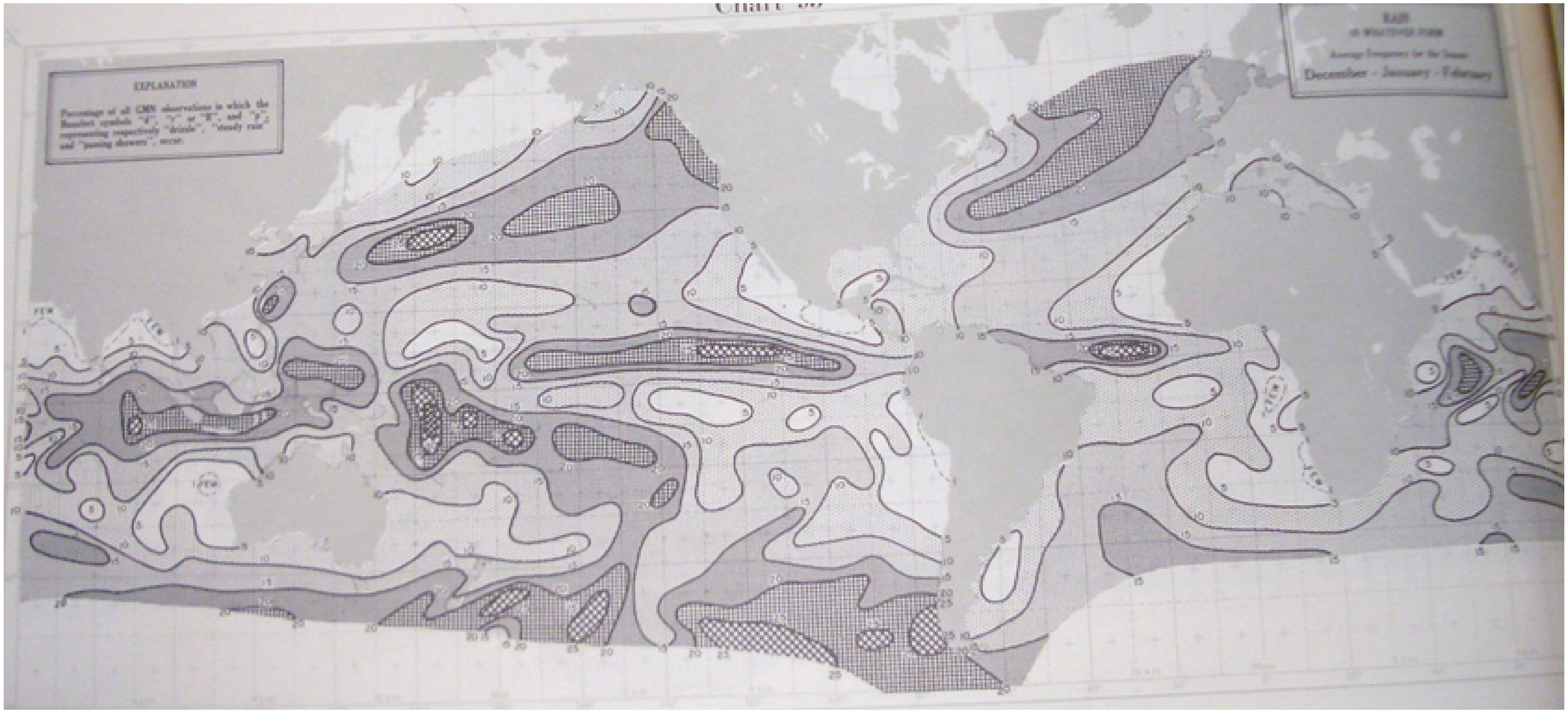

FIG. C1. DJF rainfall frequency in percent. Contours are drawn at every 5% with unshaded areas representing 0-5% and checkerboard areas representing ≥30% rainfall frequency.

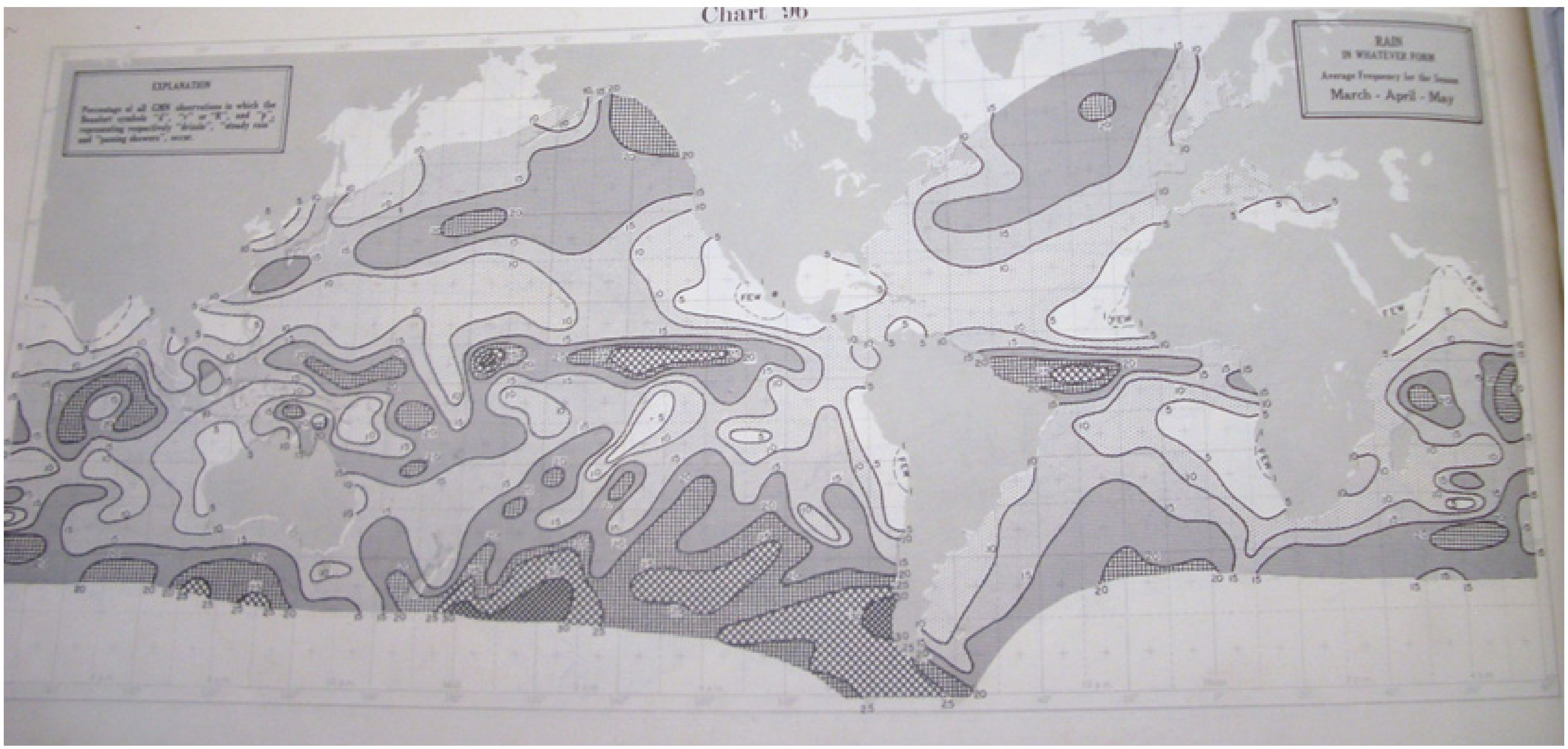

FIG. C2. As in Fig. C1 but for MAM.

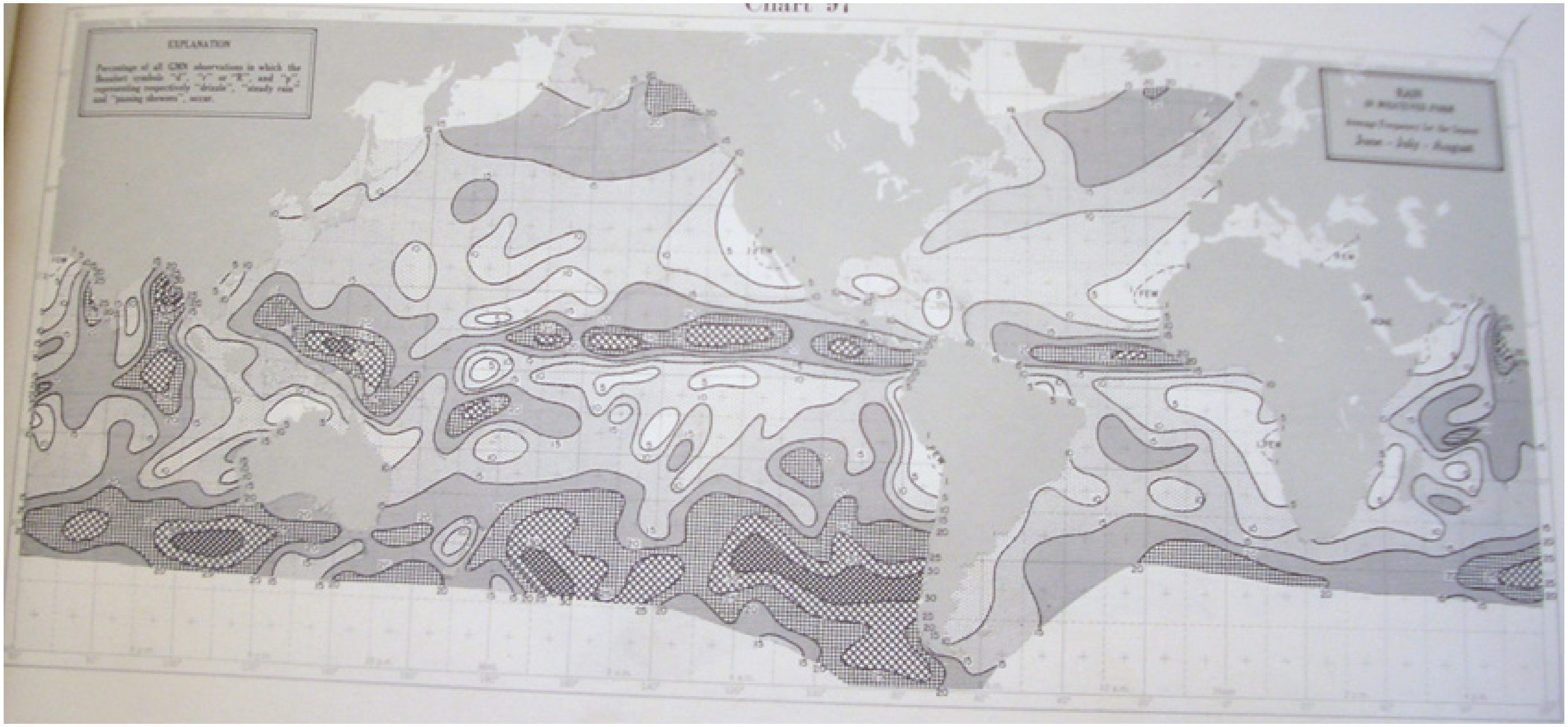

FIG. C3. As in Fig. C1 but for JJA.

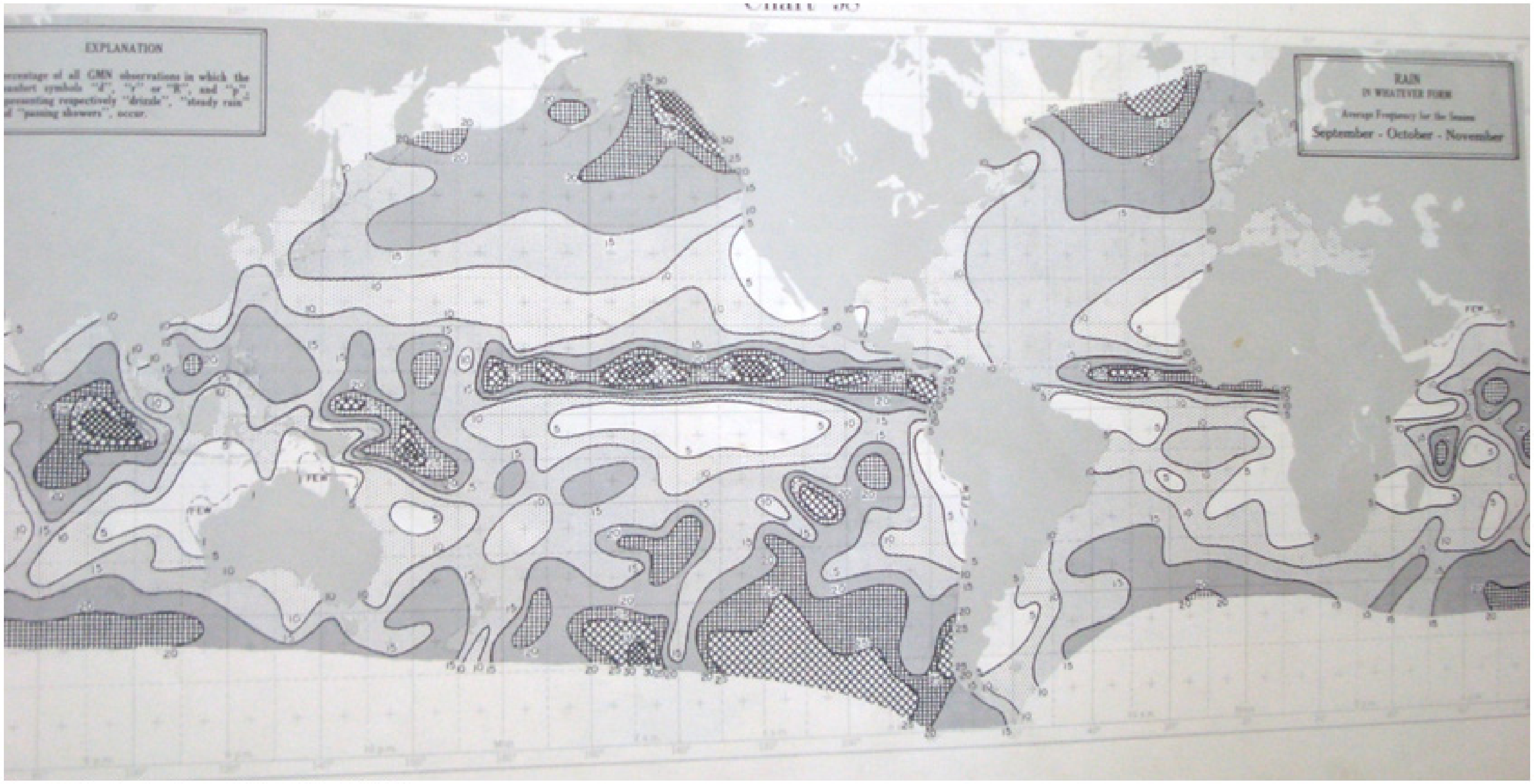

FIG. C4. As in Fig. C1 but for SON.

APPENDIX D: NVAP TPW PRODUCT

The NASA Water Vapor Product (NVAP) was developed by scientists at CIRA, as was the bTPW data product used in this thesis. This appendix serves to distinguish between the two products, as they were both developed at CIRA but are derived using different methods and instruments and are available at differing resolutions and for different time periods.

The bTPW is an operational product developed for forecasters to use, striving to blend away the streaks that accompany satellite swath observations in order to avoid any confusion that may arise from non-physical steep TPW gradients (Kidder and Jones 2007). As described in Chapter 3, the bTPW product is formed using data from three SSM/I instruments and three AMSU instruments and has been available since February 2006 with 16 km resolution at the equator.

Alternately, the NVAP product was not formed for operational use. These datasets were constructed using data from SSM/I, Television and Infrared Operational Satellite (TIROS) Operational Vertical Sounder (TOVS), and radiosonde retrievals and are available at $1^{\circ}\times 1^{\circ}$ resolution between 1988 and 2001. These three data types were combined into daily grids, blended using a weighting scheme that assigned 100% to radiosonde values (i.e., these were assumed to be truth), 90% to SSM/I, and 10% to TOVS if both satellite measures were available. Using these weights, a 'confidence map' was constructed. These daily grids were then examined directly by a team of meteorologists. This quality control process identified possible erroneous retrieval values, including those due to sea ice, small islands, regional moist biases, or even radiosonde stations which consistently overestimated the column water vapor (Randel et al. 1996).

Global climatologies similar to the one discussed in this thesis were created using this NVAP dataset. For instance, Amenu and Kumar (2005) compared NVAP TPW with that from the National Center for Environmental Prediction (NCEP)-National Center for Atmospheric Research (NCAR) reanalysis-2 project (R-2) in order to "examine their relative performance in describing the global spatial and temporal variability". They found the two products to display similar trends in TPW, although NVAP TPW values tended to be greater than those from R-2 in the NH, with the opposite occurring in the SH. It is evident from Fig. D1, which displays the annual mean TPW for each product, that the two datasets show similar trends but display clear differences, such as the lower magnitudes of R-2 TPW in the Western Pacific Ocean. Figure D1 may also be compared with the annual mean TPW from the bTPW product shown in Fig. 5.1. Schlosser and Houser (2007) compared the NVAP TPW dataset to several other TPW datasets in order to determine if satellite measurements "faithfully depict" global TPW trends, finding that merged data products generally provide the "best" results. Although the bTPW and NVAP products were formed using different methods and instruments, they show similar variations in TPW and can be used for similar types of studies.

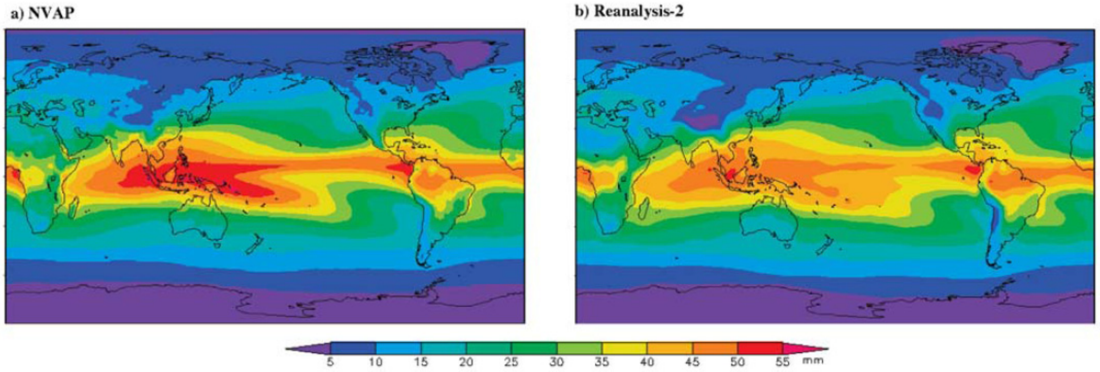

FIG. D1. 12-year annual mean TPW in mm for the (a) NVAP and (b) reanalysis-2 datasets. Source: Amenu and Kumar (2005).